Lucchi, R.G., St. John, K.E.K., Ronge, T.A., and the Expedition 403 Scientists
Proceedings of the International Ocean Discovery Program Volume 403
publications.iodp.org

Site U1618[1]

R.G. Lucchi, K.E.K. St. John, T.A. Ronge, M.A. Barcena, S. De Schepper, L.C. Duxbury, A.C. Gebhardt, A. Gonzalez-Lanchas, G. Goss, N.M. Greco, J. Gruetzner, L. Haygood, K. Husum, M. Iizuka, A.K.I.U. Kapuge, A.R. Lam, O. Libman-Roshal, Y. Liu, L.R. Monito, B.T. Reilly, Y. Rosenthal, Y. Sakai, A.V. Sijinkumar, Y. Suganuma, and Y. Zhong[2]

[1] Lucchi, R.G., St. John, K.E.K., Ronge, T.A., Barcena, M.A., De Schepper, S., Duxbury, L.C., Gebhardt, A.C., Gonzalez-Lanchas, A., Goss, G., Greco, N.M., Gruetzner, J., Haygood, L., Husum, K., Iizuka, M., Kapuge, A.K.I.U., Lam, A.R., Libman-Roshal, O., Liu, Y., Monito, L.R., Reilly, B.T., Rosenthal, Y., Sakai, Y., Sijinkumar, A.V., Suganuma, Y., and Zhong, Y., 2026. Site U1618. In Lucchi, R.G., St. John, K.E.K., Ronge, T.A., and the Expedition 403 Scientists, Eastern Fram Strait Paleo-Archive. Proceedings of the International Ocean Discovery Program, 403: College Station, TX (International Ocean Discovery Program). https://doi.org/10.14379/iodp.proc.403.103.2026
[2] **Expedition 403 Scientists' affiliations.**

Contents

Keywords
International Ocean Discovery Program, IODP, Expedition 403, *JOIDES Resolution*, Eastern Fram Strait Paleo-Archive, Earth climate system, biosphere frontiers, carbon sequestration, Site U1618, Svalbard-Barents Sea Ice Sheet, North Atlantic Water, West Spitsbergen Current, gas hydrate, sediment drift, Vestnesa Ridge, sea ice, Northern Hemisphere glaciation, Pleistocene

Core descriptions

Supplementary material

References (RIS)

MS 403-103
Published 29 January 2026

Funded by NSF OCE1326927, ECORD, and JAMSTEC

1. Background and objectives

The Vestnesa Ridge is a roughly east–west oriented prominent bathymetric feature situated in the Fram Strait on the western continental margin of Svalbard (Figure **F1**). Its evolution is linked to the tectonic, sedimentary, and climatic history of the region, making it a focal point for multidisciplinary scientific research. The 100 km long ridge is a sediment drift generated by persistent bottom currents associated with the West Spitsbergen Current (WSC) (Eiken and Hinz, 1993) that developed over oceanic crust since the Fram Strait opening (17–10 Ma) (Jakobsson et al., 2007; Engen et al., 2008; Ehlers and Jokat, 2013). Although the chronology of the Vestnesa Ridge sediment record deposited since the last glacial is well established (e.g., Rasmussen and Nielsen, 2024, and references therein) and regionally correlatable (Lucchi et al., 2023), the chronology prior to approximately Marine Isotope Stage (MIS) 5 is limited to extrapolation from seismic data from previously drilled sites on the Yermak Plateau (Ocean Drilling Program [ODP] Site 912) and south

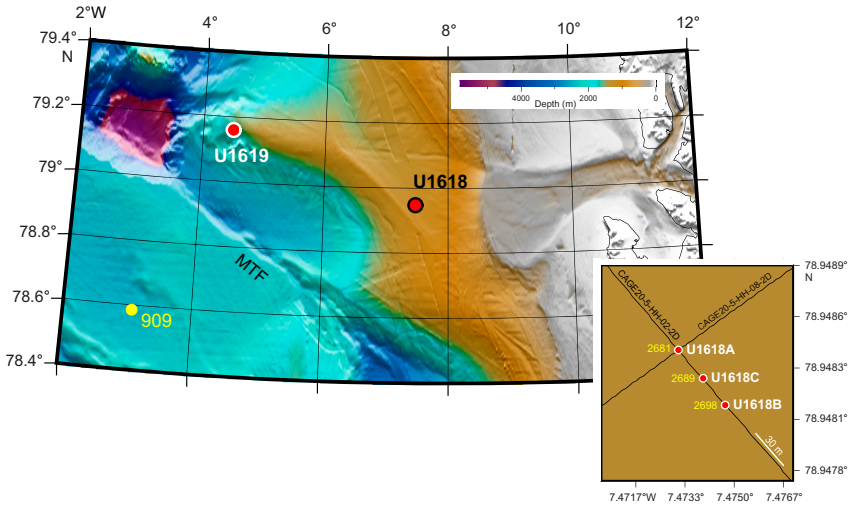

Figure F1. Bathymetric map showing the locations of Sites U1618 and U1619 on the eastern and western terminations of the Vestnesa Ridge sediment drift, respectively. Site U1618 is located ~22 km from the shelf edge of the Kongsfjorden glacial trough in northwestern Spitsbergen. The Molloy Transform Fault (MTF) is parallel to and south of the Vestnesa Ridge and connects the actively spreading Knipovich and Molloy Ridge segments. ODP Site 909 is located on an abyssal hill south of the MTF. Inset: close-up view of Holes U1618A–U1618C. Holes U1618B and U1618C are respectively located 50 and 25 m southeast of Hole U1618A along Seismic Line CAGE20-5-HH-02-2D. Seismic trace numbers (yellow) are shown.

of the Molloy Transform Fault (ODP Site 909) (Eiken and Hinz, 1993; Knies et al., 2014; Mattingsdal et al., 2014). Seismic Reflectors R1–R8 were drilling targets for Site U1618 (Figure **F2**), with a total depth target of 738 meters below seafloor (mbsf).

The sedimentation and geologic development in this area has been heavily influenced by Pliocene–Pleistocene glaciations, with ice sheet extent over Svalbard and the Barents Sea, and Arctic Ocean sea ice (Jakobsson et al., 2014). Depositional facies representing a range of glaciogenic and bottom current depositional processes, including ice rafting events, dense glacial debris flows, and subglacial meltwater plumes, are well documented in the recent sedimentary record along the western Svalbard continental margin (e.g., Lucchi et al., 2013, 2015; Caricchi et al., 2019) and the Vestnesa Ridge (Schneider et al., 2018; Sztybor and Rasmussen, 2017; Plaza-Faverola et al., 2023; Rasmussen and Nielsen, 2024). The presence of gas hydrates and associated fluid migration are additional controls on the sedimentary record of the Vestnesa Ridge.

Bathymetric and seismic surveys have revealed numerous pockmarks and fluid escape features along the Vestnesa Ridge, indicating active seepage of methane and other hydrocarbons (Hustoft et al., 2009; Bünz et al., 2012; Smith et al., 2014). Seismic surveys also reveal a regional gas hydrate–related bottom-simulating reflector (BSR) and thus the presence of gas hydrate and free gas at depth. Previous studies indicate that the hydrate stability zone is several hundred meters thick and can extend to the seafloor (Himmler et al., 2019; Pape et al., 2020; Rasmussen and Nielsen, 2024; Plaza-Faverola et al., 2023).

Spatial changes in seafloor morphology, faults, and seepage characteristics led to the distinction of two main areas along the Vestnesa Ridge (Plaza-Faverola et al., 2015; Schneider et al., 2018; Sztybor and Rasmussen, 2017): (1) the East Vestnesa Ridge, characterized by a narrow crest (~3 km wide) and large pockmarks connected with chimneys with ongoing seepage activity, and (2) the West Vestnesa Ridge, characterized by a larger crest (>10 km wide) and small, apparently inactive pockmarks, although multidisciplinary investigations point to the presence of methane in the subseafloor (e.g., Consolaro et al., 2015; Plaza-Faverola et al., 2015; Sultan et al., 2020).

Site U1618 (Figure **F1**), located on the Vestnesa Ridge East termination, was chosen for its proximity to the continental margin and outer reaches of the former paleo-Svalbard–Barents Sea Ice Sheet, which make this site ideal to reconstruct the ice sheet dynamics in the northern area. For safety and to maximize recovery toward the primary science objectives, Site U1618 was positioned

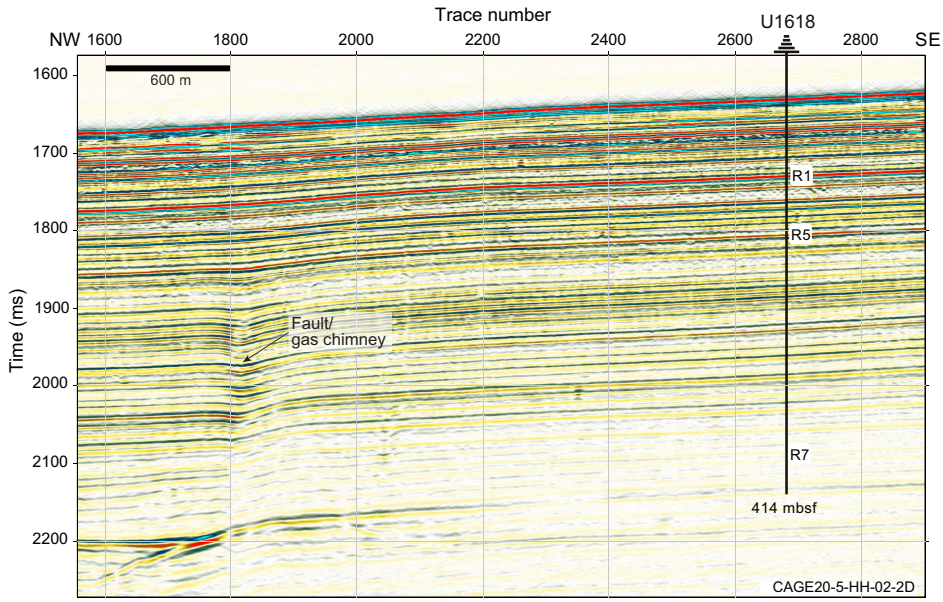

Figure F2. Seismic profile along northwest–southeast Seismic Line CAGE20-5-HH-02-2D showing the location of Site U1618. Interpreted reflectors R1, R5, and R7 and the maximum penetration depth (414 mbsf) are shown. Time is two-way traveltime.

away from the regional BSR, and Hole U1618A was located on Seismic Line CAGE20-5-HH-02-2D at 3.8 km from a gas chimney and 1.1 km from a fault that was supposed to act as a conduit for fluid migration (Figure **F2**). Holes U1618B and U1618C were located 50 and 25 m northeast from Hole U1618A, respectively, along the same seismic line (Figure **F1**). Water depths at all three holes were between 1195 and 1196 m. The deepest penetration (Hole U1618B) reached 414 mbsf, and the maximum recovery (Hole U1618C) was 110%.

The research objectives for Site U1618 include the following:

- Reconstruction of a high-resolution sediment stratigraphy since the Late Miocene–Early Pliocene transition;
- Study of ocean-cryosphere interactions and forcing mechanisms on the paleo–ice sheet dynamics;
- Definition of the effect of glacial and tectonic stresses on subseafloor sediment deformation and carbon transport; and
- Investigation of the influence of the WSC variability, ice coverage, and climate on the microbial populations through time and to what extent this is still affecting contemporary geochemical fluxes.

Additionally, this location offers the opportunity to explore possible relationships (including feedbacks and tipping points) among paleo–ice sheets, gas hydrate stability, and tectonic stress.

2. Operations

We started our 1677 nmi voyage across the North Atlantic to Fram Strait Site U1618 at 0800 h local time on 4 June 2024 in Amsterdam, The Netherlands. Throughout the transit, all groups familiarized themselves with their respective laboratories and worked on writing their methods sections. The COVID-19 mitigation protocol was followed until 11 June, when it ended at 1815 h after no one tested positive. We completed the transit on 14 June at an average speed of 9.9 kt.

In total, we spent 9.18 days at Site U1618 and penetrated a maximum depth of 414.3 mbsf with a combined penetration of 1104.3 m. The cored interval of 1102.3 m resulted in a recovered length of 1078.45 m. Site U1618 consists of three holes over a 50 m interval (25 m between holes) along Seismic Line CAGE20-5-HH-02-2D. We took 152 cores in total: 26.3% with the advanced piston corer (APC) system (40 cores), 11.2% with the half-length APC (HLAPC) system (17 cores), and 62.5% with the extended core barrel (XCB) system (95 cores). To minimize magnetic overprinting on the cored sediment, nonmagnetic collars and core barrels were used for all APC and HLAPC coring. All three holes had intervals where the sediments significantly expanded due to the presence of gas, resulting in recoveries often exceeding 100% (Table **T1**). To mitigate the impact of expansion and the potential for core disturbance and to release the pressure, holes were drilled into the liner by the drill crew on the rig floor and the technical staff on the core receiving platform (i.e., catwalk).

To more easily communicate shipboard results, core depth below seafloor, Method A (CSF-A), depths in this chapter are reported as mbsf unless otherwise noted.

2.1. Hole U1618A

The vessel arrived on site on 14 June 2024 with thrusters down and the vessel in full automatic dynamic positioning (DP) mode at 0919 h, beginning operations at the site. A positioning beacon was deployed as a backup to GPS. A depth reading was taken using the precision depth recorder (PDR), estimating the seafloor at 1191.8 meters below sea level (mbsl). The crew assembled the APC bottom-hole assembly (BHA), and prior to beginning coring operations, approximately 1000 m of core winch line were slipped from the drum due to excessive corrosion on the line. The line was reheaded, and a core barrel was deployed. The bit was spaced to 1186.8 mbsl, 5 m above the PDR seafloor depth, and a mudline core was attempted. The first recovered core barrel came back empty; thus, the bit was lowered 5 m to 1191.8 mbsl, and a second core barrel was deployed. Hole U1618A was spudded at 2225 h on 14 June, and the seafloor depth was calculated to be 1196.0

Table T1. Core summary, Site U1618. mbsf = meters below seafloor, NA = not applicable. H = advanced piston corer (APC), F = half-length APC (HLAPC), numeric core type = drilled interval. DSF = depth below seafloor. Times in UTC are 2 h behind the local times given in the text at the time of drilling. (Continued on next two pages.) **Download table in CSV format.**

Hole U1618A
Latitude: 78°56.9070′N
Longitude: 7°28.3866′E
Water depth (m): 1196
Date started (UTC): 4 June 2024; 0719 h
Date finished (UTC): 16 June 2024; 0845 h
Time on hole (days): 2.06
Penetration (mbsf): 276.9
Cored interval (m): 276.9
Recovered length (m): 252.62
Recovery (%): 91.23
Drilled interval (m): NA
Drilled interval (no.): 0
Total cores (no.): 37
APC cores (no.): 11
HLAPC cores (no.): 13
XCB cores (no.): 13

Hole U1618B
Latitude: 78°56.8855′N
Longitude: 7°28.4818′E
Water depth (m): 1195.23
Date started (UTC): 16 June 2024; 0845 h
Date finished (UTC): 20 June 2024; 0545 h
Time on hole (days): 3.88
Penetration (mbsf): 414.3
Cored interval (m): 414.3
Recovered length (m): 375.24
Recovery (%): 90.57
Drilled interval (m): NA
Drilled interval (no.): 0
Total cores (no.): 54
APC cores (no.): 14
HLAPC cores (no.): 1
XCB cores (no.): 39

Hole U1618C
Latitude: 78°56.8960′N
Longitude: 7°28.4368′E
Water depth (m): 1195.79
Date started (UTC): 20 June 2024; 0545 h
Date finished (UTC): 23 June 2024; 1130 h
Time on hole (days): 3.24
Penetration (mbsf): 413.1
Cored interval (m): 411.1
Recovered length (m): 450.59
Recovery (%): 109.61
Drilled interval (m): 2
Drilled interval (no.): 1
Total cores (no.): 61
APC cores (no.): 15
HLAPC cores (no.): 3
XCB cores (no.): 43

Core	Top depth drilled DSF (m)	Bottom depth drilled DSF (m)	Interval advanced (m)	Recovered length (m)	Curated length (m)	Top depth cored CSF (m)	Bottom depth cored CSF (m)	Recovery (%)	Core on deck date (2024)	Core on deck time UTC (h)
403-U1618A-										
1H	0.0	4.9	4.9	4.88	4.88	0.0	4.88	100	14 Jun	0840
2H	4.9	14.4	9.5	9.92	9.92	4.9	14.82	104	14 Jun	0900
3H	14.4	23.9	9.5	9.95	9.95	14.4	24.35	105	14 Jun	0940
4H	23.9	33.4	9.5	9.95	9.95	23.9	33.85	105	14 Jun	1115
5H	33.4	42.9	9.5	10.26	10.26	33.4	43.66	108	15 Jun	1145
6H	42.9	52.4	9.5	10.39	10.39	42.9	53.29	109	15 Jun	1225
7H	52.4	61.9	9.5	2.70	2.70	52.4	55.10	28	15 Jun	0120
8H	61.9	70.4	8.5	8.49	8.49	61.9	70.39	100	15 Jun	0205
9H	70.4	78.4	8.0	7.96	7.96	70.4	78.36	100	15 Jun	0300
10H	78.4	86.3	7.9	7.87	7.87	78.4	86.27	100	15 Jun	0410
11H	86.3	94.0	7.7	7.70	7.70	86.3	94.00	100	15 Jun	0515
12F	94.0	98.7	4.7	4.99	4.99	94.0	98.99	106	15 Jun	0615
13F	98.7	103.4	4.7	5.19	5.19	98.7	103.89	110	15 Jun	0700
14F	103.4	108.1	4.7	4.82	4.82	103.4	108.22	103	15 Jun	0725
15F	108.1	112.8	4.7	4.95	4.95	108.1	113.05	105	15 Jun	0810
16F	112.8	117.5	4.7	5.09	5.09	112.8	117.89	108	15 Jun	0845
17F	117.5	122.2	4.7	3.03	3.03	117.5	120.53	64	15 Jun	0940
18F	122.2	125.2	3.0	4.78	4.78	122.2	126.98	159	15 Jun	1035
19F	125.2	129.9	4.7	5.13	5.13	125.2	130.33	109	15 Jun	1105
20F	129.9	134.6	4.7	5.11	5.11	129.9	135.01	109	15 Jun	1135
21F	134.6	139.3	4.7	4.96	4.96	134.6	139.56	106	15 Jun	1205
22F	139.3	144.0	4.7	5.14	5.14	139.3	144.44	109	15 Jun	1245
23F	144.0	148.7	4.7	4.87	4.87	144.0	148.87	104	15 Jun	0205
24F	148.7	150.8	2.1	2.12	2.12	148.7	150.82	101	15 Jun	0235
25X	150.8	160.3	9.5	9.10	9.10	150.8	159.90	96	15 Jun	0350
26X	160.3	169.8	9.5	6.80	6.80	160.3	167.10	72	15 Jun	0500
27X	169.8	179.3	9.5	6.68	6.68	169.8	176.48	70	15 Jun	0550
28X	179.3	189.1	9.8	6.31	6.31	179.3	185.61	64	15 Jun	0645
29X	189.1	198.9	9.8	8.55	8.55	189.1	197.65	87	15 Jun	0730
30X	198.9	208.7	9.8	9.15	9.15	198.9	208.05	93	15 Jun	0820
31X	208.7	218.5	9.8	6.76	6.76	208.7	215.46	69	15 Jun	0900

Table T1 (continued). (Continued on next page.)

Core	Top depth drilled DSF (m)	Bottom depth drilled DSF (m)	Interval advanced (m)	Recovered length (m)	Curated length (m)	Top depth cored CSF (m)	Bottom depth cored CSF (m)	Recovery (%)	Core on deck date (2024)	Core on deck time UTC (h)
32X	218.5	228.3	9.8	5.71	5.71	218.5	224.21	58	15 Jun	1000
33X	228.3	238.1	9.8	9.20	9.20	228.3	237.50	94	15 Jun	1115
34X	238.1	247.8	9.7	9.31	9.31	238.1	247.41	96	16 Jun	0105
35X	247.8	257.5	9.7	6.89	6.89	247.8	254.69	71	16 Jun	0405
36X	257.5	267.2	9.7	9.20	9.20	257.5	266.70	95	16 Jun	0510
37X	267.2	276.9	9.7	8.71	8.71	267.2	275.91	90	16 Jun	0645
403-U1618B-										
1H	0	2.8	2.8	2.82	2.82	0	2.82	101	16 Jun	1100
2H	2.8	12.3	9.5	9.71	9.71	2.8	12.51	102	16 Jun	1155
3H	12.3	21.8	9.5	9.72	9.72	12.3	22.02	102	16 Jun	1225
4H	21.8	31.3	9.5	9.49	9.49	21.8	31.29	100	16 Jun	1250
5H	31.3	40.8	9.5	9.80	9.87	31.3	41.17	103	16 Jun	0115
6H	40.8	48.2	7.4	7.41	7.43	40.8	48.23	100	16 Jun	0145
7H	48.2	57.7	9.5	9.35	9.35	48.2	57.55	98	16 Jun	0240
8H	57.7	66.5	8.8	8.78	8.78	57.7	66.48	100	16 Jun	0500
9H	66.5	76.0	9.5	9.15	9.15	66.5	75.65	96	16 Jun	0600
10H	76.0	85.5	9.5	10.18	10.18	76.0	86.18	107	16 Jun	0630
11H	85.5	95.0	9.5	9.39	9.39	85.5	94.89	99	16 Jun	0655
12H	95.0	104.5	9.5	8.27	8.27	95.0	103.27	87	16 Jun	0820
13H	104.5	112.8	8.3	8.26	8.26	104.5	112.76	100	16 Jun	0910
14F	112.8	117.5	4.7	1.63	1.63	112.8	114.43	35	16 Jun	1045
15H	117.5	117.7	0.2	0.15	0.15	117.5	117.65	75	16 Jun	1135
16X	117.7	127.5	9.8	0.06	0.06	117.7	117.76	1	17 Jun	0140
17X	127.5	137.3	9.8	5.83	5.83	127.5	133.33	59	17 Jun	0410
18X	137.3	147.1	9.8	6.16	6.16	137.3	143.46	63	17 Jun	0810
19X	147.1	156.9	9.8	5.10	5.10	147.1	152.20	52	17 Jun	0900
20X	156.9	166.7	9.8	8.74	8.74	156.9	165.64	89	17 Jun	1025
21X	166.7	176.5	9.8	7.69	7.69	166.7	174.39	78	17 Jun	1215
22X	176.5	186.3	9.8	4.79	4.79	176.5	181.29	49	17 Jun	0105
23X	186.3	193.3	7.0	9.18	9.18	186.3	195.48	131	17 Jun	0320
24X	193.3	200.8	7.5	8.73	8.73	193.3	202.03	116	17 Jun	0445
25X	200.8	206.8	6.0	7.19	7.19	200.8	207.99	120	17 Jun	0545
26X	206.8	214.8	8.0			206.8	206.80		17 Jun	0830
27X	214.8	219.7	4.9	6.94	6.94	214.8	221.74	142	17 Jun	0950
28X	219.7	225.7	6.0	8.49	8.49	219.7	228.19	142	17 Jun	1045
29X	225.7	232.7	7.0	8.02	8.02	225.7	233.72	115	17 Jun	1140
30X	232.7	240.7	8.0	2.60	2.60	232.7	235.30	33	18 Jun	1240
31X	240.7	247.7	7.0	6.76	6.76	240.7	247.46	97	18 Jun	0315
32X	247.7	254.7	7.0	8.12	8.12	247.7	255.82	116	18 Jun	0400
33X	254.7	261.7	7.0	8.54	8.54	254.7	263.24	122	18 Jun	0455
34X	261.7	268.7	7.0	8.83	8.83	261.7	270.53	126	18 Jun	0540
35X	268.7	275.7	7.0	0.23	0.23	268.7	268.93	3	18 Jun	0640
36X	275.7	282.7	7.0	3.91	3.91	275.7	279.61	56	18 Jun	0730
37X	282.7	289.7	7.0	6.10	6.10	282.7	288.80	87	18 Jun	0820
38X	289.7	296.7	7.0	5.72	5.72	289.7	295.42	82	18 Jun	0920
39X	296.7	303.7	7.0	6.41	6.41	296.7	303.11	92	18 Jun	1015
40X	303.7	313.5	9.8	9.67	9.67	303.7	313.37	99	18 Jun	1130
41X	313.5	323.3	9.8	9.69	9.69	313.5	323.19	99	18 Jun	0140
42X	323.3	330.3	7.0	9.73	9.73	323.3	333.03	139	18 Jun	0345
43X	330.3	337.3	7.0	7.33	7.33	330.3	337.63	105	18 Jun	0450
44X	337.3	344.3	7.0	3.20	3.20	337.3	340.50	46	18 Jun	0555
45X	344.3	351.3	7.0	8.99	8.99	344.3	353.29	128	18 Jun	0745
46X	351.3	358.3	7.0	6.82	6.82	351.3	358.12	97	18 Jun	0840
47X	358.3	365.3	7.0	6.83	6.83	358.3	365.13	98	18 Jun	0945
48X	365.3	372.3	7.0	8.50	8.50	365.3	373.80	121	18 Jun	1100
49X	372.3	379.3	7.0	9.68	9.68	372.3	381.98	138	19 Jun	1250
50X	379.3	386.3	7.0	7.84	7.84	379.3	387.14	112	19 Jun	0205
51X	386.3	393.3	7.0	9.58	9.58	386.3	395.88	137	19 Jun	0330
52X	393.3	400.3	7.0	2.16	2.16	393.3	395.46	31	19 Jun	0510
53X	400.3	407.3	7.0	7.57	7.57	400.3	407.87	108	19 Jun	0740
54X	407.3	414.3	7.0	9.40	9.40	407.3	416.70	134	19 Jun	0940
403-U1618C-										
1H	0	7.3	7.3	7.28	7.28	0	7.28	100	20 Jun	0820
2H	7.3	16.8	9.5	9.37	9.37	7.3	16.67	99	20 Jun	0900
3H	16.8	26.3	9.5	9.64	9.64	16.8	26.44	101	20 Jun	0950
4H	26.3	32.4	6.1	6.25	6.25	26.3	32.55	102	20 Jun	1020
5H	32.4	39.7	7.3	7.49	7.49	32.4	39.89	103	20 Jun	1055
6H	39.7	49.2	9.5	10.18	10.18	39.7	49.88	107	20 Jun	1140

Table T1 (continued).

Core	Top depth drilled DSF (m)	Bottom depth drilled DSF (m)	Interval advanced (m)	Recovered length (m)	Curated length (m)	Top depth cored CSF (m)	Bottom depth cored CSF (m)	Recovery (%)	Core on deck date (2024)	Core on deck time UTC (h)
7H	49.2	58.7	9.5	10.01	9.99	49.2	59.19	105	20 Jun	1210
8H	58.7	66.1	7.4	7.37	7.37	58.7	66.07	100	20 Jun	0100
9H	66.1	74.5	8.4	8.26	8.26	66.1	74.36	98	20 Jun	0135
10H	74.5	82.8	8.3	8.14	8.14	74.5	82.64	98	20 Jun	0230
11H	82.8	91.6	8.8	8.84	8.84	82.8	91.64	100	20 Jun	0330
12H	91.6	91.7	0.1	0.08	0.08	91.6	91.68	80	20 Jun	0530
13F	91.7	96.4	4.7	4.82	4.82	91.7	96.52	103	20 Jun	0615
14H	96.4	103.2	6.8	6.79	6.79	96.4	103.19	100	20 Jun	0720
15F	103.2	107.9	4.7	4.08	4.08	103.2	107.28	87	20 Jun	0850
161	107.9	109.9	2.0	***Drilled interval***		107.9	107.90	NA	20 Jun	0940
17F	109.9	114.6	4.7	4.81	4.81	109.9	114.71	102	20 Jun	1015
18H	114.6	119.9	5.3	5.34	5.34	114.6	119.94	101	21 Jun	1230
19H	119.9	125.6	5.7	5.67	5.67	119.9	125.57	99	21 Jun	0145
20X	125.6	132.6	7.0	9.30	9.30	125.6	134.90	133	21 Jun	0310
21X	132.6	139.6	7.0	8.92	8.92	132.6	141.52	127	21 Jun	0420
22X	139.6	146.6	7.0	6.83	6.83	139.6	146.43	98	21 Jun	0505
23X	146.6	153.6	7.0	7.59	7.59	146.6	154.19	108	21 Jun	0555
24X	153.6	160.6	7.0	8.52	8.52	153.6	162.12	122	21 Jun	0635
25X	160.6	164.6	4.0	4.61	4.61	160.6	165.21	115	21 Jun	0720
26X	164.6	171.6	7.0	6.84	6.84	164.6	171.44	98	21 Jun	0815
27X	171.6	175.6	4.0	6.27	6.27	171.6	177.87	157	21 Jun	0915
28X	175.6	182.6	7.0	2.83	2.83	175.6	178.43	40	21 Jun	1010
29X	182.6	189.6	7.0	5.97	5.97	182.6	188.57	85	21 Jun	1100
30X	189.6	196.6	7.0	8.02	8.02	189.6	197.62	115	21 Jun	1155
31X	196.6	203.6	7.0	7.05	7.05	196.6	203.65	101	21 Jun	1240
32X	203.6	208.6	5.0	7.05	7.05	203.6	210.65	141	21 Jun	0135
33X	208.6	215.6	7.0	5.93	5.93	208.6	214.53	85	21 Jun	0215
34X	215.6	222.6	7.0	5.64	5.64	215.6	221.24	81	21 Jun	0315
35X	222.6	229.6	7.0	7.47	7.47	222.6	230.07	107	21 Jun	0405
36X	229.6	236.6	7.0	7.76	7.76	229.6	237.36	111	21 Jun	0500
37X	236.6	241.6	5.0	9.34	9.34	236.6	245.94	187	21 Jun	0550
38X	241.6	247.6	6.0	8.70	8.70	241.6	250.30	145	21 Jun	0655
39X	247.6	253.6	6.0	9.00	9.00	247.6	256.60	150	21 Jun	0755
40X	253.6	260.1	6.5	9.44	9.44	253.6	263.04	145	21 Jun	0845
41X	260.1	267.1	7.0	8.10	8.10	260.1	268.20	116	21 Jun	0945
42X	267.1	274.6	7.5	6.21	6.21	267.1	273.31	83	21 Jun	1040
43X	274.6	278.6	4.0	6.19	6.19	274.6	280.79	155	21 Jun	1135
44X	278.6	286.1	7.5	8.92	8.92	278.6	287.52	119	22 Jun	0110
45X	286.1	293.6	7.5	5.81	5.81	286.1	291.91	77	22 Jun	0220
46X	293.6	297.6	4.0	3.53	3.53	293.6	297.13	88	22 Jun	0315
47X	297.6	305.1	7.5	6.98	6.98	297.6	304.58	93	22 Jun	0445
48X	305.1	312.6	7.5	7.64	7.64	305.1	312.74	102	22 Jun	0635
49X	312.6	320.1	7.5	8.96	8.96	312.6	321.56	119	22 Jun	0750
50X	320.1	327.6	7.5	9.47	9.47	320.1	329.57	126	22 Jun	0920
51X	327.6	335.1	7.5	9.71	9.71	327.6	337.31	129	22 Jun	1030
52X	335.1	342.6	7.5	9.28	9.28	335.1	344.38	124	22 Jun	1145
53X	342.6	350.1	7.5	6.86	6.86	342.6	349.46	91	22 Jun	0125
54X	350.1	357.6	7.5	4.56	4.56	350.1	354.66	61	22 Jun	0230
55X	357.6	362.6	5.0	7.63	7.63	357.6	365.23	153	22 Jun	0350
56X	362.6	370.1	7.5	6.57	6.57	362.6	369.17	88	22 Jun	0510
57X	370.1	377.6	7.5	9.80	9.80	370.1	379.90	131	22 Jun	0625
58X	377.6	384.6	7.0	8.93	8.93	377.6	386.53	128	22 Jun	0740
59X	384.6	392.1	7.5	9.78	9.78	384.6	394.38	130	22 Jun	0940
60X	392.1	399.1	7.0	9.36	9.36	392.1	401.46	134	22 Jun	1115
61X	399.1	406.1	7.0	9.66	9.66	399.1	408.76	138	23 Jun	1240
62X	406.1	413.1	7.0	9.14	9.14	406.1	415.24	131	23 Jun	0240
		Totals:	1104.3	1078.45	1078.52					

mbsl based on the core recovery from Core 1H. Coring continued with the APC system to 94.0 mbsf. Cores 7H–11H were partial strokes and were advanced by recovery. The HLAPC system was then deployed to extend the hole to 150.8 mbsf (Cores 12F–24F), with partial strokes on Cores 21F, 22F, and 24F. The XCB coring system was used for Cores 25X–32X to 228.3 mbsf by 0000 h on 16 June. Coring continued to 276.9 mbsf. C_1/C_2 gas headspace ratios were monitored and were in the anomalous zone at 276.9 mbsf. Hole U1618A was terminated, and the gas, temperature, and core data were sent to shore for feedback from the Environmental Protection and Safety Panel

(EPSP) to determine whether coring any deeper at the site could be done in a safe manner. The top drive was set back, and the bit was pulled out of the hole, clearing the seafloor at 1043 h on 16 June.

A total of 37 cores were taken from Hole U1618A (Table **T1**) over a 276.9 m interval with 252.62 m of recovery (91%). The APC system was used for 11 cores over a 94.0 m interval with 90.07 m recovered (96%), the HLAPC system was deployed for 13 cores over a 56.8 m interval with 60.18 m recovered (106%), and the XCB system was deployed for 13 cores over a 126.1 m interval with 102.37 m recovered (81.2%). All APC and HLAPC cores were taken using nonmagnetic core barrels. Temperature measurements were taken on Cores 4H, 7H, 10H, and 13F using the third-generation advanced piston corer temperature (APCT-3) tool. A fifth temperature measurement was taken using the Sediment Temperature 2 (SET2) probe after Core 34X at 249.0 mbsf. In total, we spent 48.50 h (2.1 days) at Hole U1618A.

2.2. Hole U1618B

After clearing Hole U1618A, the vessel was offset 50 m at 139° along Seismic Line CAGE20-5-HH-02-2D to begin operations at Hole U1618B. After careful deliberation, this offset was chosen to move even farther away from a known BSR in the area that was previously identified by IODP's EPSP. A depth reading was taken using the PDR, estimating the seafloor at 1190 mbsl. The top drive was picked up, and the bit was placed at 1189 mbsl for the mudline core. Hole U1618B was spudded at 1245 h on 16 June 2024. The seafloor was calculated to be 1195.2 mbsl based on recovery from Core 1H. Cores 1H–13H were cored with the APC system to 112.8 mbsf. Partial strokes were recorded for Cores 6H, 8H, and 13H. A shattered liner on Core 7H required that the core be pumped out of the core barrel. The HLAPC was deployed for Core 14F from 112.8 to 117.5 mbsf. The decision was made to revert to the APC system for Core 15H. This core was a partial stroke and only advanced from 117.5 to 117.7 mbsf, signaling APC refusal had been reached. Permission was received from EPSP to deepen Hole U1618B past the total depth of Hole U1618A (276.9 mbsf) as long as the headspace C_1/C_2 ratios in this hole remained normal. The hole was advanced with the XCB coring system for Cores 16X–54X, deepening the hole from 117.5 mbsf to the total depth of 414.3 mbsf. At this depth, the C_1/C_2 ratio jumped sharply into the anomalous zone, outside our safety envelope, causing coring to be terminated at 1300 h on 19 June. It was decided to attempt downhole wireline logging in Hole U1618B instead of Hole U1618C (see below) because Hole U1618A had to be terminated prematurely for anomalous C_1/C_2 ratios and higher hydrocarbons. Hence, the future of a potential Hole U1618C was uncertain.

A total of 54 cores were taken from Hole U1618B (Table **T1**) over a 414.3 m interval with 375.24 m recovered (90.57%). The APC system was used for 14 cores over a 113.0 m interval with 112.48 m recovered, the HLAPC system was deployed for 1 core over a 4.7 m interval with 1.63 m recovered (35%), and the XCB system was deployed for 39 cores over a 296.6 m interval with 261.13 m recovered (88%).

All cores collected with the APC and HLAPC systems were taken using nonmagnetic core barrels. Two temperature measurements were attempted using the SET2 temperature probe. The first, after Core 403-U1618B-40X, returned with no data. The second attempt, after Core 41X, returned a good temperature reading from 325.0 mbsf.

2.3. Hole U1618C

The vessel was offset 25 m northwest at a bearing of 319° from Hole U1618B, halfway back toward Hole U1618A, and the bit was lowered to 1194 mbsl. An APC core barrel was deployed, and Hole U1618C was spudded at 1012 h on 20 June 2024. The seafloor was calculated to be 1195.8 mbsl based on recovery from Core 1H. Cores 1H–12H were APC cored to 91.7 mbsf, with partial strokes recorded on Cores 4H, 5H, and 8H–12H. The APC and HLAPC systems were deployed from 91.7 to 125.6 mbsf (Cores 13F–19H), with one drilled interval (161) from 107.9 to 109.9 mbsf. Partial strokes were recorded on Cores 14H and 19H. The XCB coring system was deployed to extend the hole from 125.6 mbsf to the total depth of 392.1 mbsf (Cores 20X–59X) at 0000 h on 23 June. Advances of 7.0–7.5 m were used on the majority of the XCB cores to allow for gas expansion within the core liner. Cores 60X–62X were retrieved from 392.1 to 413.1 mbsf, the final depth for

the hole. Some of the XCB cores expanded upon recovery. The decision to advance by 7–7.5 m to allow for core expansion was kept in place. The C_1/C_2 ratios for Cores 61X and 62X plotted significantly outside of our safety envelope; thus, the decision was made to end the hole. Although a few cores higher in the hole had an anomalous C_1/C_2 ratio, Cores 61X and 62X had an additional presence of higher hydrocarbons. Hole U1618C reached a maximum penetration of 413.1 mbsf with a cored interval of 411.1 m and a recovery of 450.59 m (109.61% recovery). The pipe was pulled from the hole, and the bit cleared the rig floor at 1120 h. While pulling the pipe, the beacon was recovered at 0945 h. The rig floor was secured for transit, the vessel switched from DP mode to cruise mode, and the vessel was underway to Site U1619 at 1151 h on June 23.

A total of 61 cores were taken from Hole U1618C (Table **T1**) over a 411.1 m interval with 450.59 m recovered (109.61%). The APC system was used for 14 cores over a 113.0 m interval with 112.48 m recovered, the HLAPC system was deployed for 3 cores over a 14.1 m interval with 13.71 m recovered (97.3%), and the XCB coring system was deployed for 43 cores over a 287.5 m interval with 337.18 m recovered (114.82%).

2.4. Downhole logging

After concluding coring operations in Hole U1618B, the bit was pulled to 68.6 mbsf and the Schlumberger wireline was rigged up. The triple combo logging tool string was made up and deployed at 1645 h on 19 June 2024, reaching 373.3 mbsf on the first pass and 368.3 mbsf on the second. The tools were recovered, and the Formation MicroScanner (FMS)-sonic logging tool string was made up and deployed at 0300 h on 20 June. The tools reached 358.8 mbsf on the first pass and 342.8 mbsf on the second. The tools were recovered, and the Versatile Seismic Imager (VSI) tool string was made up and deployed at 0445 h on 20 June. While deploying the tool, it was noticed that the *Z*-axis was not transmitting data. The tools were recovered, and the backup VSI tool was made up and deployed. While powering up the backup tool, a power surge caused a failure in the electronics. With both VSI tool strings inoperable, it was decided to end logging operations for the hole. The Schlumberger equipment was rigged down, and the rig floor was cleared. The bit was pulled out of the hole, clearing the seafloor at 0740 h on 20 June and ending Hole U1618B. In total we spent 93.0 h (3.9 days) at Hole U1618B.

3. Lithostratigraphy

The recovered sequence at Site U1618 consists of 152 cores and 1078.4 m of sediment that exhibits increasing lithification with depth. The sediments throughout all cores from Holes U1618A–U1618C are primarily siliciclastic, mainly composed of dark gray to greenish black silty clay, with interbedded coarser intervals, such as clayey silt, and rarely sandy mud, gravel, and diamicton intervals (Figure **F3A, F3B, F3F**). These lithologies contain varying amounts of detrital clasts and/or authigenic mineral precipitants. Small (<2 cm) to large (>2 cm) clasts are identified throughout the cores from visual descriptions and X-radiograph observations, when available (Figure **F3C–F3E**). When present, clast abundance ranges from dispersed (observed on <1% of the split core surface) to common (1%–5%) to abundant (5%–30%). When the sediment is poorly sorted, with clast abundance between 1% and 30% and large clasts (>2 cm) present, the lithology is designated as a diamicton (Figure **F3F**). Authigenic mineral precipitants range in size from micrometer-scale to 2–3 cm diameter concretions (Figure **F4A, F4B**). Although sometimes not visible on the split core surfaces (i.e., described as structureless), primary (e.g., laminations and bioturbation) and secondary (e.g., bioturbated infilling by authigenic dense minerals) sedimentary structures are more commonly visible in the X-radiographs available from Hole U1618B and the deeper part of Hole U1618C (Figures **F4C**, **F5**, **F6**). Clasts of varying sizes, interpreted to be ice-rafted debris (IRD), are observed throughout all lithostratigraphic units, with lesser abundance in Lithostratigraphic Unit II. The majority of these clasts are angular to subangular and smaller than 1–2 cm in size, but larger (>2 cm) clasts are also occasionally observed. Most of the clasts consist of siltstones, mudstones, and igneous rocks, but metamorphic rocks are also evident.

Based on these characteristics, the sediments recovered from Site U1618 are divided into three primary lithostratigraphic units and additional subunits (Table **T2**). The relatively continuous

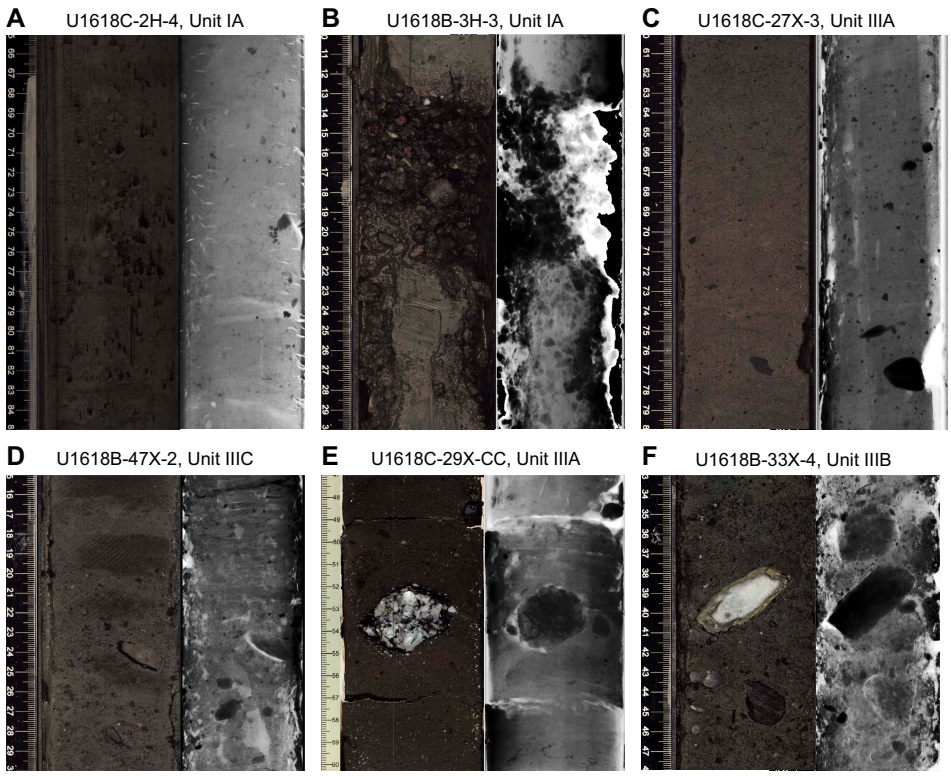

Figure F3. Paired core photographs (left) and X-radiographs (right; black = high density) showing typical lithologies, Holes U1618B and U1618C. A. Structureless silty clay. B. Gravel layer. C. Silty clay with common clasts. D. Transition from sandy mud with abundant clasts (bottom) into slightly bioturbated clay. E. Large clast (>3 cm). F. Muddy diamicton with large clasts.

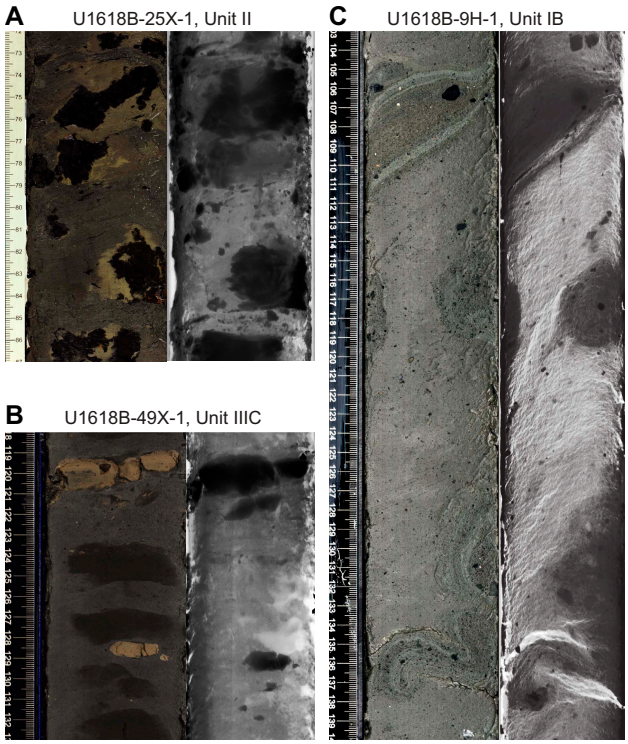

Figure F4. Paired core photographs (left) and X-radiographs (right; black = high density) showing sedimentologic features, Hole U1618B. A. Authigenic iron sulfides nodules. B. Authigenic carbonate concretions. C. Debrite with contorted muddy clasts and layers in a muddy matrix.

Hole U1618C is used as the primary record to define the lithostratigraphic unit and subunit boundaries. The stratigraphic boundaries in Hole U1618C are subsequently transferred to Holes U1618A and U1618B based on stratigraphic correlation on the mbsf (equivalent to CSF-A) scale (see **Stratigraphic correlation**) (Figure **F7**).

The degree of core recovery, coring disturbance, and gas expansion varies with the depth of the cores and the type of coring method employed. APC cores from Holes U1618A–U1618C exhibit minimal disturbance, although low recovery or fracturing is observed beginning around 50–60 mbsf in all holes, with decreased recovery below this depth. Soupy intervals are noted in the upper sections of the first two to three cores from each hole and often result in mixed sediments. Most XCB cores from all holes are moderately to heavily disturbed, primarily by biscuiting, which mainly affects silty clay intervals. Coarser grained intervals appear to be more resistant to disturbance, preventing them from becoming severely biscuited.

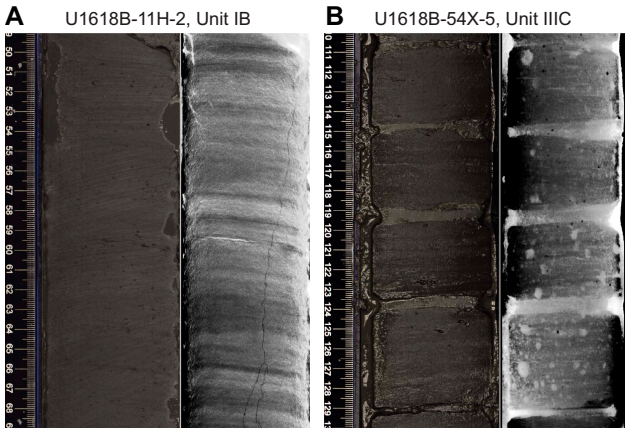

Figure F5. Paired core photographs (left) and X-radiographs (right; black = high density) showing laminations, Hole U1618B. A. Planar laminations. B. Faint lamination in moderately biscuited sediments.

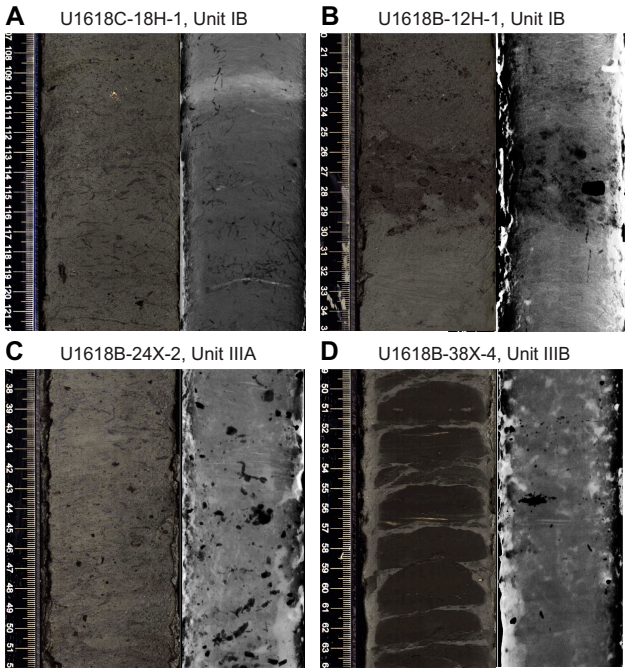

Figure F6. Paired core photographs (left) and X-radiographs (right; black = high density) showing bioturbation, Holes U1618B and U1618C. A, C. Moderate bioturbation with iron-sulfide burrow infillings. B. Bioturbated silty clay and a sandy silt layer with clasts. D. Moderately bioturbated clay in biscuited sediments.

The sediments from Site U1618 exhibit similarities to those from the nearest ODP site location (Site 912; Shipboard Scientific Party, 1995). However, lithologic analysis of X-radiographs, coupled with the physical property and geochemical data, revealed new notable information in sediment characteristics.

3.1. Lithostratigraphic unit descriptions

3.1.1. Unit I

Intervals: 403-U1618A-1H-1 through 23F-CC; 403-U1618B-1H-1 through 19X-CC; 403-U1618C-1H-1 through 23X-1
Depths: Hole U1618A = 0–148.87 mbsf; Hole U1618B = 0–152.20 mbsf; Hole U1618C = 0–148.05 mbsf
Age: Pleistocene to Holocene

The sediment in Lithostratigraphic Unit I is predominantly soft to firm dark gray (2.5Y 4/1) to very dark gray (N 3/) silty clay with frequent intervals of coarser clayey silt/sandy mud, occasional greenish gray (e.g., 10GY 5/1) and dark reddish gray (10R 3/1) intervals, and gravels that mostly occur in the upper part of the unit. The lower contacts of the sandy mud intervals are sometimes irregular with grading, suggesting turbidite-type gravitational flow deposition. Based on visual observations of the split core surface and examination of X-radiographs, the presence of gravel- to pebble-sized clasts is highly consistent. There is an abundance of small clasts (<1–2 cm) ranging from dispersed to abundant throughout the unit. In the lower part of the unit, the sediment displays the occasional occurrence of diamicton and laminated intervals, with slight to moderate bioturbation (Figures **F5A**, **F6A, F6B**). Debrite-type sediments are visible on both the split core surface and the X-radiographs (Figure **F4C**).

The most common minerals observed in smear slides are quartz and clay, accompanied by a considerable number of rock fragments and a relatively low concentration of heavy minerals, feldspar, and other minerals (Figure **F8**). Glauconite is also occasionally recognized. The biogenic component of the sediment is typically less than 2%, except in a few intervals that are dominated by calcareous nannofossils.

Table T2. Summary of lithostratigraphic units and subunits, Site U1618. BOH = bottom of hole. Information regarding lithostratigraphic characteristics taken mainly from Hole U1618C. This hole also serves as the primary reference for defining lithostratigraphic units and subunits. Its boundaries are then extrapolated to Holes U1618A and U1618B through stratigraphic correlations on the CSF-A scale. **Download table in CSV format.**

Lith. unit	Defining lithologic characteristics	Depth interval base CCSF-A (m)	Bottom core, section, interval (cm)	Interval depth range CSF-A (m)	Age
			403-		
IA	Soft sediments that consist of silty clay with coarser clayey silt/sandy mud, and occasional greenish gray and dark reddish gray intervals. No to slight bioturbation.	60.65	U1618A-7H-CC U1618B-8H-1, 81 U1618C-7H-CC	0–55.10 0–58.51 0–59.19	Holocene to Pleistocene
IB	Transition to firmly indurated sediments. Bioturbation increases, and diamictons and laminations occur. Lithology similar to Subunit IA but with the presence of authigenic carbonate.	156.52	U1618A-23F-CC U1618B-19X-CC U1618C-23X-1	61.90–48.87 58.51–152.20 59.19–148.05	Pleistocene
II	Predominantly silty clay. Bioturbation more variable than Unit I. No diamictons and no to rare laminations. Increased voids and fractures throughout. Small amounts of authigenic iron sulfide minerals (greigite and/or pyrite).	199.93	U1618A-29X-1, 46 U1618B-23X-4, 78 U1618C-29X-3	148.87–189.56 156.90–190.60 148.05–186.65	Pleistocene
IIIA	Higher amount of silty clay to clay compared to Subunits IIIB and IIIC. Slight to heavy bioturbation. Significant authigenic iron sulfide grains (mm to cm scale).	245.96	U1618A-32X-CC U1618B-29X-3, 15 U1618C-35X-CC	189.56–224.21 190.60–228.81 186.65–230.07	Pleistocene
IIIB	Occurrence of diamictons and laminated sediments. Relatively low abundance of iron oxide grains. Bioturbation slight to heavy from the top to the middle and slight to none toward the base.	357.08	U1618A: BOH U1618B-41X-CC U1618C-49X-CC	228.30–BOH 228.81–323.19 230.07–321.56	Pleistocene
IIIC	Laminations common, and diamictons are occasionally present in the upper half. Bioturbation is slight to none. Defined by the return of significant authigenic iron sulfide grains (mm to cm scale).	—	U1618B: BOH U1618C: BOH	323.30–BOH 321.56–BOH	Pleistocene to Pliocene

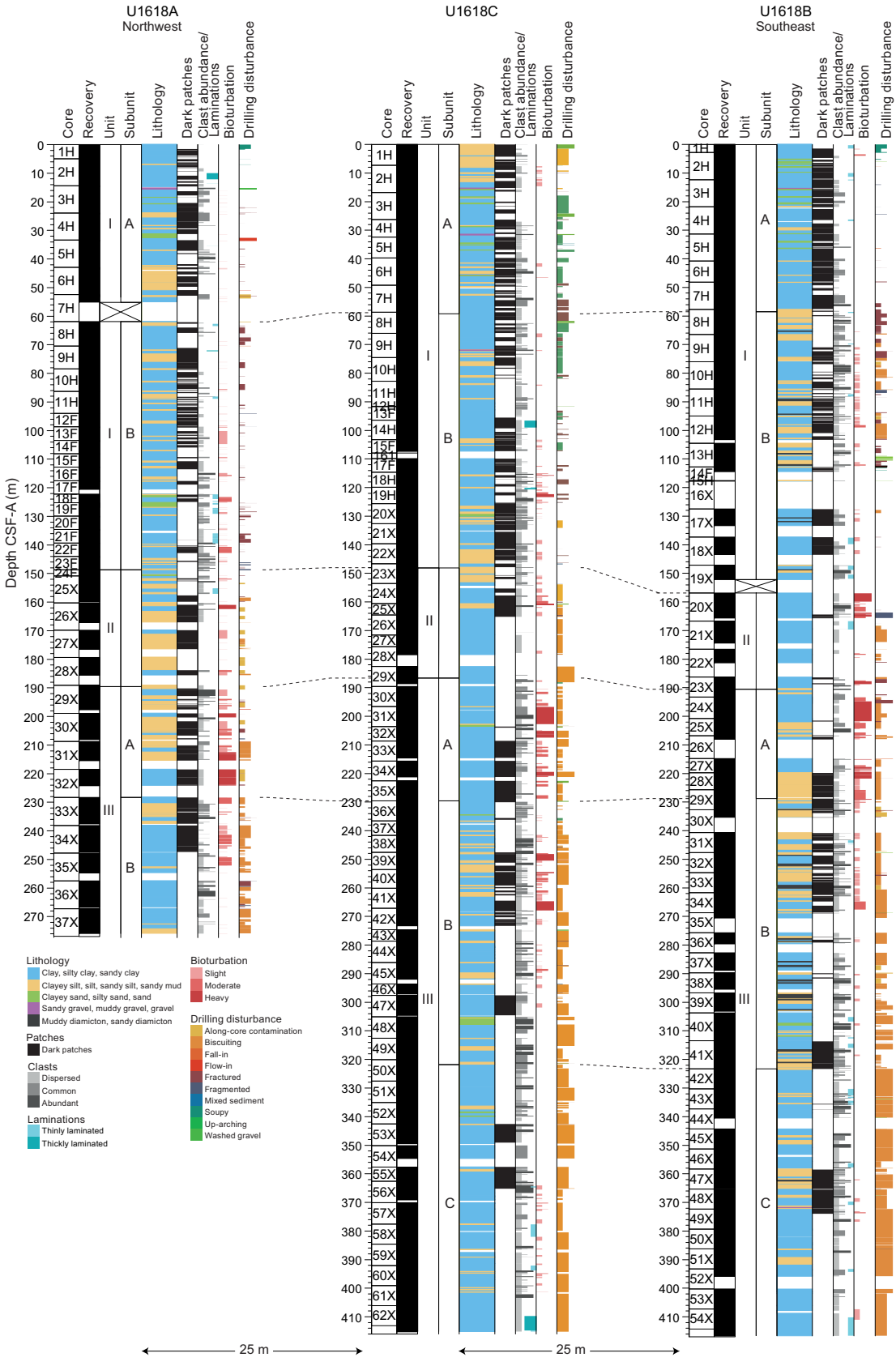

Figure F7. Lithostratigraphic correlation, Site U1618. Unit and subunit boundaries are displayed in relation to their location at section breaks and within core sections rather than at the corresponding depth because overlapping sections occurred due to gas expansion and are not correctly displayed on the CSF-A depth scale. Core lithology is simplified by grouping (silty/sandy) clay and clay; (clayey/sandy) silt, silt and sandy mud; (clayey/silty) sand and sand; (sandy/muddy) gravel and gravel; and (muddy/sandy) diamicton. Clast abundance, laminations, degree of bioturbation, and degree of drilling disturbance are all color coded and shown as histograms.

Unit I can be divided into two subunits (IA and IB) based on the different occurrence of diamicton and intense lamination in the lower part of the sediment sequence, in addition to the presence of bioturbation, variations in color, and physical properties. This subunit boundary is located at the bottom of Core 403-U1618A-7H (55.10 mbsf); in Section 403-U1618B-8H-1, 81 cm (58.51 mbsf); and at the bottom of Core 403-U1618C-7H (59.19 mbsf) (Table **T2**).

3.1.1.1. Subunit IA

Intervals: 403-U1618A-1H-1 through 7H-CC; 403-U1618B-1H-1 through 8H-1, 81 cm; 403-U1618C-1H-1 through 7H-CC
Depths: Hole U1618A = 0–55.10 mbsf; Hole U1618B = 0–58.51 mbsf; Hole U1618C = 0–59.19 mbsf

Lithostratigraphic Subunit IA is the youngest in the stratigraphic sequence and is characterized by relatively soft and soupy sediments compared to Subunit IB, especially in the uppermost cores, and is less bioturbated overall. The first few cores of this subunit have higher a* and b* color index values compared to the other subunits (Figures **F9**, **F10**, **F11**). Subunit IA has a greater percentage of sand (e.g., sandy mud) (Figure **F12**) and more recurrent intervals with abundant clasts. Biogenic material generally comprises <2% of the composition, with several intervals exceeding 10%, and there is no visual evidence of diagenesis. Laminations occasionally occur. Subunit IA is also characterized by a general increase in natural gamma radiation (NGR) values toward the bottom, which is possibly associated with increased clast abundance as observed at the bottom of the subunit in Holes U1618B and U1618C.

3.1.1.2. Subunit IB

Intervals: 403-U1618A-8H-1 through 23F-CC; 403-U1618B-8H-1, 81 cm, through 19X-CC; 403-U1618C-8H-1 through 23X-1
Depths: Hole U1618A = 61.90–148.87 mbsf; Hole U1618B = 58.51–152.20 mbsf; Hole U1618C = 59.19–148.05 mbsf

Lithostratigraphic Subunit IB is slightly more consolidated than Subunit IA, slightly to moderately bioturbated in many cores, and shows lower a* and b* values than Subunit IA. In addition, this subunit is more fractured, with many void intervals, likely related to sediment degassing. Diamicton and laminated intervals are observed. Formation of large authigenic calcite grains is evident in the lowermost part of the subunit.

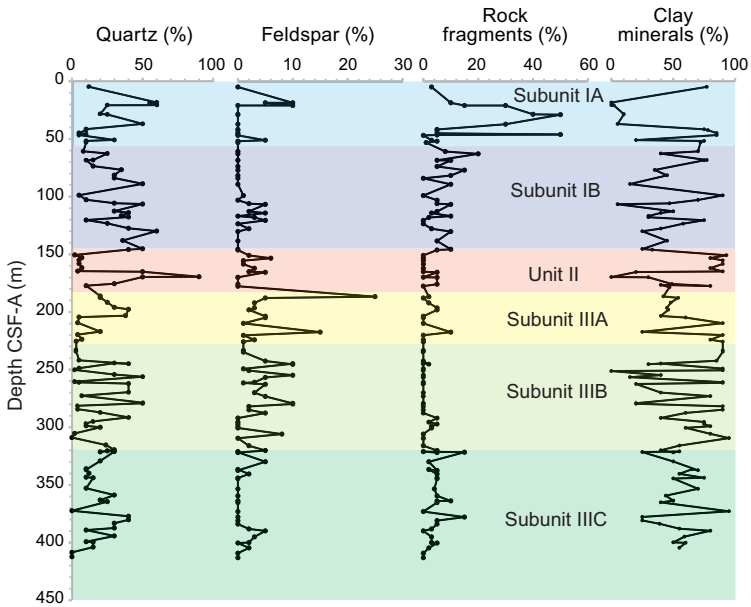

Figure F8. Downhole mineralogy from smear slide analysis, Hole U1618C.

3.1.2. Unit II

Intervals: 403-U1618A-24F-1 to 29X-1, 46 cm; 403-U1618B-20X-1 to 23X-4, 78 cm; 403-U1618C-23X-2 through 29X-3
Depths: Hole U1618A = 148.87–189.56 mbsf; Hole U1618B = 156.95–190.60 mbsf; Hole U1618C = 148.05–186.65 mbsf
Age: Pleistocene

Lithostratigraphic Unit II is also predominantly dark gray (N 3/) to greenish black (10Y 2.5/1) silty clay and is characterized by relatively firmer induration. Intervals of clayey silt and sandy mud are less common than in Unit I. Based on visual core observations and X-radiographs, the presence of small to large clasts is evident, but their occurrence is less frequent than in Unit I. Diamicton is not observed. This unit is also characterized by frequent occurrence of voids and fractures, which is likely related to sediment degassing.

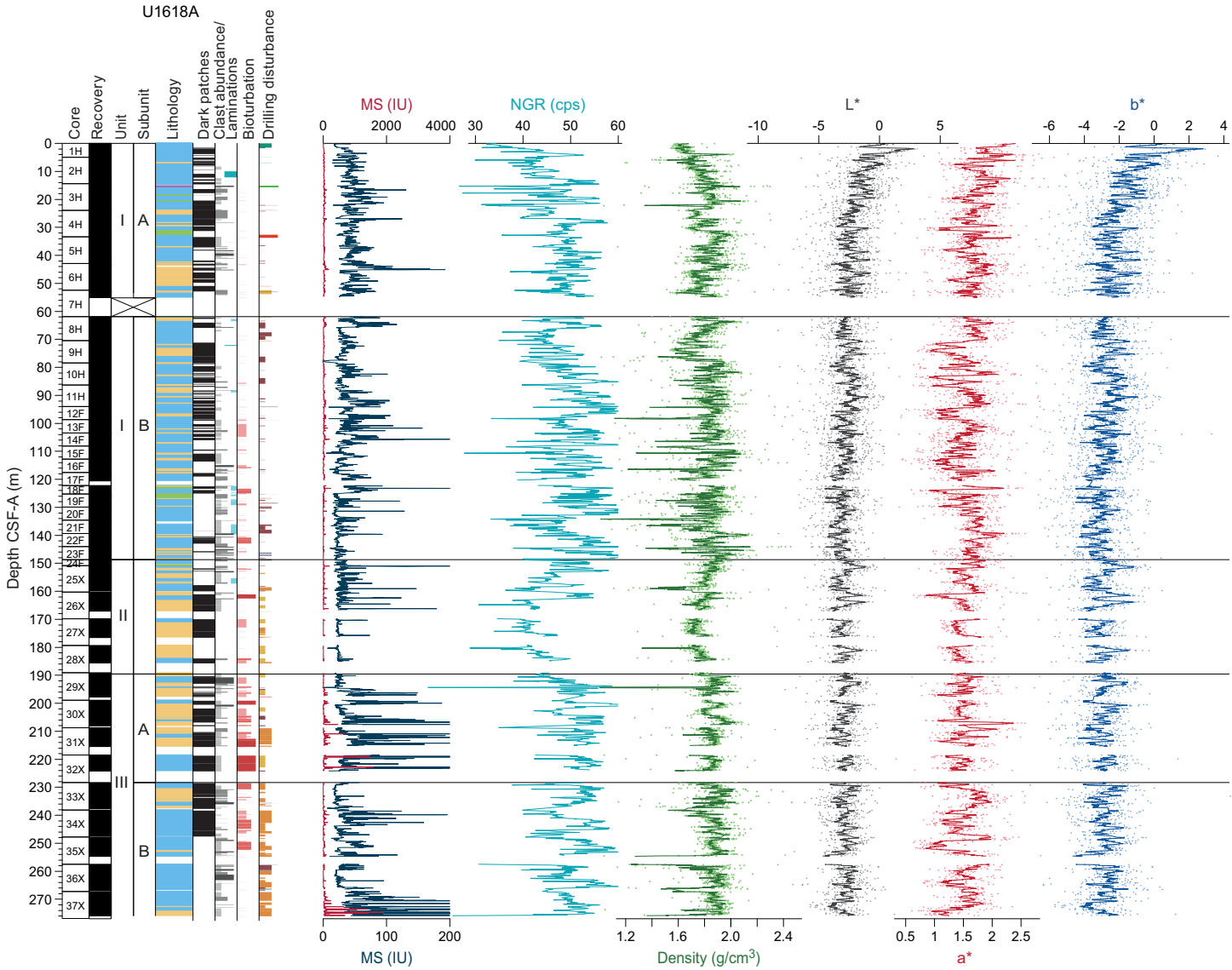

Figure F9. Physical properties, Hole U1618A. Whole-round MS is shown in two different scales, red [0–4000 IU] to display the full range observed, highlighting the high values related to iron sulfide minerals, and blue [0–200 IU] to display the variability of the sediment where iron sulfide minerals are not dominant. Density and CIELAB L*, a*, and b* are displayed as dots superimposed with an 11-point running mean. Unit and subunit boundaries are displayed in relation to their location at section breaks and within core sections rather than at the corresponding depth because overlapping sections occurred due to gas expansion and are not correctly displayed on the CSF-A depth scale. cps = counts per second. For lithology legend see Figure F7.

The most common minerals observed in smear slides are quartz and clay. In addition, occurrences of rock fragments, heavy minerals, opaque minerals, and glauconite are observed. Unit II is typified by limited bioturbation. The biogenic component of the sediment is 0%–1%. In addition to the authigenic carbonate, authigenic iron sulfide minerals are observed in this unit (as inferred from smear slide observations on the split core surface and X-radiographs) (Figure **F4A**).

Unit II has increased variability in magnetic susceptibility (MS), which most likely corresponds to authigenic iron sulfide minerals. This unit has generally lower NGR and lower gamma ray attenuation (GRA) density (especially Hole U1618A; Figure **F9**) than the other units. The upper boundary of Unit II is likely to be consistent with Seismic Reflector R5.

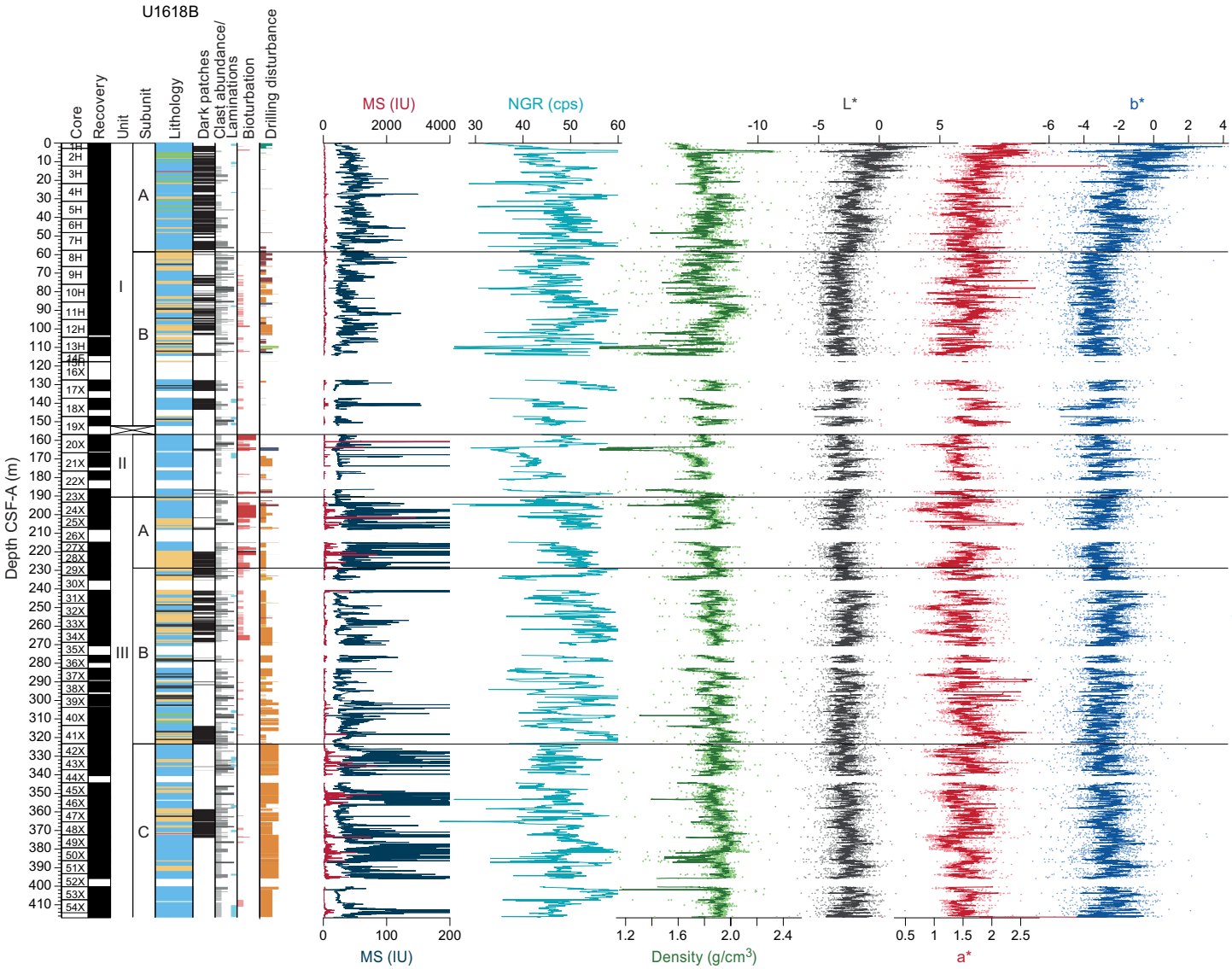

Figure F10. Physical properties, Hole U1618B. Whole-round MS is shown in two different scales, red [0–4000 IU] to display the full range observed, highlighting the high values related to iron sulfide minerals, and blue [0–200 IU] to display the variability of the sediment where iron sulfide minerals are not dominant. Density and CIELAB L*, a*, and b* are displayed as dots superimposed with an 11-point running mean. Unit and subunit boundaries are displayed in relation to their location at section breaks and within core sections rather than at the corresponding depth because overlapping sections occurred due to gas expansion and are not correctly displayed on the CSF-A depth scale. For lithology legend see Figure F7. cps = counts per second.

3.1.3. Unit III

Intervals: 403-U1618A-29X-1, 46 cm, to the bottom of the hole; 403-U1618B-23X-4, 78 cm, to the bottom of the hole; 403-U1618C-29X-4 to the bottom of the hole
Depths: Hole U1618A = 189.56–276.9 mbsf; Hole U1618B = 190.60–414.3 mbsf; Hole U1618C = 186.65–413.1 mbsf
Age: Pliocene to Pleistocene

The sediment in Lithostratigraphic Unit III is predominantly firm dark gray (5Y 4/1) to greenish black (5GY 2.5/2) silty clay with frequent clayey silt/sandy mud intervals and occasional diamicton intervals. The lower contacts of these coarser intervals are sometimes sharp or erosional, suggesting gravitational flow deposition. There is a slight increase in quartz, feldspar, mica, and opaque minerals as observed in smear slides compared to Units I and II and an increase in smectite toward the bottom of the record (Figure **F13**) based on X-ray diffraction (XRD). The biogenic component of the sediment is generally low (<3%), although there are several intervals exceeding 5%. The

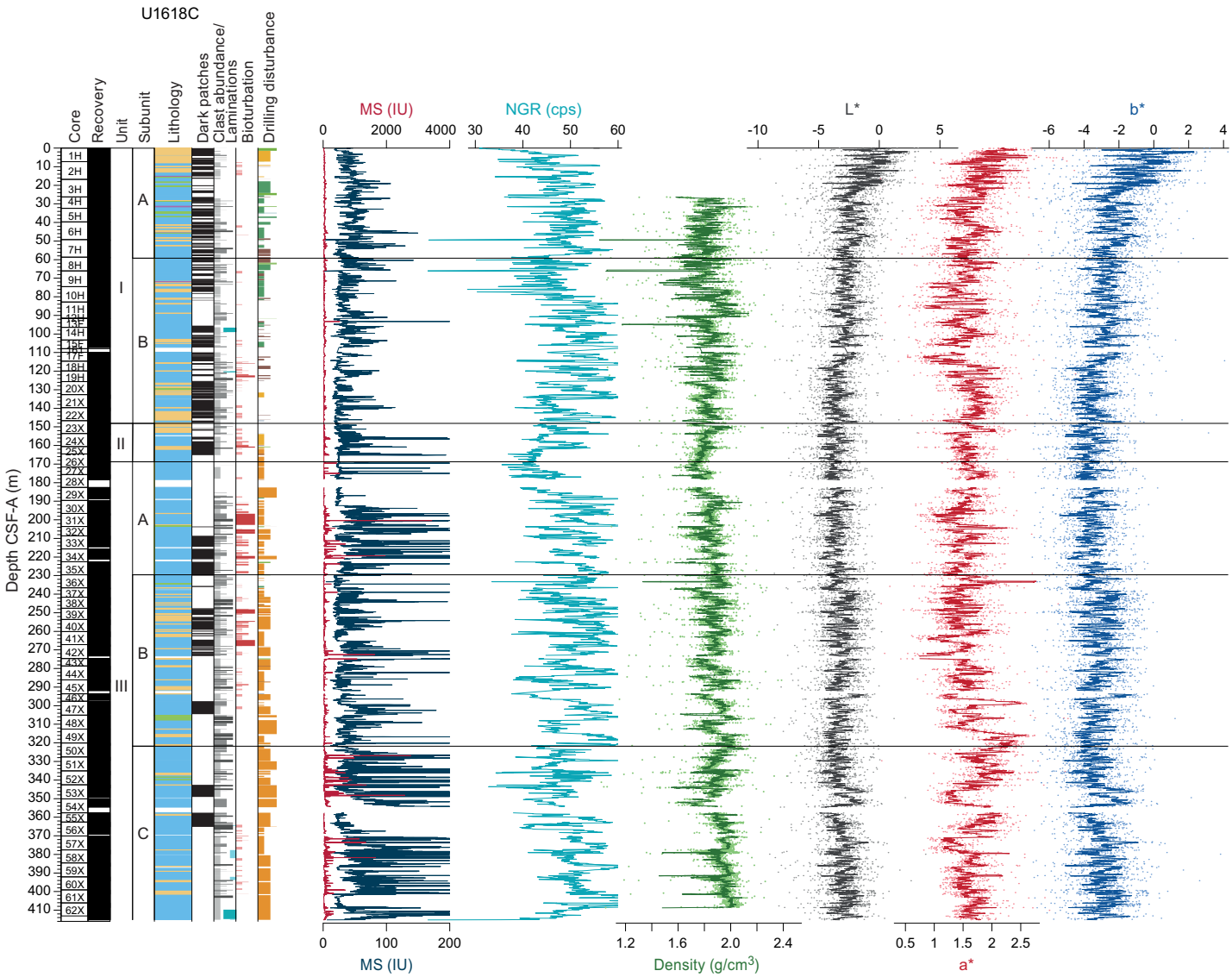

Figure F11. Physical properties, Hole U1618C. Whole-round MS is shown in two different scales, red [0–4000 IU] to display the full range observed, highlighting the high values related to iron sulfide minerals, and blue [0–200 IU] to display the variability of the sediment where iron sulfide minerals are not dominant. Density and CIELAB L*, a*, and b* are displayed as dots superimposed with an 11-point running mean. Unit and subunit boundaries are displayed in relation to their location at section breaks and within core sections rather than at the corresponding depth because overlapping sections occurred due to gas expansion and are not correctly displayed on the CSF-A depth scale. For lithology legend see Figure F7. cps = counts per second.

upper boundary of Unit III is marked by a significant increase in authigenic iron sulfide minerals compared to Unit II.

The occurrence of diamicton and lamination and the degree of bioturbation, in addition to variations in the abundance of iron sulfide minerals, allows for the division of Unit III into three

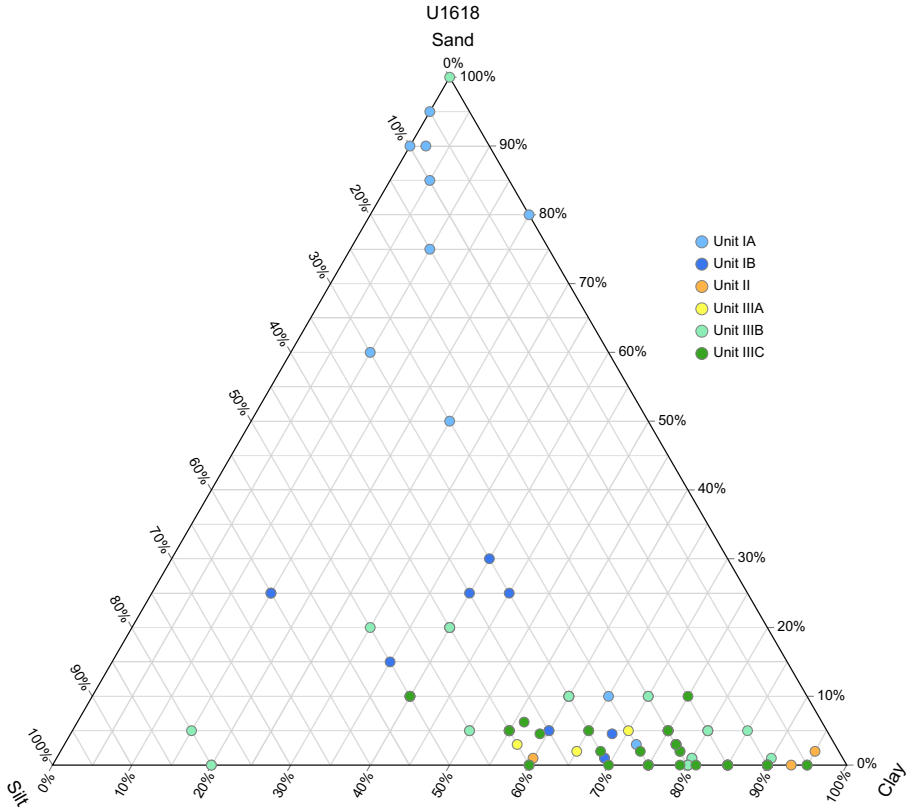

Figure F12. Ternary diagram of sand (top), silt (bottom left), and clay (bottom right) percentages of sediment as inferred from smear slides, Hole U1618C.

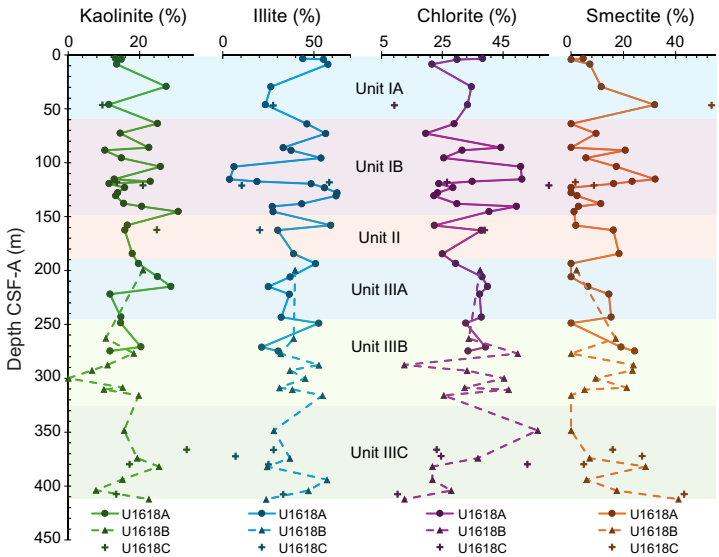

Figure F13. XRD results, Site U1618. Calculated relative abundances of different clay minerals are shown. Visual core descriptions for Holes U1618A–U1618C show lithologic changes downhole.

subunits (IIIA–IIIC). The boundary between Subunits IIIA and IIIB likely corresponds to Seismic Reflector R6.

3.1.3.1. Subunit IIIA

Intervals: 403-U1618A-29X-1, 46 cm, through 32X-CC; 403-U1618B-23X-4, 78 cm, through 29X-3, 15 cm; 403-U1618C-29X-4 through 35X-CC
Depths: Hole U1618A = 189.56–224.21 mbsf; Hole U1618B = 190.60–228.81 mbsf; Hole U1618C = 186.65–230.07 mbsf

Lithostratigraphic Subunit IIIA has a higher contribution of clayey silt compared to Subunits IIIB and IIIC in Holes U1618A and U1618B, but this is not observed in Hole U1618C (Figure **F7**). This subunit is also characterized by ranging degrees of bioturbation generally from slight to heavy (Figure **F6C**). The biogenic fraction is absent to low (3%) throughout. The occurrence of larger clasts (>2 cm) is also more common in Subunit IIIA (and Subunit IIIB) compared to Subunit IIIC and includes a variety of rock types. Subunit IIIA is characterized by significant authigenic iron sulfide minerals based on observations of the split core surface, X-radiographs, smear slides, bulk XRD mineralogy, and extreme peaks in MS (e.g., Figures **F9**, **F10**, **F11**).

3.1.3.2. Subunit IIIB

Intervals: 403-U1618A-33X-1 to the bottom of the hole; 403-U1618B-29X-3, 15 cm, through 41X-CC; 403-U1618C-36X-1 through 49X-CC
Depths: Hole U1618A = 224.21 mbsf to the bottom of the hole; Hole U1618B = 228.81–323.19 mbsf; Hole U1618C = 230.07–321.56 mbsf

Predominantly a silty clay to clayey silt, Lithostratigraphic Subunit IIIB is characterized by the additional occurrence of diamicton and laminated sediments and a reduced abundance of authigenic iron sulfide minerals, which corresponds well to the observed reduction in the number of extreme MS values. Bioturbation is slight to heavy in the upper part of the subunit (Figure **F6D**) and decreases in the lower part. Biogenic components are low throughout much of Subunit IIIB, with few intervals having more than 5% biogenics. The occurrence of clasts is similar to the other Unit III subunits.

3.1.3.3. Subunit IIIC

Intervals: 403-U1618B-42X-1 to the bottom of the hole; 403-U1618C-50X-1 to the bottom of the hole
Depths: Hole U1618B = 323.19 mbsf to the bottom of the hole; Hole U1618C = 321.56 mbsf to the bottom of the hole

Like Lithostratigraphic Subunit IIIA, Subunit IIIC is predominantly a silty clay to clayey silt. Based on X-radiographic inspection, Subunit IIIC contains diamicton intervals near the top (e.g., Core 403-U1618B-43X), and laminations are common, especially toward the bottom (Figure **F5B**). This subunit is characterized by significant authigenic iron sulfide minerals that are visible as abundant dark concretions and significant peaks in MS, similar to Subunit IIIA. Authigenic carbonate is present (Figure **F4B**). Based on X-radiograph observation, bioturbation is generally absent to slight.

3.2. X-ray diffraction

XRD analyses were used to characterize the clay mineral assemblage made of kaolinite, illite, smectite, and chlorite (Figure **F13**). The relative abundance of kaolinite ranges between 10% and 41% (standard deviation [SD] = 7.21), with higher but fluctuating values observed within Lithostratigraphic Unit I and Subunit IIIC and lower values from the top of Unit II to the base of Subunit IIIB. Illite varies from 4% to 63% (SD = 15.04; 1σ), showing minimal variation throughout the units, except for a significant reduction in Subunit IB at ~110 mbsf. Smectite varies from 0% to 54% (SD = 12.52) and shows an increase toward the base of Subunit IIIC. Chlorite varies from 9% to 60% (SD = 11.54), exhibiting high variability in Subunit IB and a gradual decrease in relative abundance toward the base of Subunit IIIC.

Table T3. Mineralogical composition of samples selected for bulk XRD analysis, Site U1618. Percentages quantified using HighScore Plus. **Download table in CSV format.**

Core, section, interval (cm)	Top depth CSF-A (m)	Bottom depth CSF-A (m)	Mineral	Percentage (%)	Chemical formula
403-U1618A-					
3H-7, 36–37	20.72	20.73	Beryllium fluoride	100	$Be_{0.94}F_{1.88}$
11H-6, 0–1	92.81	92.82	Calcium carbonate	100	$Ca(CO_3)$
403-U1618B-					
25X-1, 83–84	201.63	201.64	Greigite	92.1	Fe_3S_4
			Iron sulfide	0.5	FeS
			Siderite (calcium-magnesium-bearing)	7.5	$Ca_{0.10}Mg_{0.33}Fe_{0.57}(CO_3)$
43X-4, 104–105	335.52	335.53	Quartz	100	SiO_2
403-U1618C-					
30X-3, 90–92	193.40	193.42	Iron sulfide (nickel-bearing)	65.7	$Fe_{0.996}Ni_{0.004}S_2$
			Quartz	17.5	SiO_2
			Pyrite	16.8	FeS_2
62X-2, 62–63	407.86	407.87	Quartz	10.4	SiO_2
			Albite	89.6	$Na_{0.98}Ca_{0.02}Al_{1.02}Si_{2.98}O_8$

Additionally, bulk XRD analysis of select powdered samples confirms that clay minerals and quartz comprise the primary composition of the representative silty clay lithologies (Table **T3**). It also confirms the compositions of the suspected authigenic mineralogic components such as iron sulfides and iron carbonate (e.g., greigite, pyrite, and siderite) in Sample 403-U1618B-25X-1, 83–84 cm, and calcium carbonate ($CaCO_3$) in Sample 403-U1618A-11H-6, 0–1 cm.

3.3. Preliminary interpretation

The occurrence of diamicton intervals and laminated sediments in Lithostratigraphic Unit III suggests an early glacial influence and a proximal location of an ice sheet or glacier to the drilled site during the Late Pliocene/Early Pleistocene. In addition, rhythmic changes in color and/or texture observed over the drilled sequences are likely to be related to climatic changes such as orbitally driven glacial–interglacial cycles. The absence of diamicton and fewer terrigenous clasts in Unit II may indicate an extended period of distal depositional conditions of the drilled site with respect to the glacial terminus. Unit I sediments comprise repeated sequences of bioturbated silty clay intervals that alternate with intervals of dispersed to abundant (1%–30%) clasts, which are preliminarily interpreted as IRD. The IRD-rich intervals are often alternating with thin laminations (<0.3 cm) and intervals of diamicton occurring in Subunit IB. The lithostratigraphic sequence suggests dynamic shifts between proximal to distal positions relative to the ice sheet associated with the alternation of Late Pleistocene glacial and interglacial periods. The composition of clasts (sandstone, mudstone, etc.) indicates that the IRD may have been predominantly delivered from Fennoscandia, including Svalbard and the Barents Sea shelf.

4. Biostratigraphy and paleoenvironment

Site U1618 sediments were examined for calcareous nannofossils, planktonic foraminifers, diatoms, and dinoflagellate cysts (dinocysts). None of these microfossil groups are consistently present throughout the sediment column, and several levels are barren (Figure **F14**).

Diatoms are present at the very top and only sporadically downcore. Planktonic foraminifers are present in the upper part but disappear downcore. Calcareous nannofossils are also generally present, but toward the base of the hole the record is mainly barren. Dinocysts are present throughout the sediment column but are absent occasionally. All groups combined, especially with calcareous nannofossils and dinocysts, contribute to a first biostratigraphic and paleoenvironmental assessment and an age-depth model for Site U1618 (Figure **F15**; Table **T4**).

The age model for Site U1618 is based on a combination of biostratigraphical and paleomagnetic data. A total of three calibrated calcareous nannofossil events were identified across the three holes at Site U1618: the lowest occurrence (LO) of *Emiliania huxleyi*, the lowest dominant occurrence (LDO) of the small *Gephyrocapsa* group, and the LO of medium *Gephyrocapsa*. The acme of

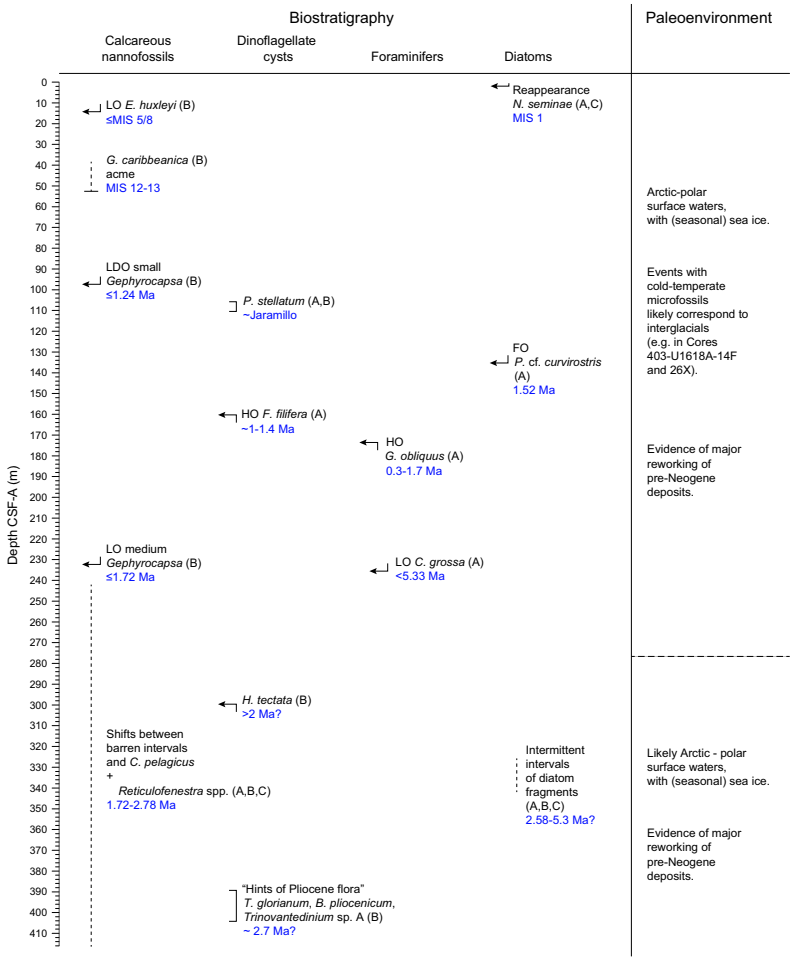

Figure F14. Biostratigraphic summary, Site U1618. Letters in parentheses = hole(s) where the event is observed.

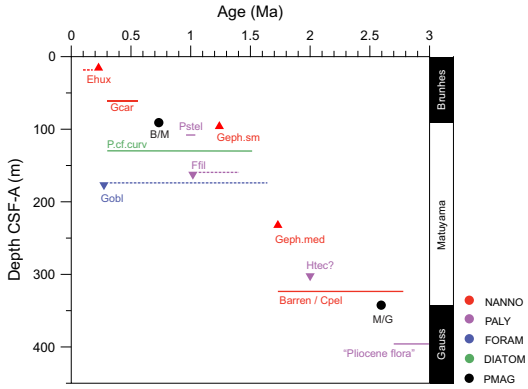

Figure F15. Age-depth model, Site U1618. All encountered biostratigraphic and paleomagnetic datums are shown. Calcareous nannofossils: Ehux = LO *E. huxleyi*, Gcar = acme *G. caribbeanica*, Geph.sm = LDO small *Gephyrocapsa*, Geph.med = LO medium *Gephyrocapsa*, Cpel = *C. pelagicus*. Diatoms: P.cf.curv = HO *P.* cf. *curvirostris*. Dinocysts: Pstel = occurrence of *P. stellatum*, Ffil = HO *F. filifera*, Htec = HO *H. tectata*. Foraminifers: Gobl = LO *G. obliquus*. Paleomagnetic boundaries: B/M = Bruhnes/Matuyama boundary, M/G = Matuyama/Gauss boundary.

Gephyrocapsa caribbeanica indicates a Late Pleistocene age for the upper part of the site. Two dinocyst events, which suggest an age around 1 Ma, were observed: the restricted presence of *Protoperidinium stellatum* and the highest occurrence (HO) of *Filisphaera filifera*. The discontinuous presence of *Coccolithus pelagicus*, together with a rare content of medium *Reticulofenestra* and the tentative HO of the dinocyst *Habibacysta tectata*, suggest an Early Pleistocene age for the lower part of the site. Traces of Late Pliocene flora, such as a few specimens of the dinocysts *Barssidinium pliocenicum* and *Trinovantedinium variabile*, appear near the base of the core and are tentatively interpreted as Late Pliocene. Additionally, the HO of *Globigerinoides obliquus*, the presence of the diatom *Proboscia* cf. *curvirostris*, and the record of the benthic foraminifer *Cibicides grossa* were used to constrain the age-depth model for Site U1618 (Figure **F15**).

The microfossil assemblages generally indicate Arctic–polar surface waters and seasonal sea ice conditions throughout the Quaternary. Polar surface waters are colder and slightly less saline than Arctic water masses, which are defined as a mixture of Polar and Atlantic water masses following definitions of water masses in the Fram Strait today (e.g., Hopkins, 1991). Exceptions are the cold-temperate conditions and Atlantic water incursion during the middle Pleistocene and occasional incursions of temperate waters in the Early Pleistocene. It is likely that there are more warm intervals (interglacials), given our rather low sampling resolution. Little to substantial reworking of pre-Neogene deposits is evident in all microfossil groups.

4.1. Calcareous nannofossils

The biostratigraphy of calcareous nannofossils at Site U1618 is based on the study of 59 core catchers and 268 split core samples taken from Holes U1618A–U1618C. All core catchers from Hole U1618A were examined for calcareous nannofossils (Figure **F16**). Core catchers from Holes U1618B and U1618C were analyzed only for those depths extending beyond the maximum depth in Hole U1618A (Figures **F17**, **F18**). Split core samples were routinary selected in all cores from Holes U1618A–U1618C based on the visual examination of sediments and physical properties (i.e., changes in color and MS).

Calcareous nannofossils at Site U1618 evidence a discontinuous representation along the studied sequence. The calcareous nannofossil abundance in samples from Holes U1618A–U1618C show a high range of variability between rare and common. Species diversity is generally low, and the state of preservation varies between moderate and good. The nannofossil assemblages in samples from Site U1618 comprise nine groups/taxa, including *E. huxleyi*, small *Gephyrocapsa*, *G. caribbeanica*, medium *Gephyrocapsa*, medium *Reticulofenestra*, *C. pelagicus*, *Calcidiscus leptoporus*, *Helicosphaera carteri*, and *Syracosphaera* spp. Reworked nannofossils from older stratigraphic levels (mostly Cretaceous) are regularly present in samples, with an overall content that ranges between rare and frequent.

Table T4. Age and depth of biostratigraphic and paleomagnetic datums used for developing age-depth model of Site U1618. LO = lowest occurrence, HO = highest occurrence, LDO = lowest dominant occurrence. **Download table in CSV format.**

Biostratigraphic event	Event type	Age (Ma)	Event depth CSF-A (m)			Reference for age estimate
			Hole U1618A	Hole U1618B	Hole U1618C	
LO *E. huxleyi*	NANNO	≤0.13/0.29	4.88	17.83	17.5	Thierstein et al. (1977), Razmjooei et al. (2023)
Acme *G. caribbeanica*	NANNO	0.19–0.52	55.1			Razmjooei et al. (2023)
Brunhes/Matuyama boundary	PMAG	0.733	90.92			Gradstein et al. (2020)
Acme *P. stellatum*	DINO	~1.0	107.98	108.2		Matthiessen and Brenner (1996)
LDO small *Gephyrocapsa*	NANNO	1.24	96.05	96.1	94.55	Lourens et al. (2004)
P. cf. *curvirostris*	DIATOM	0.3–1.53	130			Koç and Scherer (1996)
HO *F. filifera*	DINO	1.0–1.4	159.88			Matthiessen et al. (2018)
HO *G. obliquus*	FORAM	0.3–1.7	176.3			Lam et al. (2022)
LO medium *Gephyrocapsa*	NANNO	1.73	197.65	200.25	231.36	Sato et al. (1991)
HO *H. tectata*	DINO	~2.0		303.09		Matthiessen et al. (2018)
Barren – *C. pelagicus* shifts	NANNO	1.7–2.8	199.3–275.91	242.5–266.23	242.84–267.38	Sato and Kameo (1996)
Matuyama/Gauss boundary	PMAG	2.595	342.45			Cande and Kent (1995)
"Pliocene flora"	DINO	2.7–3.0		395.85		S. De Schepper, unpubl. data, 2024

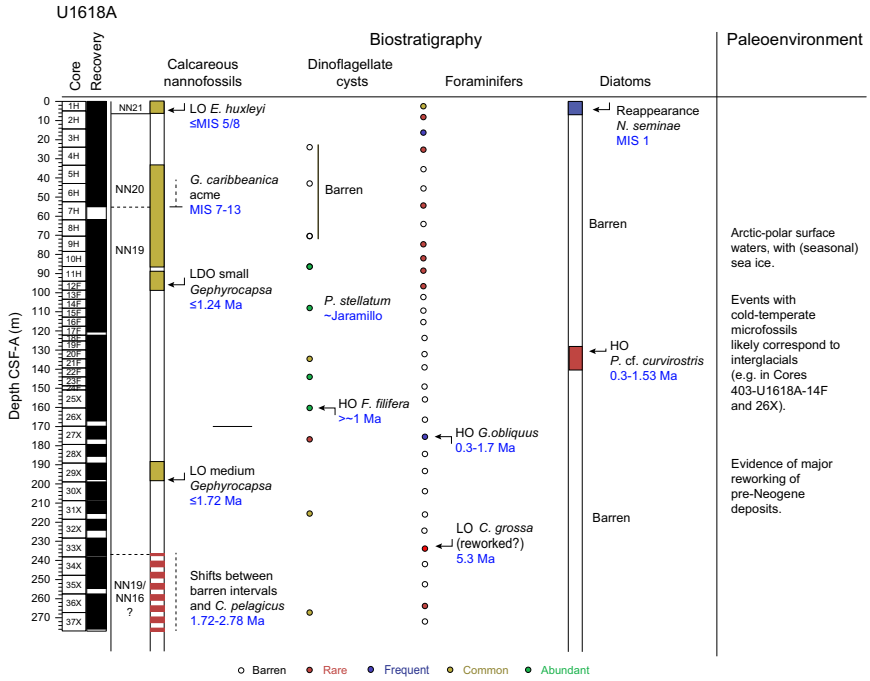

Figure F16. Biostratigraphy and paleoenvironment, Hole U1618A.

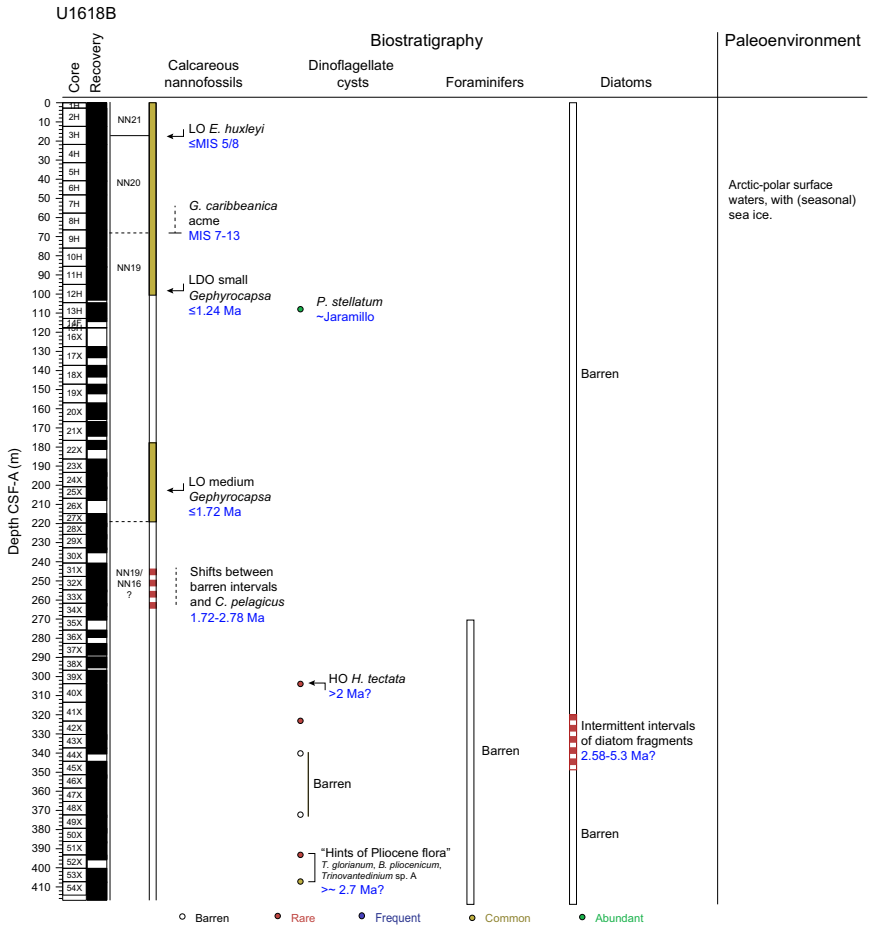

Figure F17. Biostratigraphy and paleoenvironment, Hole U1618B.

A total of three calibrated calcareous nannofossil events were identified across the three holes at Site U1618, allowing the site to be assigned an age range following the global zonation by Martini (1971). A good correspondence between the events in the three holes and nearby ODP Site 911 (Leg 151) is also observed, together with other regional and global records. Adaptation of calibrations for the North Atlantic, Fram Strait, and/or Arctic basin zonations are included when available. All this information assigns an accurate age range for Site U1618.

The LO of *E. huxleyi* is an indicator of Zone NN21 of Martini (1971), with a global calibration for equatorial to subpolar settings of 291 ka at MIS 8 (Thierstein et al., 1977; Rio et al., 1990; Raffi et al., 2006). In the central Arctic Ocean, the LO of *E. huxleyi* has been detailed to be time transgressive (i.e., diachronous), with a LO placed around MIS 5 (see Razmjooei et al., 2023, and references therein). At Site U1618, the LO of *E. huxleyi* is identified for the three holes in Samples 403-U1618A-1H-CC, 403-U1618B-3H-4, 114 cm, and 403-U1618C-3H-2, 140 cm. Combined, this suggests a lower age boundary that could span between MISs 8 and 5 and the assignment to the uppermost part of the Site U1618 sequence to Zone NN21 (Martini, 1971) (Figure **F14**).

For Hole U1618A, samples between Samples 6H-3, 54 cm, and 7H-CC are characterized by a common content of *G. caribbeanica*. Among these samples, the representation of this taxa is abundant and nearly monospecific in Sample 7H-1, 50 cm. This structure in nannofossil assemblages could be identifiable with the so-called acme of *G. caribbeanica*, globally defined between MISs 13 and 7 (Flores et al., 2012) and recognizable from tropical to subpolar settings of the North Atlantic (Maiorano et al., 2015; González-Lanchas et al., 2023) and the Arctic Ocean (Razmjooei et al., 2023). For Hole U1618A, the absence of *Pseudoemiliania lacunosa* in Sample 7H-1, 50 cm, suggests an age younger than or equal to 430 ka (MIS 12), according to the global calibration for the LO of *P. lacunosa*, or younger than or equal to MIS 13, according to the revision of this bound-

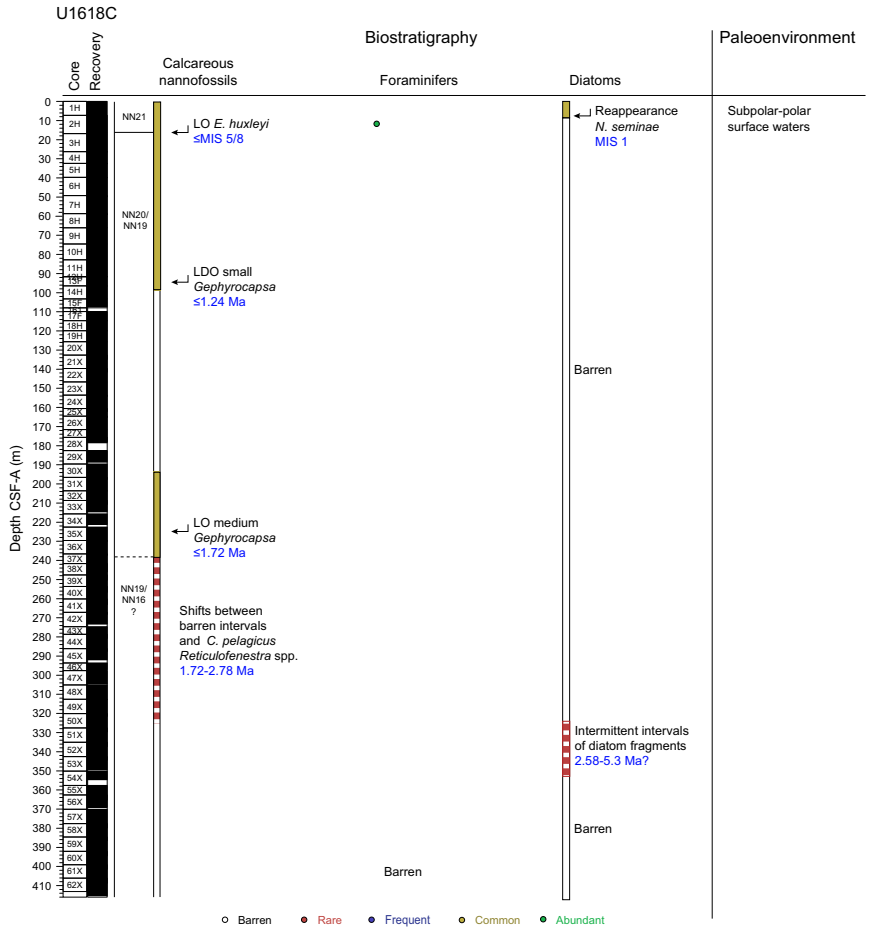

Figure F18. Biostratigraphy and paleoenvironment, Hole U1618C.

ary for Arctic environments (Razmjooei et al., 2023) (Figures **F14**, **F16**). The recognition of this acme event allows the assignment of this part of the Site U1618 sedimentary sequence to Zone NN20 of the Middle to Late Pleistocene (Figure **F14**).

The small *Gephyrocapsa* group is a characteristic dominant component of worldwide calcareous nannofossil assemblages since the Early Pleistocene. The LDO of this group has a calibrated age of 1.24 Ma (Lourens et al., 2004). In the sediments from Site U1618, the LDO of small *Gephyrocapsa* is consistently identified for the three holes in Samples 403-U1618A-12F-2, 60 cm, 403-U1618B-12H-1, 110 cm, and 403-U1618C-13F-3, 19 cm (Figures **F16**, **F17**, **F18**). In the absence of a regional calibration for this boundary in subpolar and Arctic environments, the standard calibration is adopted, placing the age of these sediments from the three holes as younger or equivalent to 1.24 Ma (Figure **F14**). The identification of this boundary characterizes this part of the sequence at Site U1618 in the Early Pleistocene, belonging to Zone NN19 (Martini, 1971).

The LO of the medium *Gephyrocapsa* group has a calibrated age of 1.71/1.73 Ma during the Early Pleistocene (Raffi, 2002; Raffi et al., 2006; Sato et al., 1991; Sato et al., 1999). Adopting the practice for nearby ODP Leg 151, the calibration of 1.72 Ma is considered (Sato and Kameo, 1996). The LO of medium *Gephyrocapsa* at Site U1618 is observed in Samples 403-U1618A-29X-CC, 403-U1618B-24X-5, 127 cm, and 403-U1618C-36X-2, 33 cm; hence, this Site U1618 sequence is assigned to Zone NN19 in the Early Pleistocene (Figures **F16**, **F17**, **F18**).

Calcareous nannofossils are scarce in samples below the LO of medium *Gephyrocapsa* and to the bottom of each hole at Site U1618. This interval is mainly barren, but toward the lower part of the sequence, intermittent levels with *C. pelagicus* occur in sediments from the three holes (Figure **F14**). A similar distribution of *C. pelagicus* was observed at ODP Site 911 (Leg 151) between 1.72 and 2.78 Ma (Sato and Kameo, 1996). The 2.78 Ma boundary determines the transition to Zone NN16 (Martini, 1971) and is globally defined by the LO of *Discoaster tamalis* in low- to mid-latitude records (Curry et al., 1995; Lourens et al., 2004). Because of environmental limitation on this variety in the high latitudes, the 2.78 Ma boundary is established as correspondent to the increase in representation of *Reticulofenestra* specimens over *C. pelagicus* in the Late Pliocene sediments at ODP Site 911 (Sato and Kameo, 1996). A rare occurrence of medium *Reticulofenestra* in Sample 403-U1618C-50X-3, 71 cm, could be considered as a hint of the proximity of this Pliocene boundary (i.e., 2.78 Ma) in the lowermost part of the sequence at Site U1618 (Figures **F14**, **F18**). This observation allows the potential assignment of this lower part of the sequence (i.e., from the LO of medium *Gephyrocapsa* to the bottom) to comprise the Early Pleistocene to Pliocene transition, ranging between Zones NN19 and NN16 (Martini, 1971).

4.2. Diatoms and silicoflagellates

The diatom investigation at Site U1618 included the examination of core catcher samples and additional samples from split core sections. Most of the samples are barren of diatoms, except Samples 403-U1618A-1H-1, 0 cm, and 403-U1618C-1H-1, 0 cm, in which a well-preserved diatom assemblage is found (Figures **F16**, **F18**). The most abundant taxa are *Chaetoceros* in resting spore stage, *Fragilariopsis oceanica* (Cleve) Hasle, *Thalassionema nitzschioides* var. *nitzschioides* (Grunow) Van Heurck, *Rhizosolenia borealis* (Sundström), and *Neodenticula seminae* (Simonsen and Kanaya) Akiba and Yanagisawa.

The species *N. seminae* accounts for more than 40% of the diatom assemblage in the subarctic North Pacific and its high-latitude marginal seas in the modern assemblage (Reid et al., 2007). In the high-latitude North Atlantic and in the Nordic Seas, the species occurred from the Middle Pleistocene (1.26 Ma) to the Early mid-Pleistocene transition at 0.84 Ma (Koç and Scherer, 1996). Its disappearance has been related with a severe cooling and the closure of the Arctic connection between the Atlantic and Pacific Oceans (Reid et al., 2007). Nevertheless, several studies indicated that *N. seminae* reenters the North Atlantic via the Arctic. It has been documented in plankton samples (Reid et al., 2007), surface sediment samples (Miettinen et al., 2013), and Holocene sediments of the Fram Strait (Matul and Kazarina, 2020).

Across all three holes at Site U1618, some intervals contain fragments of diatoms, but these were not useful for biostratigraphy. For Hole U1618A, an interval with diatom fragments and sponge

spicules is observed from 129.93 to 130.27 mbsf (Samples 19F-CC, 28 cm, 20F-1, 3 cm, and 20F-1, 10 cm). For Hole U1618B, another interval is found from 329 to 339.37 mbsf (Samples 42X-4, 130 cm, to 44X-2, 61 cm) (Figure **F17**). For Hole U1618C, the interval appears from 342.24 to 350.29 mbsf (Samples 52X-6, 69 cm, to 54X-1, 19 cm). Only in Sample 403-U1618A-20F-1, 3 cm, is a fragment of *P.* cf. *curvirostris* (Jousé) found, indicating a Pleistocene age (*P. curvirostris* Biozone) (Koç and Scherer, 1996). The most significant and identifiable diatom fragment is of *Paralia sulcata* (Ehrenberg) Cleve, which indicates transport from coastal shallow waters into the hemipelagic realm.

No silicoflagellates are observed.

4.3. Dinoflagellate cysts

Dinocysts were analyzed in a total of 18 samples from Holes U1618A–U1618C, and they are dominated by round brown cysts (RBCs) and *Brigantedinium*. *Bitectatodinium tepikiense* and *Islandinium* species are frequently recorded. Assemblages are well preserved, showing no influence of oxidation, and are low in diversity. Key stratigraphic species are present in low abundance.

Samples 403-U1618A-3H-CC, 5H-CC, and 8H-CC are dominated by reworked terrestrial and marine palynomorphs, and only a few in situ dinocysts are found. The in situ assemblage is represented by a few specimens of RBCs, *Brigantedinium simplex*, *Islandinium*, and *B. tepikiense*. The same species are more abundantly present in Sample 10H-CC (Figure **F16**).

Samples 403-U1618A-14F-CC and 403-U1618B-13H-4, 4–5 cm, contain a diverse assemblage (>10 species). Species encountered include *Brigantedinium*, RBCs, *Spiniferites*, *B. tepikiense*, *Protoceratium reticulatum* (indicative of Atlantic water), and cysts of *P. stellatum*. Such a diverse assemblage with abundant *P. reticulatum* is indicative of interglacial conditions (e.g., Matthiessen et al., 2018). The species *P. stellatum* is reported by Matthiessen and Brenner (1996) from around the Jaramillo Subchron at nearby ODP Site 911 on the Yermak Plateau (Sample 911A-11H-4, 72–78 cm). *F. filifera* is recorded in several samples from Hole U1618A (25X-CC, 31X-CC, 36X-CC, and 41X-CC). The HO of *F. filifera* is not a well-defined stratigraphic event. In the North Atlantic and Nordic Seas in the upper Matuyama Chron, its HO is between 1 and 1.4 Ma, but well-preserved specimens also occur in the Bruhnes Chron (Matthiessen et al., 2018). The range top of *F. filifera* in Sample 25X-CC would conservatively suggest an age older than ~1 Ma for deposits below this level but possibly older than 1.3–1.4 Ma. The better constrained top of the *F. filifera* acme (Matthiessen et al., 2018), which corresponds to the top of the Olduvai Subchron, is not identified in Hole U1618A. Only two specimens of *H. tectata* are recorded: one each in Samples 403-U1618B-39X-CC and 41X-CC (Figure **F17**). It is very tentative to base a stratigraphic interpretation on so few specimens, but if the record in Sample 39X-CC corresponds to the range top of the species, then this likely indicates an age older than 2 Ma for deposits below Sample 39X-CC. Near the base of Hole U1618B, traces of Late Pliocene flora are found. In Sample 51X-CC, *T. variabile* and *Trinovantedinium* sp. A are encountered (Figure **F17**). The latter species is thus far only found in the Late Pliocene (~2.7 Ma) of the Integrated Ocean Drilling Program Bering Sea Site U1341 (S. De Schepper, unpubl. data, 2024). In Sample 53X-CC, several specimens of *Trinovantedinium glorianum* and *T. variabile* and parts of the cyst *B. pliocenicum* are found. *B. pliocenicum* was reported from ODP Site 987 to have its HO just below Seismic Reflector R6 (Smelror, 1999). It ranges up into the Early Pleistocene (Head, 1993) but is mainly found in the Pliocene of the North Atlantic and Nordic Seas (De Schepper and Head, 2009; De Schepper et al., 2017).

Almost all investigated samples contain a substantial amount of reworked pollen and spores, degraded plant debris, and also pre-Neogene dinocysts. This reflects the considerable input of pre-Neogene sediments to the site. The in situ dinocyst assemblage is therefore sometimes hard to identify, and several samples are (nearly) barren. Where dinocysts are present, assemblages are mainly low in diversity and dominated by heterotrophic taxa (RBC and *Brigantedinium*). *Islandinium* is present in nearly all samples, and together with *Brigantedinium* it would suggest Arctic–polar water masses with sea ice for most of the studied interval. Exceptions are Samples 403-U1618A-14-CC and 403-U1618B-13H-4, 4–5 cm, which were taken in an interglacial during

or near the Jaramillo Subchron (Figure **F14**). Here, the dinocyst assemblage is diverse and indicates (cold–)temperate conditions as indicated by the presence of heterotrophic species, abundant *P. reticulatum*, *B. tepikiense*, and the acritarch *Nannobarbophora walldalei*. *P. reticulatum* is a good indicator for cold–temperate conditions and Atlantic water in the Fram Strait region (e.g., Matthiessen and Knies, 2001). *B. tepikiense* is a subpolar–temperate species, which today occurs mostly at mid-latitudes of the North Atlantic (de Vernal et al., 2020), and the acritarch *N. walldalei* is linked with warm–temperate conditions and interglacials (Head, 2003).

4.4. Foraminifers

A total of 54 samples from Holes U1618A–U1618C were analyzed for planktonic foraminifers. Planktonic foraminifers are very sparse in Hole U1618A. They are generally present in the uppermost ~99 m (Cores 1H–12H), with abundances from rare to common (Figure **F16**). They show a moderate to high degree of dissolution or encrustation. Generally, only *Neogloboquadrina pachyderma* is present, except in Sample 403-U1618A-12H-CC where *Globigerinoides bulloides* also appear. *N. pachyderma* is the dominant planktonic foraminiferal species in polar regions (e.g., Bé and Tolderlund, 1971). It is found today in the Fram Strait within Arctic and polar water masses in areas both with and without seasonal sea ice (e.g., Husum and Hald, 2012; Pados and Spielhagen, 2014). Below this level, samples are barren of planktonic foraminifers, except Sample 27X-CC. This sample holds a well-preserved diverse fauna consisting of *G. bulloides*, *Globigerinoides conglobatus*, *G. obliquus*, *Globigerinoides ruber*, *Globorotalita woodi*, *Neogloboquadrina incompta*, *Orbulina universa*, and *Trilobatus sacculifer*. These species first appear in the Oligocene and Miocene, and most are extant. Some of the species (e.g., *G. ruber*) were also observed at ODP Sites 910 and 911 at the nearby Yermak Plateau in upper Pliocene sediments (Spiegler, 1996). *G. obliquus* and *G. woodi* have their last appearances in the Early Pleistocene, but recent work by Lam et al. (2022) demonstrated diachronous datums of these species in the Pacific. Their last appearance is at 293 and 427 ka, respectively, in the Northwest Pacific (Lam et al., 2022). Hence, we speculate that the last appearance of these species is also diachronous in the Atlantic but within the Middle Pleistocene (Figure **F14**). Furthermore, the observed species within Sample 27X-CC are characteristic of temperate–subtropical environments (e.g., Lam et al., 2022) (Figure **F16**).

During analysis, we also noted whether benthic foraminifers are present. Overall, only potential biostratigraphic marker species were identified to species level, and further taxonomic analysis of benthic foraminifers will be carried out postexpedition. Sample 403-U1618A-27X-CC contains the benthic foraminifer *C. grossa* (Figure **F14**). Sample 32X-CC also contains rare specimens of *C. grossa*, which may suggest a Pliocene age (e.g., Feyling-Hanssen et al., 1983; King, 1983); however, the HO of *C. grossa* is diachronous, and this event is younger (Pleistocene) than previously defined (Anthonissen, 2008). Other investigations have also reported a Late–Middle Miocene age for the first appearance of *C. grossa* (Voorthuysen, 1950; Eidvin and Rundberg, 2001).

For Hole U1618B, Samples 35X-CC to 54X-CC were analyzed for planktonic foraminifers. All samples are barren (Figure **F17**).

One sample from Hole U1618C at 18.17 mbsf that was assumed to be MIS 5 was analyzed (Figure **F18**). Planktonic foraminifers are very abundant, with very abundant *N. pachyderma* and rare abundance of *N. incompta* and *G. bulloides*. This is a typical subpolar–polar planktonic foraminiferal fauna (e.g., Schiebel and Hemleben, 2017). This targeted sample was also analyzed for benthic foraminiferal fauna. Benthic foraminifers are common, mainly consisting of *Islandiella helenae* and *Epistominella exigua*. *Melonis barleeanus* and *Stainforthia fusiformis* also occur to some degree (rare abundance). Single specimens of both *Cassidulina reniforme* and *Cassidulina neoteretis* in addition to *Triloculina tricarinata* are also observed. All these species may be found together in high-latitude environments (e.g., Sejrup et al., 2004). Additionally, the composition of this benthic foraminiferal fauna is similar to what has previously been reported from MIS 5 in a sediment core from 500 m water depth at the southern Yermak Plateau (Chauhan et al., 2014), thus tentatively supporting the assumed age (MIS 5). Additionally, the three deepest core catcher samples from Hole U1618C (60X-CC to 62X-CC) were analyzed because they go below the range of Hole U1618B. They are all barren (Figure **F14**).

5. Paleomagnetism

Paleomagnetic investigation of Site U1618 focused on measurements of the natural remanent magnetization (NRM) before and after alternating field (AF) demagnetization of archive-half sections and vertically oriented discrete cube samples. All archive-half sections were measured except a few that had significant visible coring disturbance. Some archive-half sections with high MS (greater than ~750 IU) were too strong for the NRM to be measured on the superconducting rock magnetometer (SRM) and caused flux jumps even when the track speed was slowed by 10×, thus compromising our ability to collect quality data in these intervals. However, the intensity often was reduced after AF demagnetization, and measurements could then be made. APC and HLAPC archive-half sections were measured before and after 10 and 15 mT peak AF demagnetization. Because XCB cores do not use nonmagnetic core barrels and are more susceptible to the viscous isothermal remanent magnetization (VIRM) drill string overprint (Richter et al., 2007), XCB archive-half sections required higher AF demagnetization steps to remove this overprint and were measured before and after 15 and 30 mT peak AF demagnetization. The NRMs of the oriented discrete cube samples were stepwise demagnetized to higher fields up to either 50 mT if analyzed on the SRM using the in-line AF demagnetizing system or 100 mT if analyzed on the AGICO JR6 spinner magnetometer using the DTECH D-2000 static AF demagnetizer. These measurements were supplemented by measurements of MS and anhysteretic remanent magnetization (ARM) on samples from all holes. Isothermal remanent magnetizations (IRMs) at various direct current fields (100, 300, and 1000 mT and a backfield of –300 mT) were imparted and measured on Hole U1618A samples. Two unoriented iron sulfide nodules were also sampled and subject to MS, ARM, and IRM analyses.

5.1. Sediment magnetic properties

Site U1618 sediments have a wide range of magnetic properties that likely reflect contribution from detrital and authigenic sources. Although sediments are mostly lithogenic in origin (see **Lithostratigraphy**) and magnetic characterization of samples from the uppermost two cores is consistent with (titano)magnetite, authigenic iron sulfides are visible on the split core surface, sometimes occurring as nodules up to a few centimeters in diameter and sometimes associated with the highest observed MS at Site U1618 (up to ~3000 IU measured on the Whole-Round Multisensor Logger [WRMSL]). MS values greater than 500 IU become common below about 190 mbsf (Figures **F25**, **F26**), and these intervals are often associated with high-density objects in X-ray images and black to gray nodules on the split core surface. One of these nodules (from Core 403-U1618B-25X; 201.64 mbsf) with strong MS and a ~2–3 cm diameter was subsampled and studied for its magnetic properties and mineralogy (Figure **F19**; Table **T5**). Bulk XRD analysis found the nodule to mostly be composed of greigite (92%; Fe_3S_4) and associated with iron monosulfide (<1%; FeS) and siderite (7.5%; $FeCO_3$) (Figure **F19E**). Future work could explore the mineral associations of these iron sulfide nodules to determine formation pathways. Greigite association with siderite has previously been described, and further information on the timing of formation might help determine the age of the greigite-hosted chemical remanent magnetization (CRM) relative to the age of the sediment (Roberts and Weaver, 2005). Magnetic measurements confirmed the strong magnetization of this nodule, with MS, ARM, and IRM intensities almost two orders of magnitude stronger than any other discrete cube sediment sample measured from Site U1618. The nodule has no frequency dependence of MS and an S-ratio (IRM after a 300 mT backfield normalized by a saturating IRM at 1000 mT) (Stober and Thompson, 1979) of 1, indicating that the mineral's remanence fully saturates in a 300 mT field, consistent with previously reported magnetic properties for sedimentary greigite (Roberts et al., 2011; Horng, 2018). Despite having an S-ratio of 1, the nodule has higher coercivity than might be expected for typical detrital (titano)-magnetite assemblages, with 58% of its remanence gained during IRM acquisition between 100 and 300 mT (Table **T5**). The nodule is also quite resistant to AF demagnetization, with 91% of its ARM remaining after a 30 mT peak AF demagnetization (Figure **F19D**). A second iron sulfide nodule was sampled from Core 403-U1618B-30X and subject to the same measurements. This sample was found to be weakly magnetic relative to the oriented sediment cube samples from Site U1618 but had a high frequency dependence of MS (~7%), indicating the presence of superparamagnetic material (Table **T5**). XRD results from this nodule found the composition

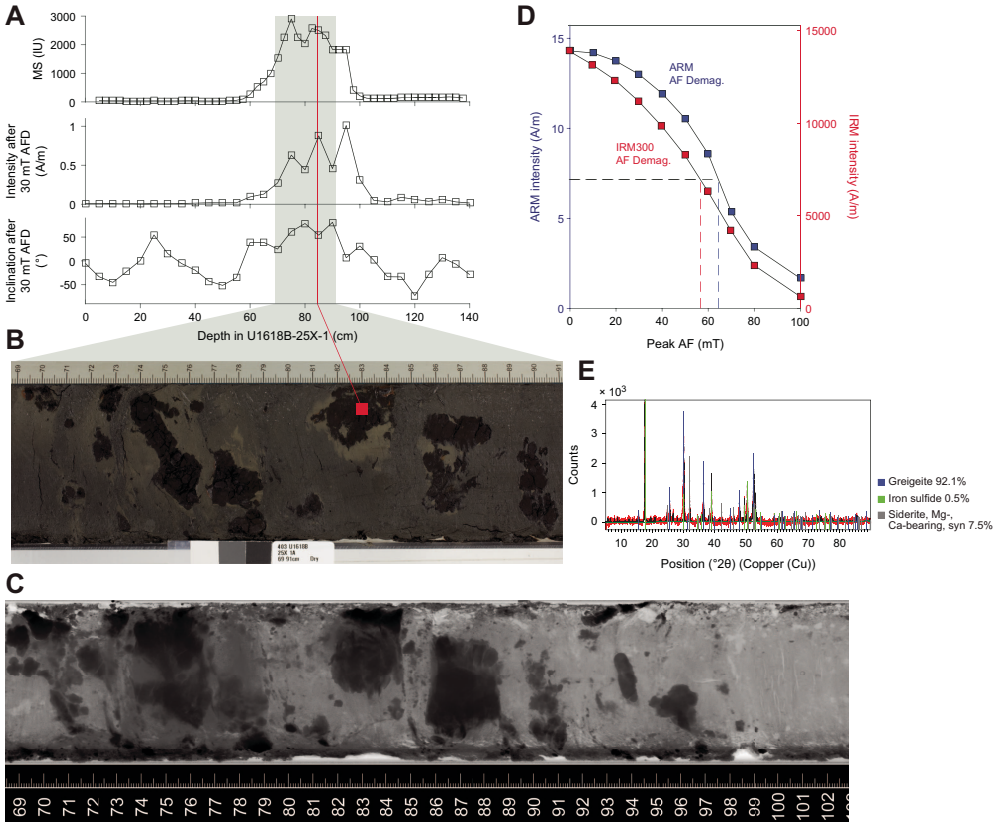

Figure F19. Interval containing several centimeter-scale greigite nodules (403-U1618B-25X-1). A. MS, NRM intensity after 30 mT peak AF demagnetization, and inclination after 30 mT AF demagnetization. This interval has among the highest MS values measured at Site U1618, and the inclination indicates the possibility for both reverse and normal magnetized sediments in this section. B, C. Photograph and X-ray image of the nodules. D. AF demagnetization of an ARM and 300 mT IRM (IRM300) imparted to the sample (Table T5). E. Bulk XRD results of the nodule confirming the sample is mostly greigite and associated with siderite.

Table T5. Summary of mineralogy and magnetic properties from two iron sulfide nodules sampled at Site U1618. The sample from Core 403-U1618B-25X has very strong magnetic properties, whereas the sample from Core 403-U1618C-30X has a weak magnetization compared to other Site U1618 sediments. **Download table in CSV format.**

Core:	403-U1618B-25X	403-U1618-C-30X
Mineralogy (XRD result):	Greigite: 92.1%	Pyrite: 65.7%
	Iron sulfide: 0.5%	Quartz: 17.5%
	Siderite: 7.5%	Marcasite: 16.8%
Concentration-dependent parameters (assuming 0.5 cm^3 volume):		
k (SI)	9.04E–02	1.36E–04
k_{FD} (%)	0.00	7.26
ARM (A/m)	1.43E+01	4.89E–02
IRM100 (A/m)	5.77E+03	4.00E+00
IRM300 (A/m)	1.39E+04	7.77E+00
IRM1000 (A/m)	1.41E+04	8.02E+00
IRM–300 (A/m)	1.42E+04	7.75E+00
Concentration-independent parameters:		
ARM/k	158.2	360.1
ARM_{30mT}/ARM	0.91	0.65
ARM_{MDF} (mT)	64.4	50.8
IRM100/IRM300	0.42	0.52
$IRM300_{30mT}$/IRM300	0.81	0.80
$IRM300_{MDF}$ (mT)	56.8	56.3
S ratio	1.01	0.97
SIRM/k	1.56E+05	5.91E+04
ARM/IRM300	1.03E–03	6.30E–03
IRM300/ARM	9.72E+02	1.59E+02

was 65.7% pyrite, 17.5% quartz, and 16.8% marcasite, which is consistent with there being only trace amounts of material with ferrimagnetic properties present in this sample.

The magnetic properties of 127 oriented sediment cube samples were used to provide insight to the magnetic mineralogy that hosts the NRM. The coarse resolution of the samples (~1 sample per 5 m) is too low to capture downcore trends; however, the variability of the samples likely reflects the range of magnetic minerals present in Site U1618 sediments (Figure **F20**). ARM coercivity, tracked by the ratio of the ARM after 30 mT peak AF demagnetization to the initial ARM (ARM_{30mT}/ARM), has a wide range of values (0.30–0.94) and a bimodal distribution with modes centered on 0.52 and 0.67. Previous work has demonstrated that both greigite and magnetite can have wide ranges of ARM coercivities, but greigite values are typically much greater (Peters and Thompson, 1998). These previous observations, along with our direct characterization of a Site U1618 greigite nodule (ARM_{30mT}/ARM = 0.91) and samples from the uppermost 20 m in Hole U1618A, which are above the depths where interstitial water (IW) sulfate is depleted (average ARM_{30mT}/ARM = 0.43; n = 4) (Figure **F42**), suggest that this wide range of ARM coercivities most likely reflects varying contribution of greigite (high ARM_{30mT}/ARM) and detrital magnetic minerals (lower ARM_{30mT}/ARM). This parameter shows a clear mixing relationship between the magnetic mineralogy typical of the uppermost samples (likely [titano]magnetite) and the greigite nodule when comparing multiple rock magnetic parameters like the IRM coercivity (tracked by the 300 mT IRM after 30 mT peak AF demagnetization over the initial IRM at 300 mT;

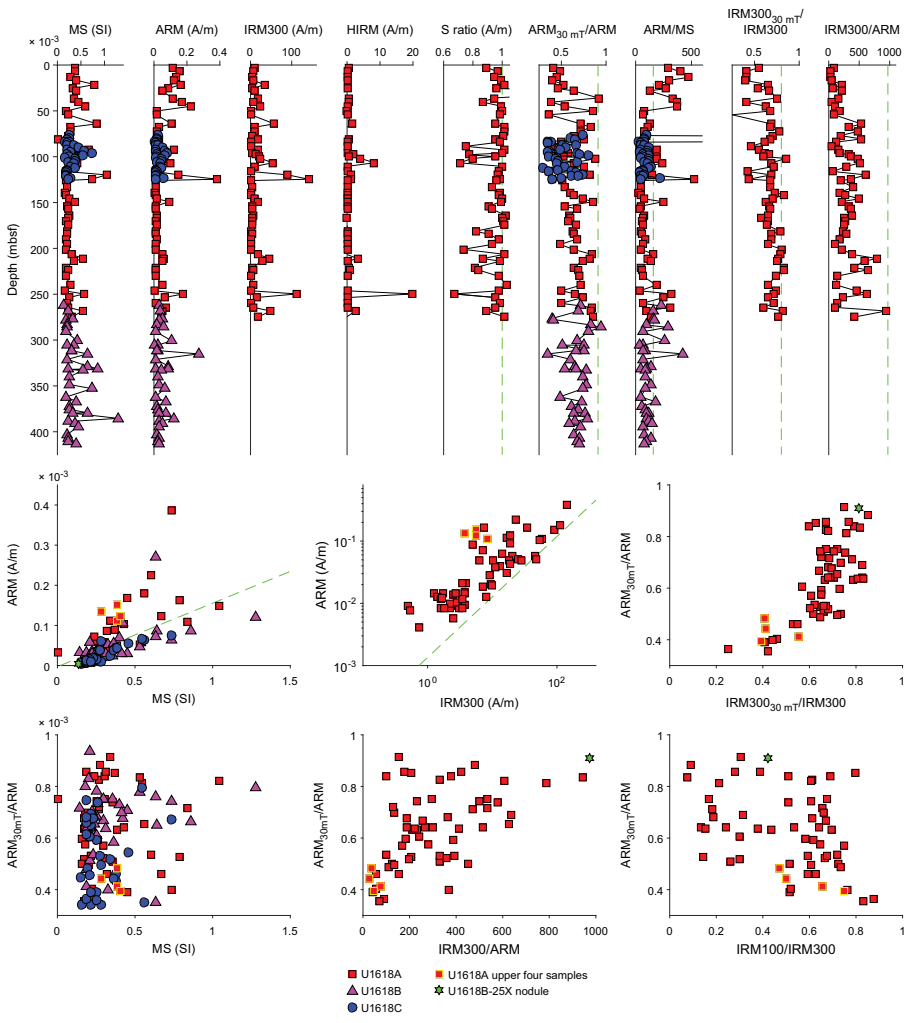

Figure F20. Rock magnetic data collected on sediments, Site U1618. Green stars/dashed lines = greigite nodule. IRM100 = IRM acquired after 100 mT. IRM300 = IRM acquired after 300 mT. HIRM = hard IRM. 30mT (subscript) = measurement after 30 mT peak AF demagnetization.

$IRM300_{30mT}$/IRM300) and the IRM300/ARM ratio (Figure **F20**). Downhole variations indicate that greigite concentration is variable and there are many samples with magnetic signatures such as low ARM coercivity that are likely dominated by detrital sources. These samples may be more suitable paleomagnetic recorders. Additional magnetic minerals beyond greigite and (titano)magnetite are present in varying concentrations, as indicated by S-ratio values that range 0.67–1 (50% of values are greater than 0.97; 90% of values are greater than 0.80). These variations in the S-ratio indicate the presence of magnetic minerals whose IRM saturates above 300 mT, such as hematite or pyrrhotite. Future rock magnetic work can identify the magnetic minerals present at Site U1618 and their implications for interpreting the paleomagnetic record.

5.2. Natural remanent magnetization

Of NRM intensities at Site U1618, 95% were between 1.1×10^{-3} and 3.8×10^{-1} A/m, with APC/HLAPC sections between 4.0×10^{-4} and 5.9×10^{-2} A/m after 15 mT peak AF demagnetization and XCB sections between 5.0×10^{-4} and 2.0×10^{-1} A/m after 30 mT peak AF demagnetization. Following the 15 mT AF demagnetization step, the distributions of measured inclinations from APC/HLAPC cores have a strong peak slightly less than the expected normal geocentric axial dipole (GAD) prediction for the latitude of Site U1618 (84.4°) in all three holes, reflecting that the majority of APC/HLAPC cored intervals were likely deposited during Chron C1n (Brunhes) (Figure **F21**). The inclination distributions for XCB-cored intervals after the 30 mT AF demagnetization step are much less pronounced and do not show distributions expected from a geomagnetic field that approximates a GAD on average. This is likely due in part to the differences between coring methods. The APC/HLAPC method is able to recover less disturbed core with less VIRM drill string overprint but also likely reflects some complications in the NRMs themselves, as described below.

The uppermost ~90 m at each site have directions that are consistent with normal polarity at this latitude (steep and positive inclinations), outside of some cored intervals that experienced coring deformation or other disturbance. Between 90 and 91 mbsf in each hole, we observe the first reverse directions and note that these first reverse directions correlate to similar MS features (Figure **F22**). However, below this horizon we observe frequent changes between inclinations consistent with reverse and normal polarity occurring on the scale of <1 to around ~7 m. In the

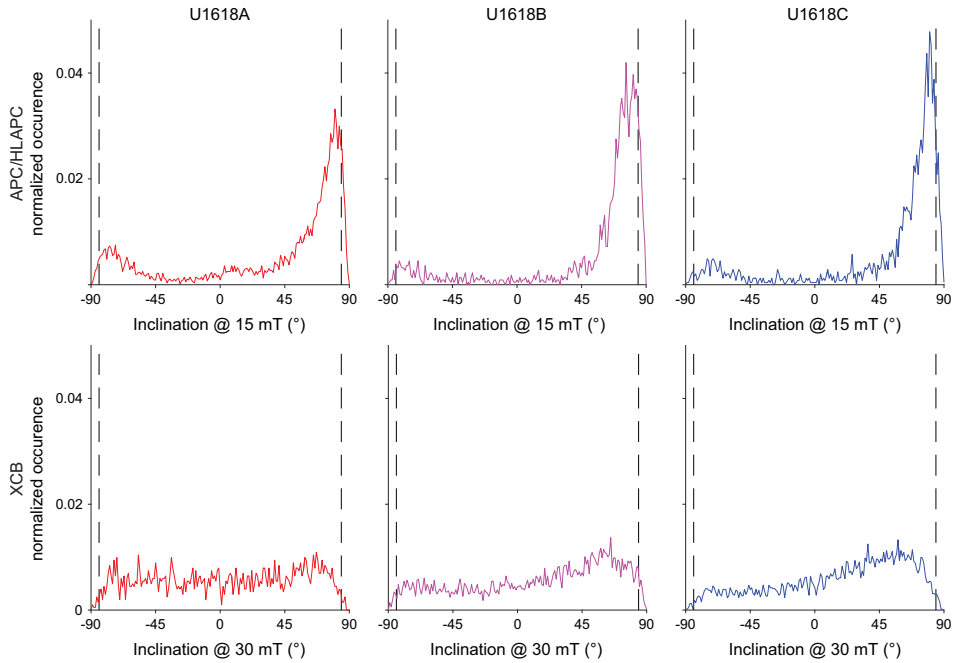

Figure F21. Inclinations measured on archive-half sections, Site U1618. Dashed lines = predicted values for a GAD at this latitude (see Table T5 in the Expedition 403 methods chapter [Lucchi et al., 2026]).

context of biostratigraphy observations at Site U1618 (see **Biostratigraphy and paleoenvironment**), this pattern contains many more magnetic reversals and polarity zones than the normal 80 ky long Subchron C1r.1n (Jaramillo) or 35 ky long Subchron C1r.2n (Cobb Mountain) expected in the 2020 geologic timescale (GTS2020; Gradstein et al., 2020) or the handful of brief geomagnetic excursions documented in late Chron C1r (Matuyama) (Channell et al., 2020). Thus, the (1) unequivocal evidence for the presence of authigenic greigite at Site U1618 (discussed above), (2) well-defined thick normal polarity zone in the uppermost 90 m, and (3) frequent reversals between normal and reverse GAD consistent directions below the first reverse direction (~90 m) suggest that many intervals in the Site U1618 stratigraphy are potentially remagnetized by a late-forming CRM. These data are consistent with deep (>10s m) formation of authigenic greigite, which would acquire a CRM that is younger than the detrital remanent magnetization of the surrounding sediment. For example, layers of sediment deposited in the reverse Chron C1r.1r (latest Matuyama) may host a CRM acquired during the normal Chron C1n (Brunhes).

To further explore the NRMs of Site U1618 sediment, we examined the AF demagnetization behavior of the discrete cube samples. Orthogonal projection plots show a variety of behaviors, ranging from higher quality samples in which a characteristic remanent magnetization (ChRM) can be defined to samples for which no ChRM can be determined (Figure **F23**). Some samples gained intensity at higher demagnetization steps, which may be explained as a gyroremanent magnetization or as a result of a nonzero field near the AF coils. Samples with high ARM coercivity that likely contain abundant greigite were often characterized by strong and stable NRMs with well-defined ChRMs. It was difficult to recognize the VIRM drill string overprint in samples with normal magnetizations because the drill string VIRM manifests as a steep and positive inclination, like the ambient normal magnetic field. In samples with reverse magnetization, the effect of the drill string overprint was apparent, with XCB cores often requiring a peak AF of 30 mT or more to fully remove the VIRM. Polarity could be determined for all but eight samples, and ChRMs could typically be defined using a range of AF steps between 15 and 60 mT that varied from sample to sample. The quality of the ChRM could be assessed with the maximum angular deviation parameter (Kirschvink, 1980) and could be used to filter magnetizations that were poorly defined, noisy, VIRM overprinted, or had complex AF demagnetization behavior. The remanence carrier could be inferred from the ARM_{30mT}/ARM ratio to assess whether the magnetization was hosted by greigite. This approach assumes that higher ARM coercivity ratios (up to ~0.90) are dominated by

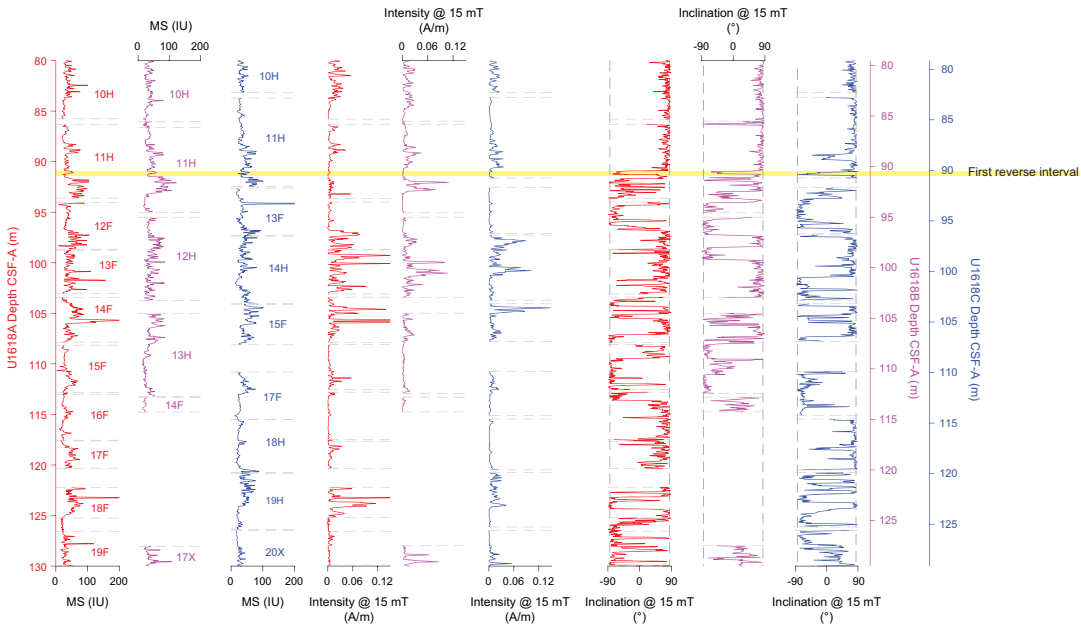

Figure F22. Archive-half paleomagnetic measurements around and below the onset of what is interpreted to be Chron C1n (Brunhes), Site U1618. MS was measured on the WRMSL. NRM intensity and inclination were taken after 15 mT peak AF demagnetization.

authigenic greigite like the greigite nodule we studied, whereas lower ratios (as low as ~0.4) are dominated by detrital minerals like the samples from the uppermost ~20 m. Although there is much to learn about the formation timing and pathways of greigite at Site U1618, samples dominated by greigite have the potential to host a later forming CRM that may be younger than the age of the surrounding sediment.

5.3. Magnetic stratigraphy

As previously discussed, determination of polarity zones was complicated by the potential for CRMs hosted by the authigenic mineral greigite. However, we can still confidently identify three major polarity zones that we interpret to reflect Chrons C1n (Brunhes; 0–773 ka), C1r–C2r (Matuyama; 773–2595 ka), and C2An (Gauss; 2595–3596 ka) (Figure **F24**; Table **T6**). Our interpretation of the normal polarity zone at the base of Holes U1618B and U1618C as Chron C2An (Gauss) was informed through conversation with the shipboard micropaleontologists and not derived entirely independently. However, this normal polarity zone indicates that the base of recovered sediments at Site U1618 are Late Pliocene in age (younger than 3.6 Ma).

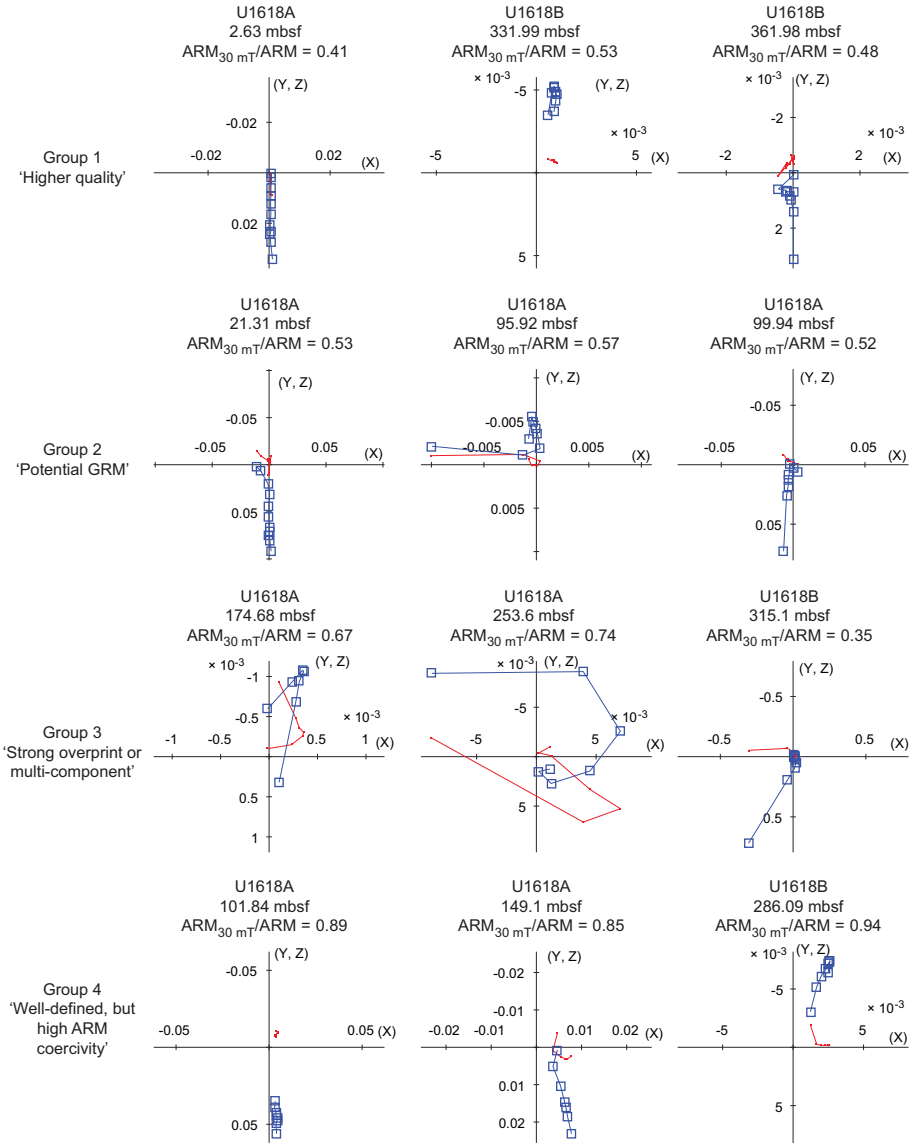

Figure F23. Representative AF demagnetization behavior of discrete cube samples, Holes U1618A and U1618B. Blue squares are in the vertical (*X*, *Z*) plane; red line is in the horizontal (*X*, *Y*) plane.

The onset of Chron C1n (Matuyama/Brunhes boundary; 773 ka) was determined as the downcore transition to the first reverse polarity interval that could be traced to a correlative MS feature in all three holes (Figure **F22**). This depth was within 1 m on each hole's CSF-A depth scale: 90.915 mbsf in Hole U1618A, 90.45 mbsf in Hole U1618B, and 90.21 mbsf in Hole U1618C (depths are the midpoint of the transition; the full depth range is reported in Table **T6**). It is still uncertain if this transition is recorded by a primary detrital remanent magnetization and reflects the actual reversal at 773 ka in MIS 19. However, at a minimum, it must reflect a maximum limiting depth of the reversal because it would be unlikely to have a reverse remagnetization during normal Chron C1n (Brunhes). Detailed work on discrete cube samples, considering only samples that we assume to have a lower influence of greigite with ARM_{30mT}/ARM ratios less than 0.65, supports this placement of the onset of Chron C1n (Brunhes). Cube samples bracket the transition in Hole U1618A

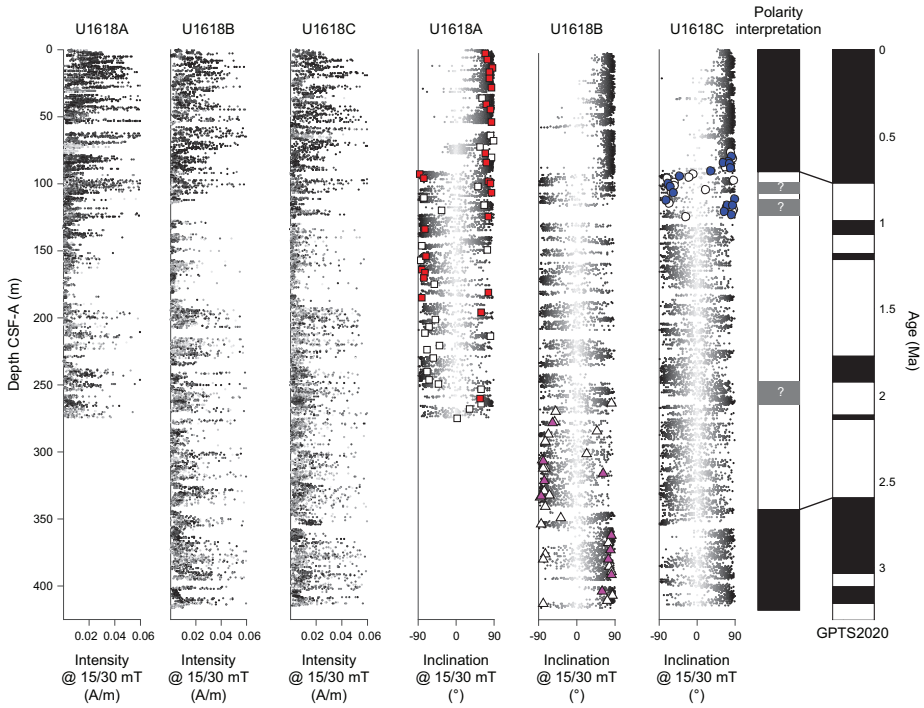

Figure F24. Archive-half and discrete sample paleomagnetic measurements, Site U1618. Archive-half NRM intensity and inclination are plotted after 15 mT peak AF demagnetization for APC/HLAPC cores and 30 mT peak AF demagnetization for XCB cores. Shading is proportional to the difference from predicted inclinations based on a GAD. Cube samples are plotted as symbols and are the ChRM determined through PCA analysis. Colored symbols = more reliable data with ARM_{30mT}/ARM values < 0.65 and maximum angular deviation values < 20°. Polarity interpretation focused on defining the major polarity zones and can be correlated to the major polarity zones of the geomagnetic polarity timescale (GPTS). Black = normal, white = reverse, gray = intervals that may represent shorter polarity zones but require further investigation.

Table T6. Summary of magnetostratigraphic constraints interpreted for Site U1618. o = onset, t = termination. NR = not recovered. **Download table in CSV format.**

		Hole U1618A			Hole U1618B			Hole U1618C			
Chron	Age (Ma)	Top depth CSF-A (m)	Bottom depth CSF-A (m)	Midpoint depth CSF-A (m)	Top depth CSF-A (m)	Bottom depth CSF-A (m)	Midpoint depth CSF-A (m)	Top depth CSF-A (m)	Bottom depth CSF-A (m)	Midpoint depth CSF-A (m)	Notes
C1n (o)	0.773	90.88	90.95	90.915	90.4	90.5	90.45	90.11	90.31	90.21	C1n onset defined by first downcore transition to reverse polarity in all three holes that is associated with a correlative magnetic susceptibility feature; we do not observe stable reverse polarity that would be associated with C1r.1r.
C2An (t)	2.595		NR		340.1	344.8	342.45	333.1	357.6	345.35	C2An termination depths defined using archive-half data; however, perhaps the most reliable data are from Hole U1618B associated with a reverse discrete sample at 332 m and normal discrete sample at 362 m (midpoint = 347 m) that have well-defined magnetizations and ARM coercivities consistent with magnetite.

at 84.1 mbsf (normal) and 92.69 mbsf (reverse) and in Hole U1618C at 87.65 mbsf (normal) and 94.08 mbsf (reverse) (Figure **F24**).

The top of Chron C2An (Gauss/Matuyama boundary; 2595 ka) is best defined in Hole U1618B where archive-half measurements can be directly compared to cube samples. Cube samples with ARM_{30mT}/ARM ratios less than 0.65 define a transition between 332 mbsf (reverse) and 362 mbsf (normal), with several well-defined and lower ARM_{30mT}/ARM with normal directions between 362 and 403.5 mbsf (Figure **F24**). Using archive-half data, we interpret that this range could be narrowed to between 340.1 mbsf (reverse) and 344.8 mbsf (normal) with a midpoint at 342.45 mbsf; however, this could likely be confirmed and refined in postcruise research (Table **T6**). It is possible that Subchrons C2An.1r (Kaena) and/or C2An.2r (Mammoth) are recorded in brief intervals with reverse archive-half directions in Holes U1618B and U1618C, including clusters around 352 mbsf (Holes U1618B and U1618C) and 384 and 397 mbsf (Hole U1618C). However, all cube samples with reverse magnetization below 362 mbsf in Hole U1618B have ARM_{30mT}/ARM values between 0.68 and 0.76 and likely contain significant amounts of greigite (Figure **F24**).

There is great potential to further refine the magnetic stratigraphy at Site U1618 with higher resolution and detailed paleomagnetic investigation that characterizes the NRM and magnetic mineral assemblages. Although greigite-hosted CRMs that postdate the primary detrital remanent magnetizations are present, initial rock magnetic characterization indicates that samples through the entire recovered interval contain a wide range of magnetic properties, with many samples having properties consistent with limited influence from greigite. Future work can better characterize how easy-to-measure magnetic parameters, such as ARM_{30mT}/ARM, correlate to the exact mineralogy with additional thermal, in-field magnetization, scanning electron microscope/energy dispersive spectrometry, and mineralogical studies. This may be helpful to better define depths of the Chron C1n (Matuyama/Brunhes boundary) onset and Chron C2An (Gauss/Matuyama boundary) termination and identify shorter polarity intervals, such as Subchrons C1r.1n (Jaramillo), C1r.2n (Cobb Mountain), C2n (Olduvai), C2An.1r (Kaena), and C2An.2r (Mammoth). Of note, clusters of normal directions defined by cube samples with lower ARM_{30mT}/ARM ratios between 97.87 and 106.6 mbsf in Hole U1618A and 115.6 and 123.2 mbsf in Hole U1618C may be good candidates for Subchrons C1r.1n (Jaramillo) and/or C1r.2n (Cobb Mountain) (Figure **F24**). However, there is not good agreement between the two holes, and this interval deserves closer attention and a more rigorous assessment of the magnetic minerals present. Similarly, a broad cluster of normal directions between around 246 and 266 mbsf in all three holes with a well defined normal direction in a cube sample from 259.9 mbsf in Hole U1618A may be a good candidate for Subchron C2n (Olduvai) and also deserves closer attention (Figure **F24**).

6. Physical properties

The physical properties measured shipboard for Site U1618 included nondestructive whole-round measurements using the Special Task Multisensor Logger (STMSL), WRMSL, and Natural Gamma Radiation Logger (NGRL), as well as thermal conductivity and discrete *P*-wave velocity measurements on working-half sections after cores were split. GRA bulk density and MS were measured on the STMSL immediately after recovery and then on the WRMSL after thermally equilibrating for a minimum of 4 h. Cores 403-U1618C-1H through 3H and 62X were excluded from GRA bulk density measurements due to their selection for sedimentary ancient DNA (sedaDNA) sampling and the need to avoid exposure to the radioactive cesium source. Physical property data from the STMSL were used for initial hole-to-hole stratigraphic correlation and splicing (see **Stratigraphic correlation**) to aid in near-real-time drilling and sampling decisions (e.g., sedaDNA sampling), but they are not further evaluated and reported here. Further use of STMSL data is discouraged because WRMSL and Section Half Multisensor Logger (SHMSL) data, collected after allowing for thermal equilibration, are available in the Laboratory Information Management System (LIMS) database. Aside from three 10 cm intervals that were sampled for anelastic strain recovery (ASR) analysis, *P*-wave velocity was measured on the WRMSL for all core sections. Results from whole-round scans are compiled in Figure **F25**. Discrete *P*-wave measurements were made on at least one section per core for the uppermost cores from Holes U1618A and U1618C using the Section Half Measurement Gantry (SHMG). However, below ~50 mbsf, SHMG

measurements ceased due to poor data quality in deeper sediments, likely related to higher gas content and coarser material. Thermal conductivity measurements were made for all cores from Hole U1618A and deeper cores from Holes U1618B and U1618C using a puck probe on the split face of working-half sections. Whole-round physical property data were used for the final hole-to-hole stratigraphic correlation and splicing (see **Stratigraphic correlation**).

Working-half sections of all cores from Hole U1618A and deeper cores from Holes U1618B and U1618C were sampled for moisture and density (MAD) analyses. Representative lithostratigraphic units with minimal coring disturbances were targeted. Archive halves were measured with the SHMSL for point MS (MSP) and color reflectance and X-ray scanned using the X-Ray Linescan Logger (XSCAN) (see **Lithostratigraphy**). Three 10 cm interval whole-round samples from Holes U1618B and U1618C were taken for ASR analysis.

6.1. Magnetic susceptibility

MS was measured both on whole-round sections using a pass-through loop sensor on the WRMSL track and on split archive-half sections using a point-source sensor on the SHMSL track. Sections were measured at 2.5 cm increments on the WRMSL. The resolution for the SHMSL measurements was 2.5 cm and occasionally switched to 5 cm in the interest of time for Holes U1618B and U1618C. WRMSL and SHMSL MS measurements yielded similar values and down-

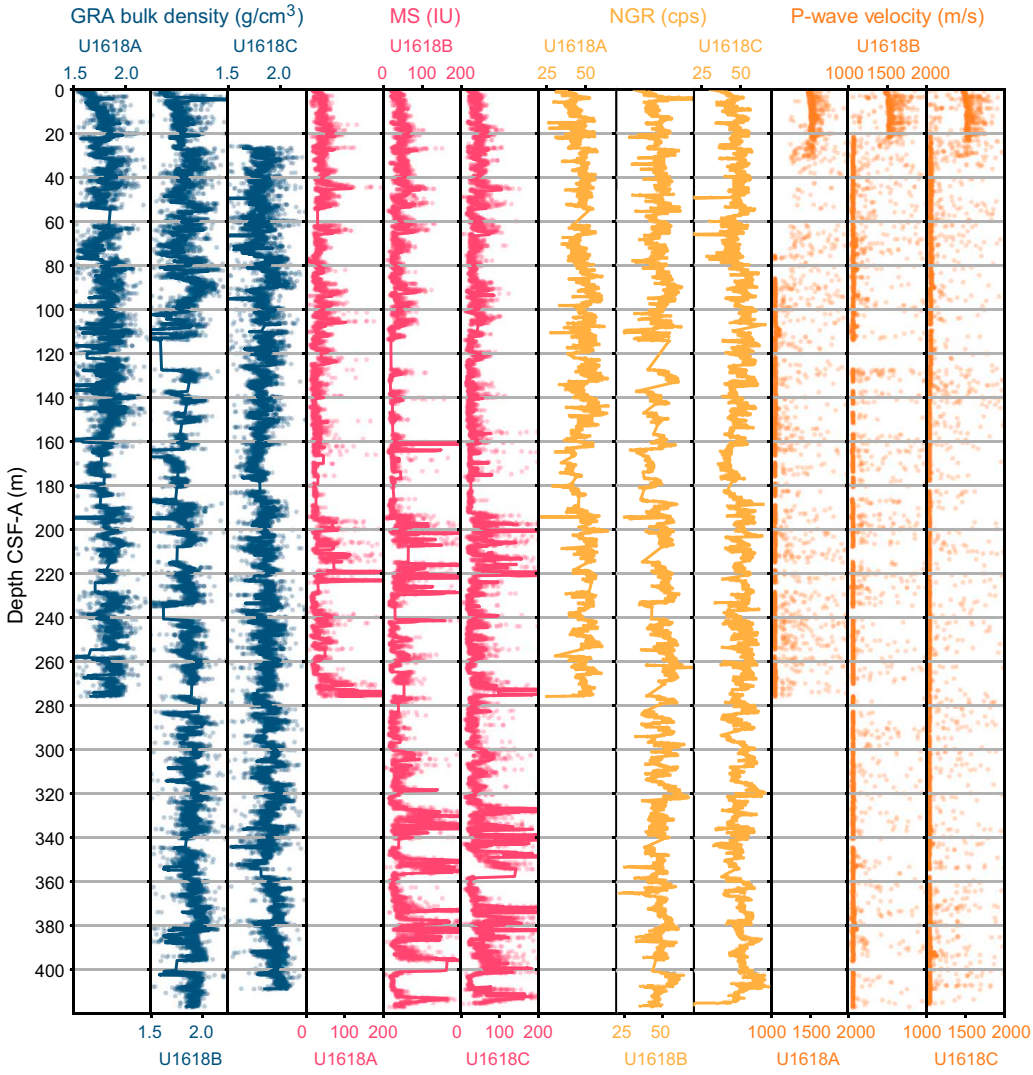

Figure F25. Physical properties, Site U1618. Lines = running averages. cps = counts per second.

hole variability (Figure **F26**). MS values range 0.7–4186 IU for measured whole-round sections and 0.1 to ~12,000 IU for point measurements on the archive-half section surfaces. Overall, the average MS value for both WRMSL and SHMSL data is ~47–50 IU across Holes U1618A–U1618C (see **Physical properties** in the Expedition 403 methods chapter [Lucchi et al., 2026] for details on instrument units).

From the seafloor to ~150 mbsf, MS values vary between ~2–5 and ~150 IU and MS co-varies with NGR and GRA bulk density. However, below ~150 mbsf, there is no obvious association of MS with other downcore physical properties. From ~150 mbsf to the base of the hole, irregularly spaced, large peaks in MS become prevalent, with maximum WRMSL-derived MS values between ~300 and ~5000 IU. These maxima are orders of magnitude higher than the background, which is represented by MS modes of 24.69, 24.49, and 24.27 IU for Holes U1618A, U1618B, and U1618C, respectively. MS peaks are often associated with the occurrence of authigenic iron sulfide minerals (e.g., greigite identified in rock magnetic and XRD analyses) (see **Lithostratigraphy**, **Geochemistry**, and **Paleomagnetism**). The large peaks in MS generally do not correspond to

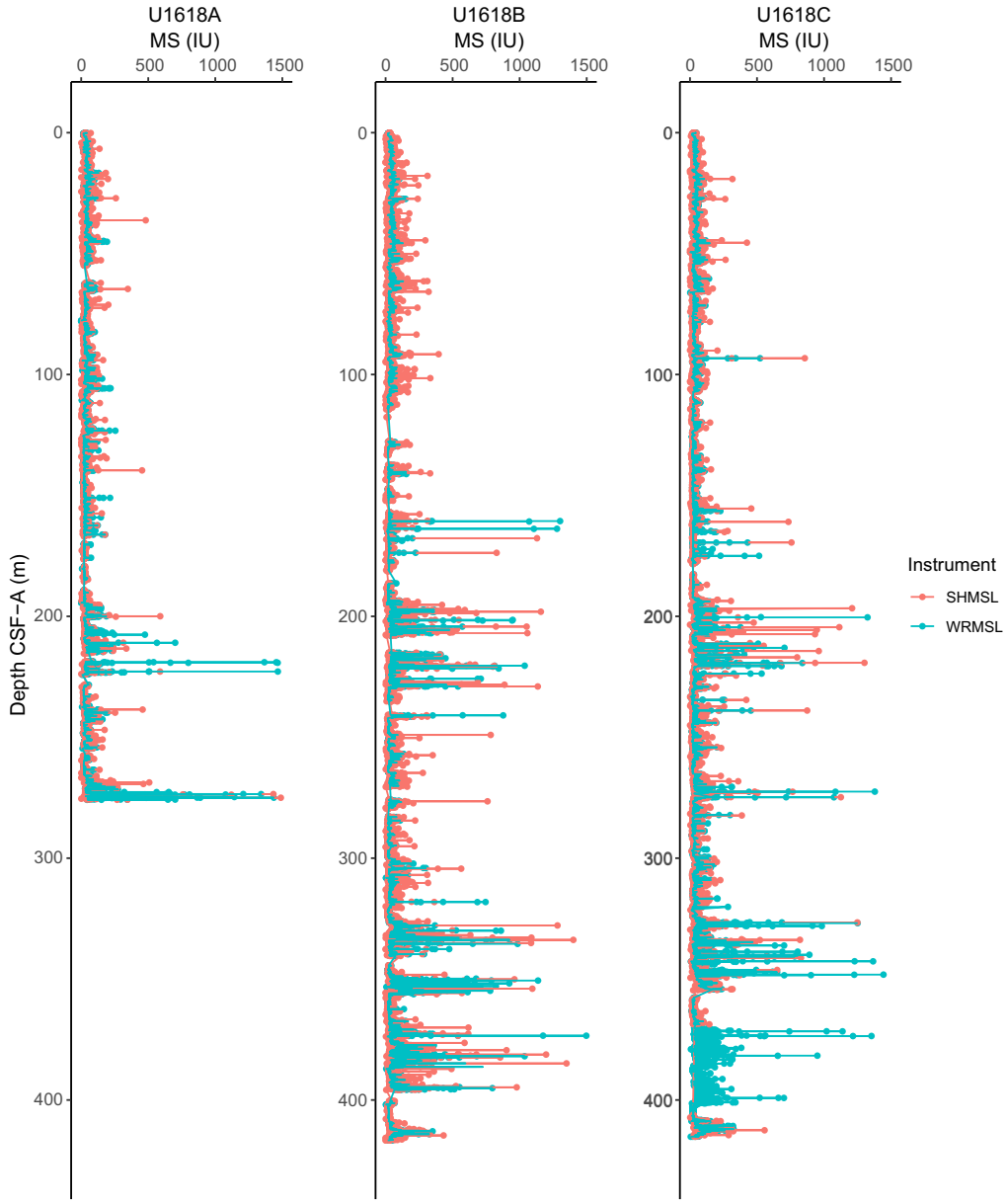

Figure F26. MS, Site U1618. Measurements were taken on whole rounds using a pass-through loop sensor (WRMSL) and on split archive-half sections using a point-source sensor (SHMSL).

peaks in NGR or GRA bulk density (Figure F27). The changes in physical properties observed at ~150 mbsf correlate to the boundary between Lithostratigraphic Units I and II (see **Lithostratigraphy**).

6.2. Gamma ray attenuation bulk density

Except for the cores that were sampled for sedaDNA, every whole-round section was measured at 2.5 cm intervals with the GRA densitometer on the WRMSL. Excluding outliers related to voids or coring disturbances, measured GRA bulk density values range ~1.6 to ~2.0 g/cm^3, with a strong mode at ~1.8–1.9 g/cm^3 and no correlation with MS (Figure F27). The GRA bulk density recorded downcore shows a rapid increase from the seafloor (~1.6 g/cm^3) to ~25 mbsf (1.8–1.9 g/cm^3) that is likely related to increased compaction with depth. Several large peaks in bulk density, reaching ~2.4 g/cm^3, occur in intervals ~25–150 and ~250–375 mbsf. These may be associated with clast-rich lithologies (e.g., diamicton). Observed bulk density lows at ~150–200 mbsf are associated with Unit II (see **Lithostratigraphy**). From ~170 mbsf to the base of the hole, GRA bulk density is less variable, which may be associated with the transition to XCB cores below ~120 mbsf.

6.3. Natural gamma radiation

NGR was measured on all whole-round core sections at 10 cm intervals. Measured NGR values range 18–74 counts/s (average = ~49 counts/s). From the seafloor to ~80 mbsf, NGR values average ~47 counts/s. From ~80 to 150 mbsf, NGR values increase to an average of ~50 counts/s and show more variability, ranging ~27–65 counts/s. An interval with a relatively low average NGR of ~45 counts/s and a tighter distribution of NGR values at ~150–190 mbsf corresponds to Lithostratigraphic Unit II (see **Lithostratigraphy**). From ~190 mbsf to the base of the hole, NGR values increase to an average of ~50.5 counts/s and demonstrate a more sawtooth variability. Generally, NGR mirrors GRA bulk density trends downcore, such as at 80–100, 160–180, and 300–350 mbsf, but correlations are less apparent below 360 mbsf (Figure F27).

6.4. *P*-wave velocity

Whole-round sections were measured for compressional *P*-wave velocity on the WRMSL at a resolution of 2.5 cm for all core sections from Site U1618. Values range from ~1350 m/s at the seafloor to ~1560 m/s at 25 mbsf. Below ~25 mbsf, the signal becomes dominated by noise with values out of the range expected for marine sediments, reaching outlier values of ~15,000 m/s and above. No downcore signal was detectable. We encountered persistent issues with void spaces and gas expansion, which we suspect contributed to anomalous values. The use of these data for interpretation is discouraged.

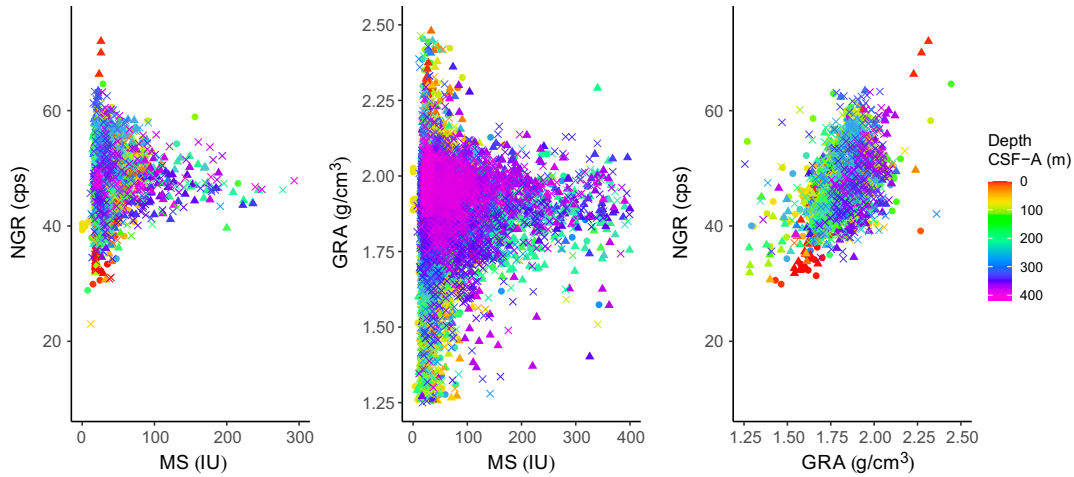

Figure F27. NGR, GRA bulk density, and MS, Site U1618. Circles = Hole U1618A, triangles = Hole U1618B, Xs = Hole U1618C. cps = counts per second.

Discrete *P*-wave velocity measurements were made using the SHMG (see **Physical properties** in the Expedition 403 methods chapter [Lucchi et al., 2026]) in intervals that excluded excessive coring disturbances, voids, cracks, or large clasts. One section per core was measured for Cores 403-U1618A-1H through 6H and 403-U1618C-1H through 9H using the *x*-caliper and *y*- and *z*-bayonets. Because of noise in the signal, *P*-wave velocity waveforms were manually selected. Values range from ~1500 m/s at the seafloor to ~1600 m/s at ~50 mbsf, generally increasing downcore, as expected with sediment compaction at depth. Below ~50 mbsf, however, *P*-wave measurements on the SHMG were abandoned due to increasing noise and eventual lack of a detectable signal. We suspect the abundance of large clasts and authigenic mineral formations (e.g., greigite nodules and authigenic carbonates), as well as free gas trapped in isolated pore spaces of the deeper, more consolidated sediments, contributes to signal depletion below ~50 mbsf.

6.5. Moisture and density

MAD analyses were conducted using 107 discrete samples collected from the working section halves of Cores 403-U1618A-1H through 37X, 403-U1618B-34X through 54X, and 403-U1618C-56X through 62X (see **Physical properties** in the Expedition 403 methods chapter [Lucchi et al., 2026]). Several parameters, including porosity, water content, and bulk density, were calculated using the wet mass, dry mass, and volume measurements of samples. MAD bulk density increases sharply from ~1.5 g/cm^3 at the sediment surface to ~2.0 g/cm^3 at ~50 m downcore, corresponding to sharply decreasing porosity and water content from 67% to 54% and 43% to 32%, respectively. This change in porosity and water content closely corresponds to the increase in sediment induration that is a defining characteristic of the Lithostratigraphic Subunit IA/IB boundary (see **Lithostratigraphy**). From 50 mbsf to the termination of Hole U1618B, MAD bulk density ranges ~1.7 to ~2 g/cm^3 (average = ~1.9 g/cm^3). There is greater variability in MAD bulk density to ~200 mbsf, below which depth values are generally stable around ~1.8 g/cm^3. Overall, MAD bulk density values correspond well to GRA bulk density trends downcore (Figure **F28**). The highest MAD bulk density values are found at ~140 mbsf (~2.1 g/cm^3) near the transition from Unit I to II (see **Lithostratigraphy**) and from APC/HLAPC to XCB recovery at ~285 mbsf (~2.1 g/cm^3) and between ~360 and 370 mbsf (~2.0 g/cm^3). Additional parameters calculated from MAD analyses include water content, porosity, and void ratio. These properties co-vary downcore, and water content, void ratio, and porosity are anticorrelated with MAD bulk density (Figure **F29**). After an initial sharp decrease from the seafloor to ~50 mbsf, water content generally ranges ~22%–27% downcore, and porosity ranges ~46%–51%.

6.6. Thermal conductivity

To calculate heat flow and interpolate temperature data, thermal conductivity measurements were made using the TK04 system for one working section half per core for Cores 403-U1618A-15H through 37X; 403-U1618B-34X through 54X; and 403-U1618C-1H-29X, 40X, 41X, and 56X–62X. A puck contact probe was placed on the split face of working section halves. To ensure good contact with the probe, a small amount of deionized water was added and/or the face was swept with a spatula. Homogeneous intervals lacking large clasts, voids, cracks, and sediment disturbances were targeted. Three measurements were made on the same interval, but we encountered a few failed measurements from the TK04 meter. Some cores did not have suitable intervals for thermal conductivity, especially XCB cores, which often had biscuiting, large clasts, and cracks on the surface of split core halves. Therefore, thermal conductivity results were not possible for all cores and may be responsible for some of the scatter in measurements downcore. Overall, thermal conductivity values at Site U1618 increase slightly with depth from ~1.1 W/(m·K) at the seafloor to ~1.3 W/(m·K) at ~415 mbsf, likely corresponding to a downcore increase in dry bulk density and a decrease in porosity from compaction (Figure **F30**). Results from thermal conductivity taken from split cores agree with the downhole temperature gradient (see **Downhole logging**).

6.7. Anelastic strain recovery

ASR experiments were conducted using three whole-round samples, each 10 cm long, selected from the top of Sections 403-U1618B-40X-4 and 54X-2 and the bottom of Section 403-U1618C-

6H-9. After STMSL and NGR scanning, the whole-round core liners were cut on the core receiving platform, and samples were removed from the core liners. To attach 16 strain gauges, soft materials (i.e., drilling mud) surrounding the core samples were removed and the surfaces were flattened with a spatula and/or sandpaper. Gauges were glued onto the surfaces, and the samples were wrapped with plastic bags and put into a thermostatic water bath. All strain gauges were then electrically connected to a data logger to collect 3D strain recovery. All sample preparation procedures were completed within 3.5–4.5 h after core recovery from the subseafloor. Average strain values of 11 ASR measurements were collected every 10 min from each of the 18 strain gauges. Temperatures and dummy channel data were also measured to ensure that the water temperature was stable and that the data logger was operating correctly. Gauges remained connected to the samples to monitor strain value for ~14 days to fully record the recovery. Preliminary results show that after temperature equilibrium, strain released logarithmically but that some strain gauges

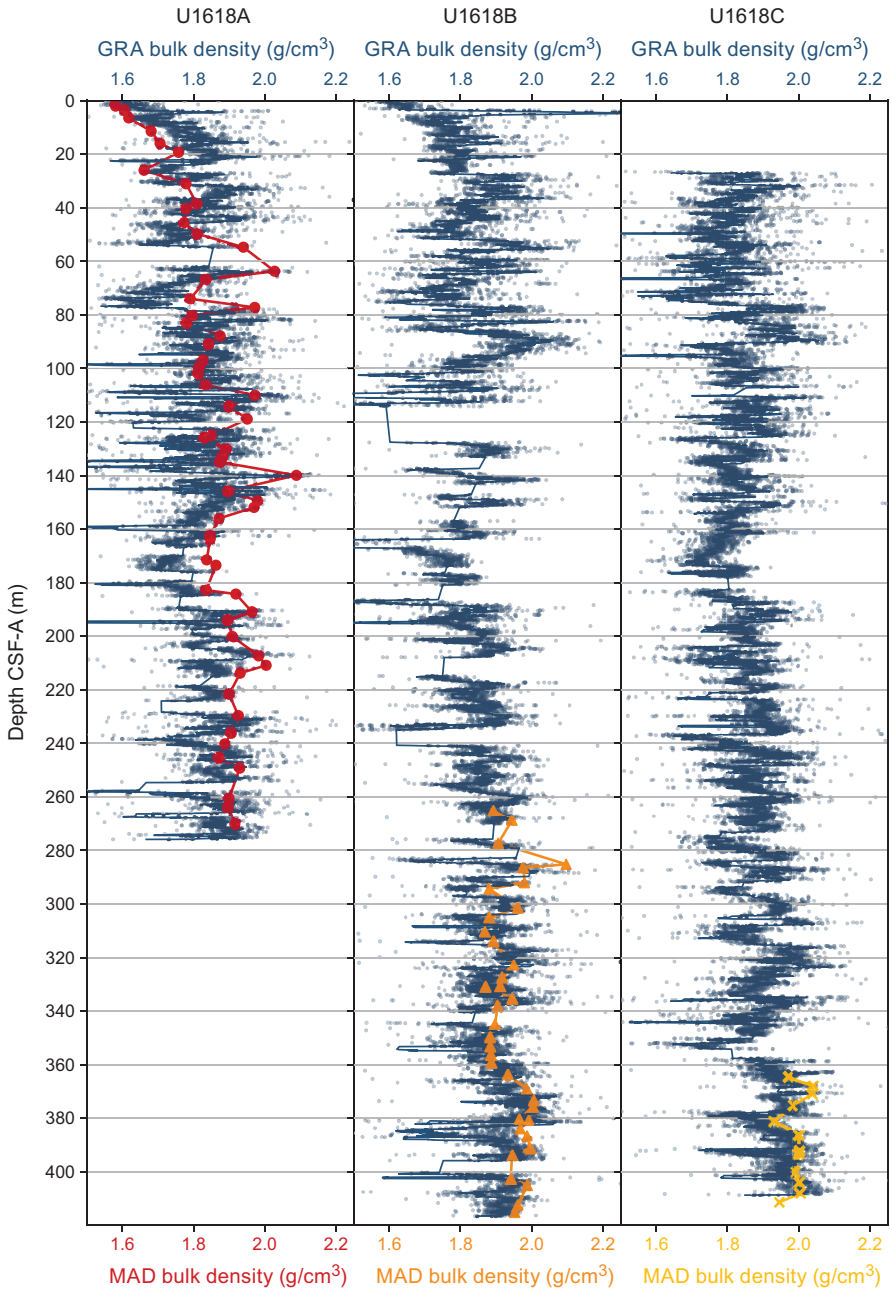

Figure F28. GRA bulk density and MAD, Site U1618. Measurements were made on the WRMSL (GRA) and discrete samples (MAD).

showed shrinking (Figures **F31**, **F32**, **F33**). Postexpedition, inversion analysis will be conducted to convert the raw strain data set to 3D strain that will be combined with azimuths of core samples by paleomagnetism to determine actual principal stress azimuths.

6.8. Physical properties summary

There is generally good correspondence between data collected at higher resolution on the MS loop sensor and data collected at lower resolution on the MSP sensor, with the MSP measurements picking up additional peaks in MS that were missed during the averaging in WRMSL measurements. There is also good correspondence between GRA bulk density and discrete MAD sample measurements. Because of issues with gas, as discussed above, *P*-wave velocity data are not considered reliable, and there is no detectable signal in discrete nor logger data below ~25–50 mbsf. Thermal conductivity data generally show a downcore increase, with a few outliers likely associated with measurements that did not have proper contact with the probe (see **Downhole logging**).

GRA bulk density and NGR show a positive linear correlation, consistent with NGR counts tracking fine-grained clay. All correlations are stronger in shallower cores less than ~150 m deep (Lithostratigraphic Unit I/II boundary). The NGR signal is a marker of lithologic change (Figure

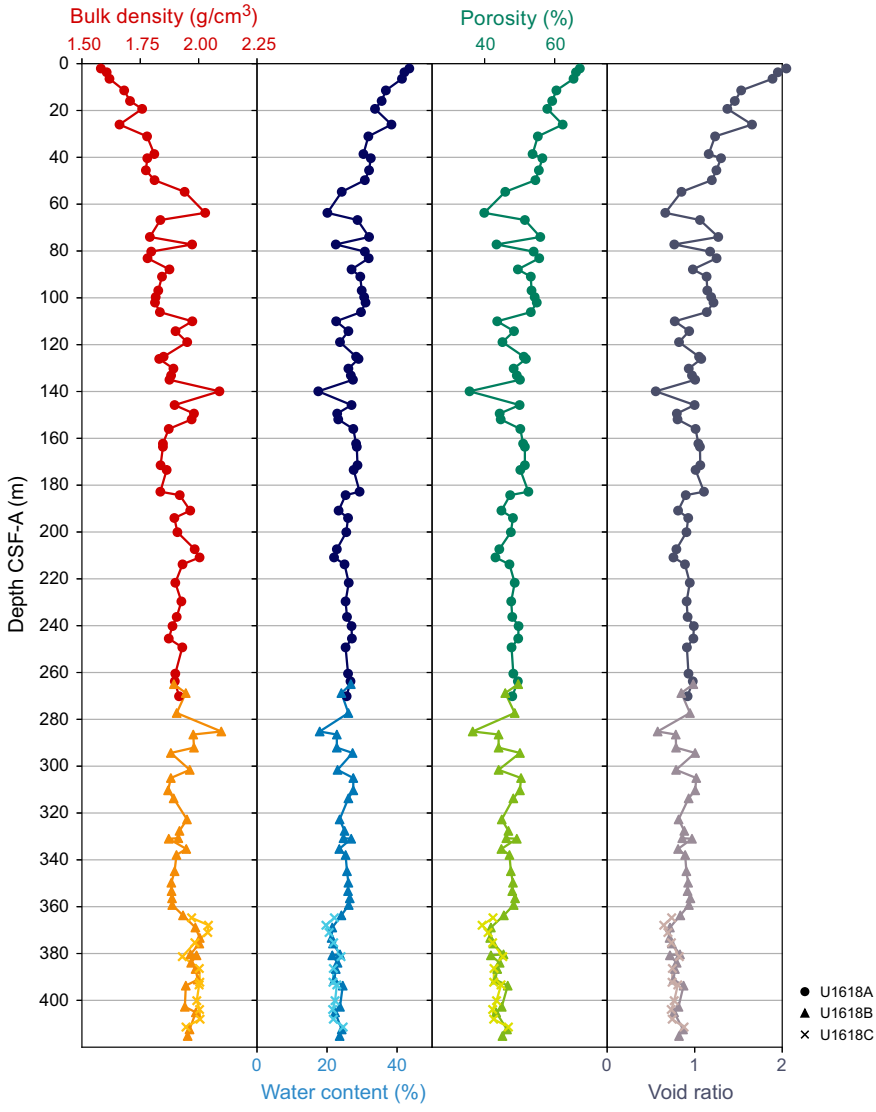

Figure F29. MAD parameters, Site U1618.

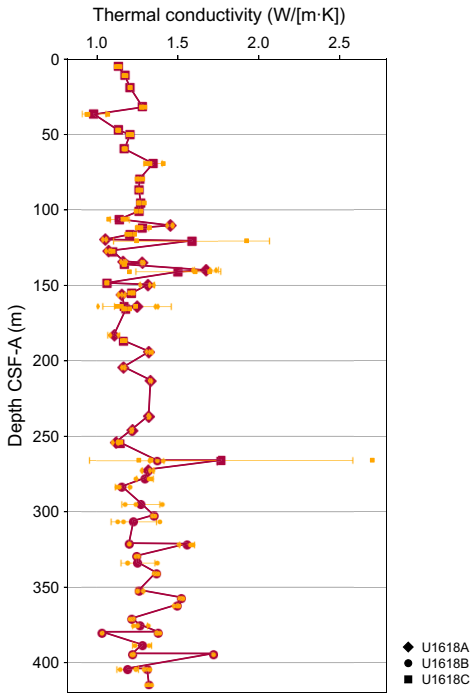

Figure F30. Thermal conductivity, Site U1618. Orange = individual measurements, orange lines = SD, maroon = averages.

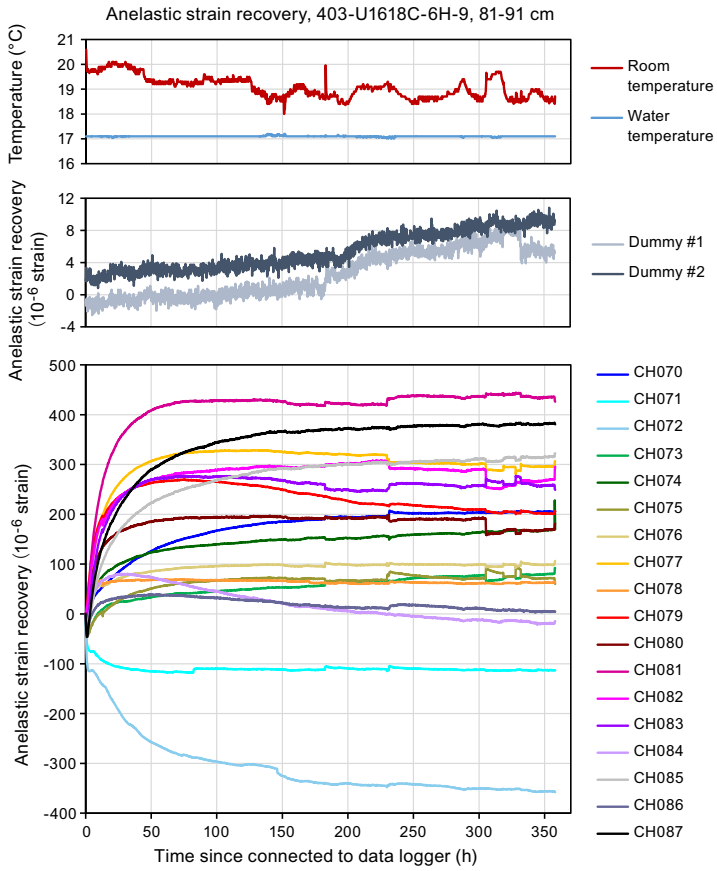

Figure F31. ASR initial results, Sample 403-U1618B-6H-9, 81–91 cm. Top: temperature monitoring data used to ensure water bath temperatures were stable. Middle: results from a dummy channel used to ensure that the data logger was operating correctly. Bottom: average values of the 11 ASR measurements collected from the 18 strain gauges every 10 min over ~14 days.

F34) with lowest counts in Unit II and higher counts in Subunit IIIA. NGR is important for identifying the relationship between physical properties and lithostratigraphy, especially because the MS signal was influenced by postdepositional alteration and GRA measurements were omitted in cores sampled for sedaDNA analyses.

A notable feature at Site U1618 is the prevalence of peaks with MS values that are orders of magnitude higher than the background. The outsized MS maxima below 150 mbsf are likely associated with authigenic iron sulfide nodules (see **Paleomagnetism**) and can indicate diagenetic alteration. GRA bulk density has a strong mode at ~1.8–1.9 g/cm^3, which does not co-vary with MS (Figure **F27**), indicating that magnetically strong constituents are not limited to a specific material or degree of compaction.

Overall, physical properties at Site U1618 appear to be influenced by glaciogenic deposition and postdepositional processes that complicate interpretations of depositional lithofacies. Glaciogenic deposition, including dense glacial diamicts and debris flows, is consistent with the location of the eastern Vestnesa Ridge close to the Kongsfjorden Trough Mouth Fan on the western margin of Svalbard, and postdepositional processes are consistent with findings of authigenic concretions in an active methane hydrate seepage area. Further studies onshore are necessary to interpret the relationship between physical properties measured on board, depositional lithofacies, and postdepositional alteration.

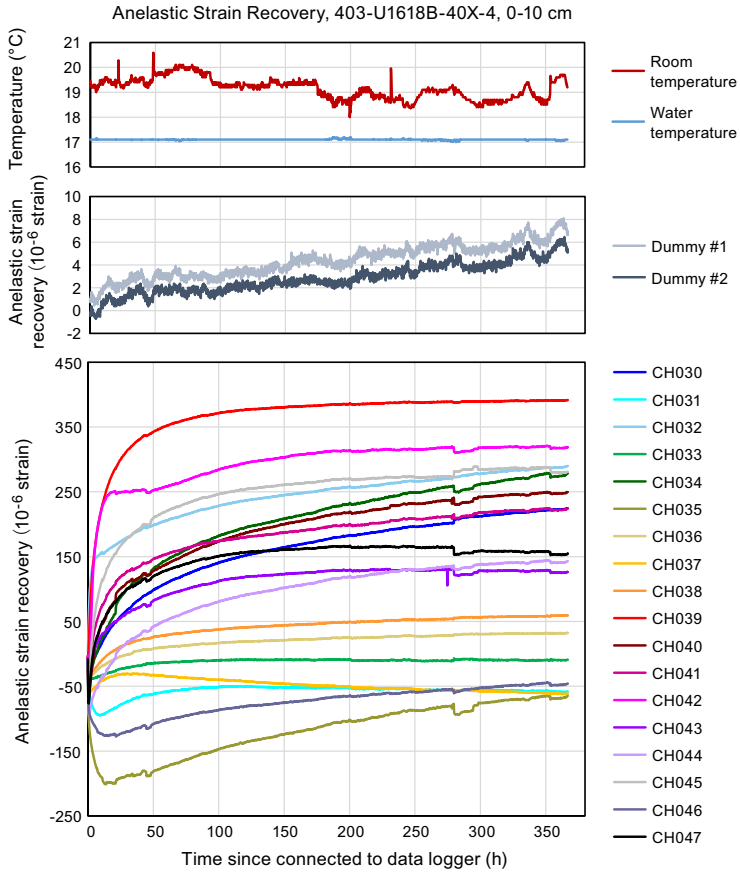

Figure F32. ASR initial results, Sample 403-U1618A-40X-4, 0–10 cm. Top: temperature monitoring data used to ensure water bath temperatures were stable. Middle: results from a dummy channel used to ensure that the data logger was operating correctly. Bottom: average values of the 11 ASR measurements collected from the 18 strain gauges every 10 min over ~14 days.

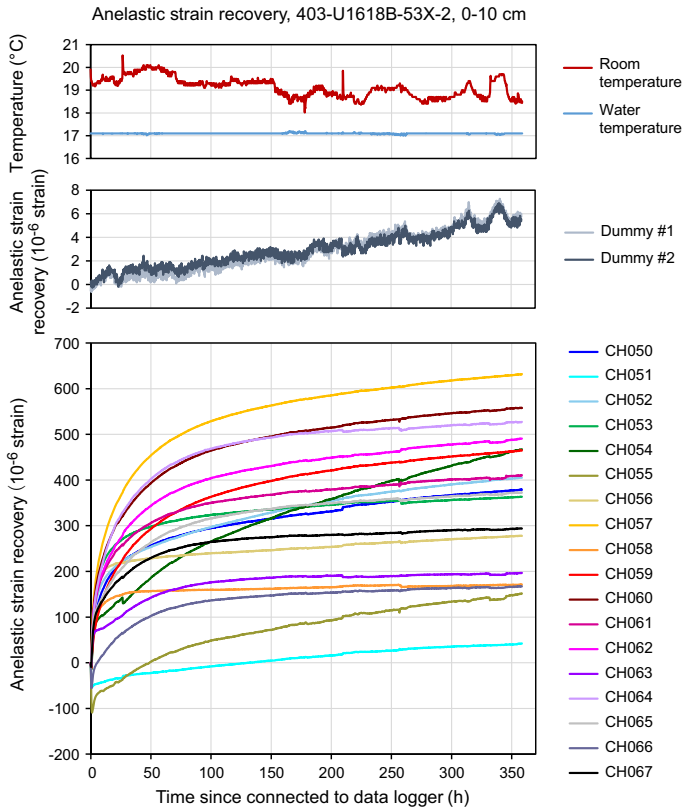

Figure F33. ASR initial results, Sample 403-U1618B-53X-2, 0–10 cm. Top: temperature monitoring data used to ensure water bath temperatures were stable. Middle: results from a dummy channel used to ensure that the data logger was operating correctly. Bottom: average values of the 11 ASR measurements collected from the 18 strain gauges every 10 min over ~14 days.

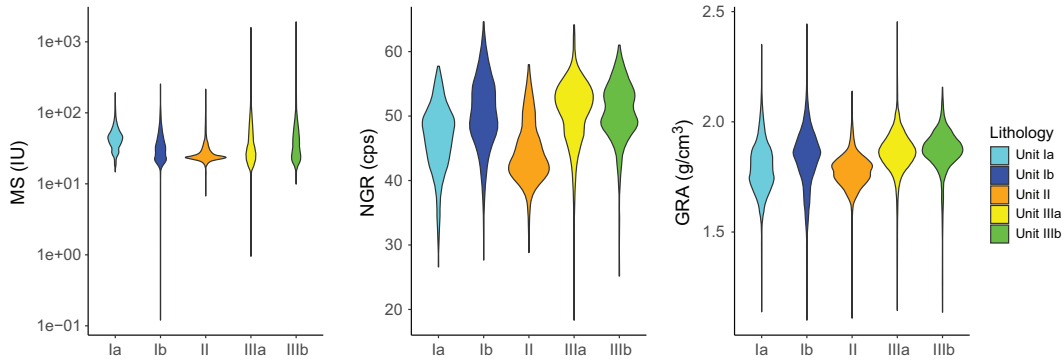

Figure F34. Violin plots summarizing physical property associations with preliminary lithostratigraphic units/subunits, Hole U1618A. cps = counts per second.

7. Stratigraphic correlation

Correlations between holes at Site U1618 were accomplished using Correlator software (version 4.5.4). In the upper part of the holes (above 125 mbsf), tie points were primarily established with WRMSL MS and GRA bulk density data. Below this depth, gas caused substantial expansion of the sediments and in some cases extrusion out of the top and bottom of the core liner and onto the rig floor; expansion also resulted in many gaps in the cores. In some cases, expansion caused shattering of the liners and made it difficult to extract them from the core barrel. These factors resulted in relatively high growth factors, disturbed sediment (especially in some of the first sections of

XCB cores in Holes U1618A and U1618B), and voids, which affected the physical properties (e.g., density) and resulted in stratigraphic inconsistencies among holes. In the deeper sections (below 125 mbsf), the occurrence of authigenic iron sulfide minerals, as well as diagenetic overprint, added uncertainty to the correlation (Table **T7**) and splice (Table **T8**). WRMSL GRA bulk density and NGR data were helpful but were not used in making the correlations. Although we relied on MS data (Figure **F35**), we note that the NGR data are less noisy than other data sets (Figure **F36**) and may be useful in comparing with climate records (e.g., coarse sediments delivered by ice sheet versus clay-rich sediments mostly delivered by bottom currents). We constructed two spliced intervals, one from 0 to 294.2 m core composite depth below seafloor (CCSF) based on correlations among the three holes and another from 294.2 to 474.15 m CCSF based on a correlation between Holes U1618B and U1618C. For this deeper interval, expansion of the cores made it difficult to correlate, and at several gaps we appended the cores based on an average growth factor of ~1.1 of the previous cores (Figure **F35**; Table **T8**). Thus, parts of the sedimentary sequence were difficult to correlate between holes, and postcruise work will be required to verify some of the tentative tie points used to construct the splice.

The CCSF scale is anchored to the mudline of Core 403-U1618C-1H, which is assigned the depth of 0 m CCSF. From this anchor, we worked downhole using Correlator to establish a composite stratigraphy on a core-by-core basis. The match between holes is relatively well constrained within the spliced intervals, although there are gaps throughout the splice. Between 0 and ~200 m CCSF, the splice is secured except to a few tentative tie points (Table **T8**). Below this depth, incomplete recovery and sediment expansion resulted in more gaps, especially in Holes U1618A and U1618B, that were not fully covered by Hole U1618C and need to be confirmed or secured with additional analyses (e.g., X-ray fluorescence data). We approached the construction of the splice by mainly using the best recovered stratigraphy of Hole U1618C as the backbone, where possible, and using primarily Hole U1618A to fill the core gaps down to 294 mbsf (Figure **F35A–F35C**), where coring in Hole U1618A was terminated. Below this depth, we used Hole U1618B to fill the gaps in Hole U1618C (Figure **F35D**). We have provided the exact position of the tie points we used to determine the offsets for cores that were not used in the splice (Table **T7**); this information will make it easier for studies that utilize samples from intervals that are outside the splice to compare data to records from the splice.

The cumulative offset between the mbsf and CCSF depth scales is nearly linear (Figure **F37A**), but close inspection of the cumulative offset as a function of depth (mbsf) (Figure **F37B**) reveals that in the upper section (0 to ~140 mbsf), cores from all three sites consistently show minimal growth factor because of low expansion associated with the release of overburden combined with methane gas expansion. The growth factors below ~140 mbsf are strongly affected by making hole-to-hole correlations, and expansion and the loss of some sediment is also affecting the core offsets. In a few intervals, we have small floating sections that were difficult to correlate. Because of the expansion and incomplete recovery in all three holes, we had to include offsets between cores based on an average growth factor in the preceding cores. This uncertainty was large in Hole U1618B, resulting in decreasing cumulative offsets in some cores (Figure **F37B**), which obviously is incorrect, and we avoided using these parts of the records in the splice. In summary, we are very confident about the splice between 0 and 140 mbsf. Below this depth, the splice may be inaccurate, but we used mainly sections from Hole U1618C, which is more reliable than Holes U1618A and U1618B. Calculation of mass accumulation rates based on the CCSF scale should account for the expansion by dividing apparent depth intervals by the appropriate growth factor.

Table T7. Affine table for cores recovered at Site U1618. **Download table in CSV format.**

Table T8. Splice interval table, Site U1618. **Download table in CSV format.**

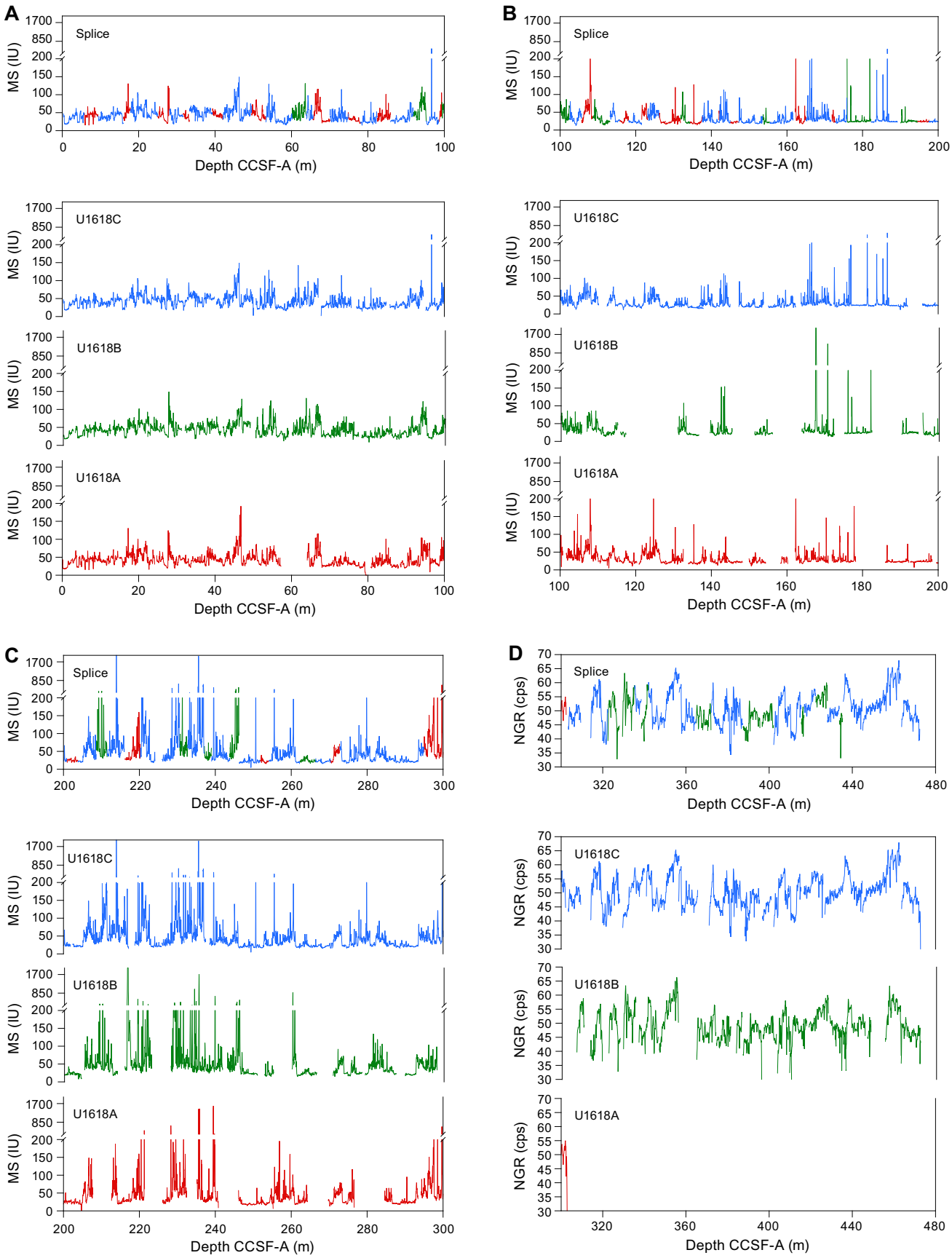

Figure F35. WRMSL MS data, Holes U1618A–U1618C. Top: MS splice constructed by combining data from all holes. Break in scale is due to high values at some depths with high concentration of authigenic greigite minerals.

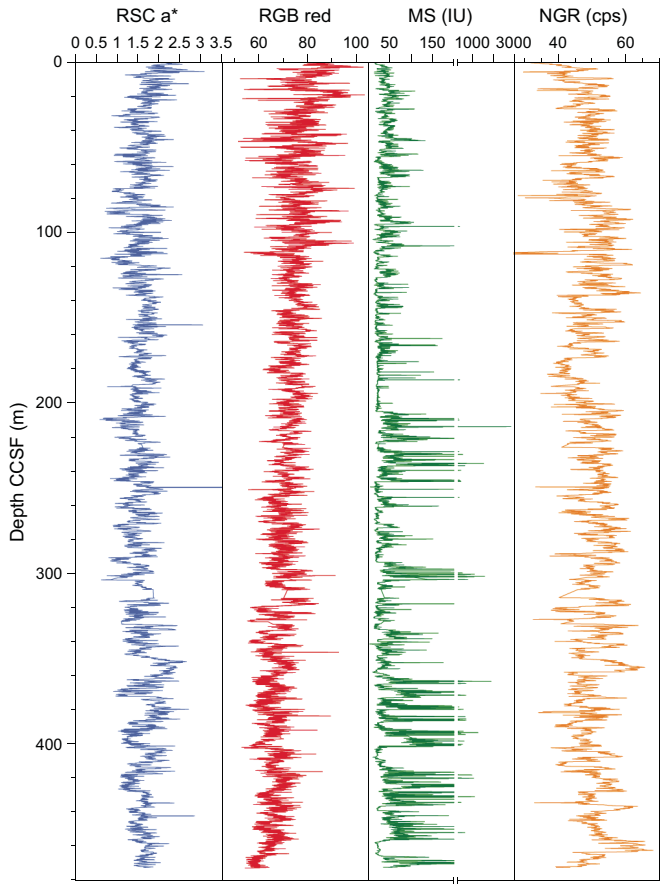

Figure F36. Spliced composite records of reflectance spectroscopy and colorimetry (RSC) a*, red-green-blue (RGB) red, WRMSL MS, and NGR, Site U1618. cps = counts per second.

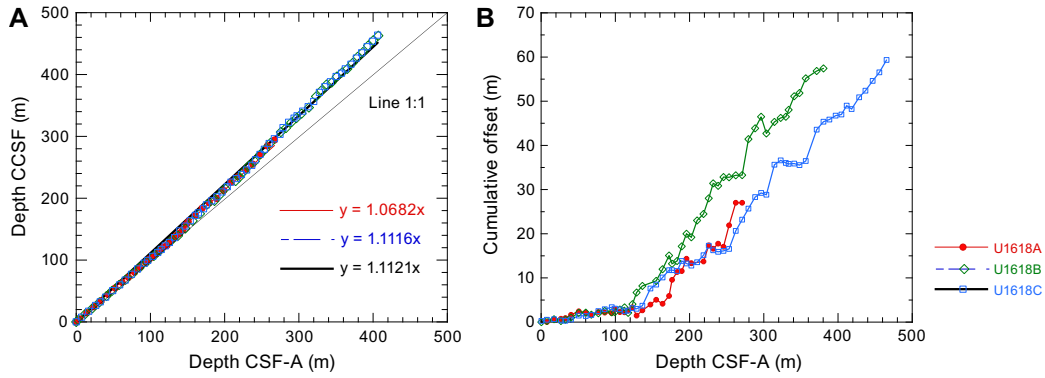

Figure F37. Depth scale offset, Site U1618. A. Comparison of CSF-A and CCSF depth scales in the splice and equations to convert between them. B. Growth of cumulative depth offset.

8. Geochemistry

Samples for IW chemistry, bulk sediment geochemistry, and headspace gas were analyzed at Site U1618. The main findings from IW analysis suggest anaerobic conditions below approximately 20 mbsf and possible fluid migration in the sediments resulting in diachronous authigenic iron sulfide mineral formation and authigenic carbonate formation. Elemental analysis of solid material revealed carbon and nitrogen content across most intervals that is typical of the Arctic region (Stein and Stax, 1996). Headspace hydrocarbon gas measurements showed low concentrations in

the uppermost 16.50 m and a sharp peak in methane below this depth, indicative of biogenic methanogenesis.

Although Site U1618 is not located near a known gas hydrate–related bottom-simulating seismic reflector, the headspace gas, IW geochemistry, and bulk sediment geochemistry indicate the presence and influence of gas hydrate and free gas at depth.

8.1. Interstitial water chemistry

A total of 46 IW samples were squeezed from 5 or 10 cm whole-round samples. Typical samples yielded 10 cm^3 of water for subsequent analysis. A suite of major and trace elements (Table **T9**) were measured via ion chromatography (IC) and inductively coupled plasma (ICP) spectroscopy, respectively.

8.1.1. pH, chloride, sodium, and salinity

The measured pH of the IWs varied between 7.7 and 8.2 at Site U1618, with no discernible trends. The concentrations of chloride (Cl), sodium (Na), and salinity are conservative tracers used to investigate gas hydrate formation and dissociation in sediments (e.g., Ussler and Paull, 2001; Kastner et al., 2008). Gas hydrate dissociation involves breaking down hydrates in the sediments, which results in the freshening of IWs, whereas gas hydrate formation results in an increased salinity profile of IWs. The Cl concentrations at Site U1618 show a linear decrease from 559 mM at 12.30 mbsf to 377 mM at 406.26 mbsf. This linear decrease of Cl suggests diffusion of fluids deeper than 406.26 mbsf, which may indicate that gas hydrate dissociation occurred deeper than core recovery. The Na concentration (measured via IC) also tends to decrease with depth from 477 mM at 12.30 mbsf to 338 mM at 406.26 mbsf. Salinity linearly decreases downcore from 34 to a minimum of 22 at 406.26 mbsf. The salinity of 34 is comparable to established average seawater values, and the linear decrease down to 22 is indicative of the freshening of the IWs, which may be due to gas hydrate dissociation throughout Hole U1618A. Chloride, Na, and salinity concentration-depth profiles are shown in Figure **F38**.

8.1.2. Sulfate, alkalinity, iron, and manganese

The sulfate–methane transition zone (SMTZ) is characterized by sulfate depletion and methane increase. The depth of the SMTZ can vary and is generally near the sediment/water interface in locations of high methane supply (Borowski et al., 1996; Graves et al., 2017). Sulfate at Site U1618 is rapidly depleted from 9 mM at 12.30 mbsf (well below the established average seawater value of 28 mM; e.g., Bruland and Lohan, 2006) to ~0.8 mM at 20.31 mbsf, where it remains at values ≤ 1 mM. The rapid depletion of sulfate in the IWs corresponds to an increase in methane concentrations in the headspace samples (described below). This suggests the SMTZ at Site U1618 is

Table T9. IW major and trace elements, Site U1618. **Download table in CSV format.**

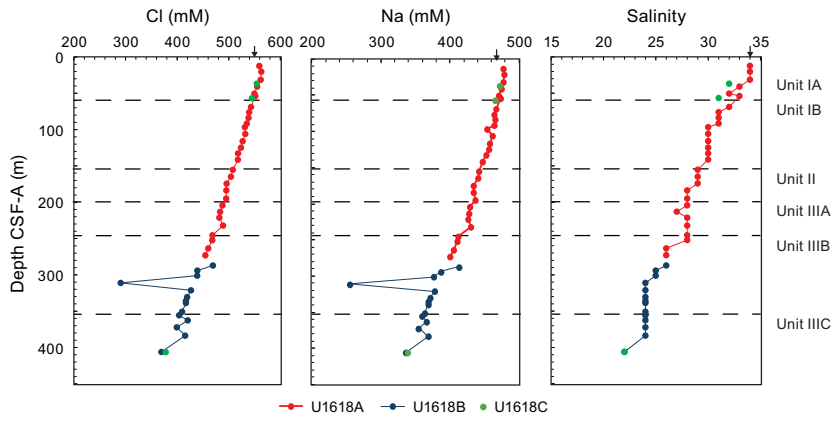

Figure F38. IW chloride, sodium, and salinity, Site U1618. Black arrows = average seawater values.

shallow, likely somewhere between 12.30 m and 20.31 mbsf. A shallow SMTZ is also supported by the measured alkalinity data. Alkalinity values increase from 14 mM at 12.30 mbsf to a maximum of 19 mM at 20.31 mbsf. This increase is consistent with the production of bicarbonate that occurs at the SMTZ due to the anaerobic oxidation of methane (AOM), as follows:

$$CH^4 + SO_4^{2-} \rightarrow HCO_3^- + HS^- + H_2O.$$

There are trace amounts of sulfate at 53.81, 200–250, and 350–400 mbsf ranging ~3–5 mM; the cause behind this slight increase is unknown.

Iron decreases from 33 to ~1 µM concentrations from 12.30 to 20.31 mbsf, suggesting Fe reduction above the SMTZ. Iron concentrations slightly increase to ~3 µM between 40 and 50 mbsf, where Fe concentrations then remain at values ≤ 1 µM, except for an increase to ~16 µM at 287.03 mbsf. The formation of authigenic iron sulfide minerals in Lithostratigraphic Unit II and Subunits IIIA and IIIC may explain the low Fe concentrations in the IWs. Manganese (Mn) decreases from 6 µM to near 3 µM concentrations from 12.30 to 20.31 mbsf, also suggesting Mn reduction above the SMTZ. Below the SMTZ, Mn concentrations tend to fluctuate between near 0 to ~2 µM in the IWs. In general, the decrease of Fe and Mn in the IWs is assumed to be due to incorporation into diagenetic mineral phases. Sulfate, alkalinity, Fe, and Mn concentration-depth profiles are shown in Figure **F39**.

8.1.3. Calcium, magnesium, strontium, silicon, barium, lithium, boron, bromide, and potassium

The calcium (Ca) and magnesium (Mg) trends in the IWs are typical of those observed within the SMTZ, as well as within the methanogenic zone, and may also include processes of silicate weathering and authigenic mineral formation. Calcium decreases from 6 mM at 12.30 mbsf to 3 mM at 40.87 mbsf, where Ca begins to increase and continues to increase downcore. The decrease of Ca in the IWs between 12.30 and 40.87 mbsf corresponds to authigenic carbonate mineral precipitation (see **Lithostratigraphy**). The formation of authigenic carbonates at this depth is also consistent with the typical reaction to form carbonate during AOM, where bicarbonate produced during AOM reacts with the Ca in IWs to form carbonate (Graves et al., 2017). The continuous increase of Ca in the IWs with depth may be attributed to the formation of siderite, where Fe would partially replace the Ca in the carbonate minerals; this may explain the release of Ca and the decrease of Fe, while also supporting carbonate mineral formation observed throughout the cores. Similar to Ca, Mg between 12.30 and 40.87 mbsf decreases from 43 to 33 mM and strontium (Sr) decreases from 78 to 72 µM, which suggests Mg and Sr may also be incorporated into authigenic carbonate minerals. Additionally, dolomite formation below the SMTZ cannot be completely excluded, given that the concentration of Mg continues to decrease with depth, suggesting removal from the IWs. Silicon (Si) concentrations fluctuate with depth. The increases of Si concentration in IWs in Lithostratigraphic Unit II and Subunits IB and IIIB (lower) are consistent with Si release due to the alteration of silicates in methanogenic sediments. It is possible that the Si

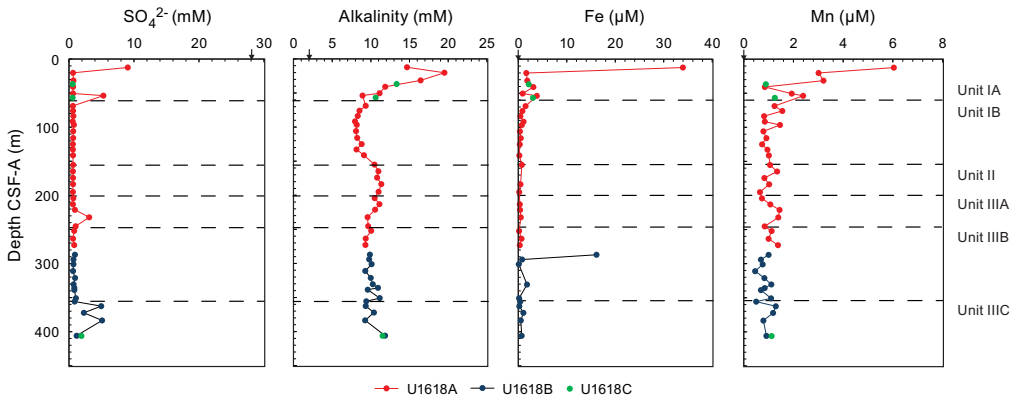

Figure F39. IW sulfate, alkalinity, iron, and manganese, Site U1618. Black arrows = average seawater values.

trend is also reflecting Si from diatoms dissolved in the alkaline pore water. Diatoms, which are phytoplankton that build their frustules from Si dissolved in seawater, were not found in the sedimentary sequence below the uppermost sample. There is likely marine barite formation and dissolution within Unit I, given that changes in dissolved barium (Ba) occur within this cored interval. The dissolved Ba shows barite formation above the SMTZ at 12.30 mbsf. The subsequent increase in dissolved Ba within and below the SMTZ (20.31–68.84 mbsf) is a result of marine barite dissolution in the sulfate-depleted pore water. Lithium (Li) in the IW is unique, increasing with depth to ~242 µM (Hole U1618C) at 406.26 mbsf. Specifically, the increase in Li concentration within Subunits IIIB and IIIC (~300–406.26 mbsf) suggests diffusion from a Li-rich fluid that is deeper than core recovery. It is likely the Li-rich fluids are related to hydrothermal circulation (Zhang et al., 1998) and fluid flow, which has been observed at the Vestnesa Ridge (Bünz et al., 2012). The Ca, Mg, Sr, Si, Ba, and Li concentration-depth profiles are shown in Figure **F40**. Potassium (K) (measured via IC) decreases from 11.4 mM (above average seawater values; e.g., Bruland and Lohan, 2006) to 4 mM with depth, well below average seawater values (10.2 mM), consistent with incorporation into authigenic mineral phases within methanogenic sediments. Boron (B) concentrations are higher than average seawater (416 µM, e.g., Bruland and Lohan, 2006) to 115.91 mbsf, where concentrations subsequently decrease with depth to near 200 µM. The K and B trends (Figure **F41**) are consistent with authigenic mineral (e.g., carbonate) formation. Bromide concentrations linearly increase with depth to >2 mM, with the exception of a slight decrease to 1.5 mM.

8.1.4. Phosphate and ammonium

The phosphate concentration increases from 20 µM at 12.30 mbsf to 72 µM at 20.31 mbsf, followed by a constant decrease to ~6 µM at 406.26 mbsf. The relatively higher phosphate concentrations in the upper meters at Site U1618 are most likely due to organic matter remineralization, which is a diagenetic process driven by photosynthetic activity. The ammonium concentrations increase from ~1 mM at 12.30 mbsf to ~3 mM at 406.26 mbsf, with the highest ammonium concentration (~4 mM) observed at 232.14 mbsf. The increase with depth of ammonium in the pore

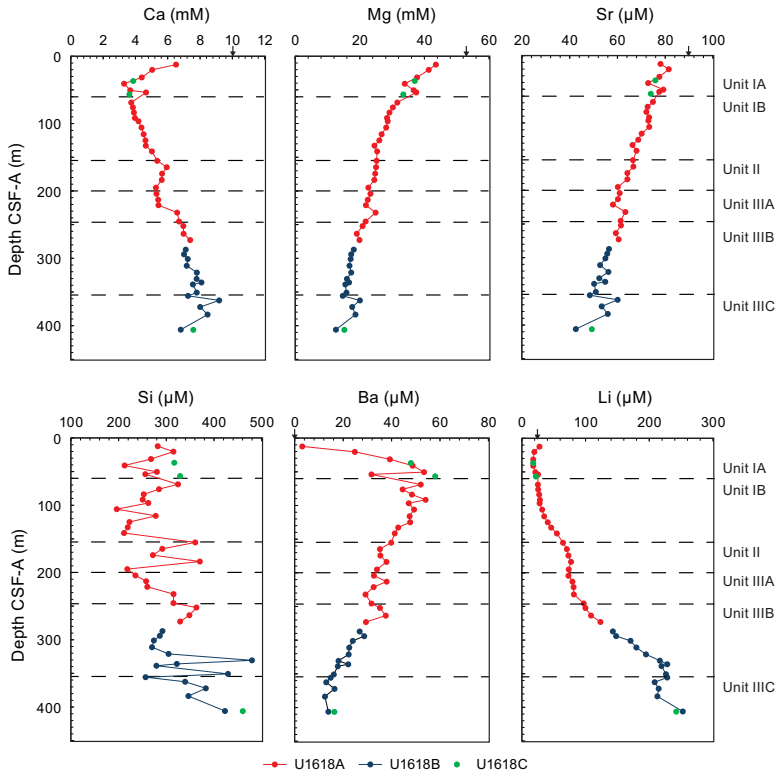

Figure F40. IW calcium, magnesium, strontium, silicon, barium, and lithium, Site U1618. Black arrows = average seawater values.

water is also indicative of organic matter diagenesis and supports the interpretation of the measured phosphate data. The phosphate and ammonium concentration-depth profiles are shown in Figure **F42**.

8.2. Sedimentary organic geochemistry

Shipboard solid-phase analysis at Site U1618 involved measurements of total inorganic carbon (TIC; i.e., $CaCO_3$), total nitrogen (TN), total carbon (TC), total organic carbon (TOC; calculated as TC – TIC), and total sulfur (TS) (Table **T10**) using shipboard plastic cylinder sampling (sample type CARB). The sedimentology team identified intervals for CARB samples from Holes U1618A–U1618C, resulting in a total of 43 samples taken. These samples are not systematically spaced, and they include representation of both major and minor lithologies.

The TC content in the sedimentary sequences of Holes U1618A–U1618C is generally high, with most values exceeding 0.5 wt%. Specifically, there are peaks of about 4 wt% at 80.92 mbsf in Hole U1618A, of about 4 wt% at 263.28 mbsf Hole U1618B, and of approximately 6 wt% at 372.35 mbsf in Hole U1618C. $CaCO_3$ content varies with depth, ranging 0–40 wt%, with peaks corresponding closely to TC peaks in each hole. This suggests that the authigenic carbonate minerals contribute significantly to the TC variations because biogenic carbonates (e.g., foraminifers and nannofossils) are generally in low abundance (see **Biostratigraphy and paleoenvironment**) and authigenic mineral was observed at Site U1618 (see **Lithostratigraphy**).

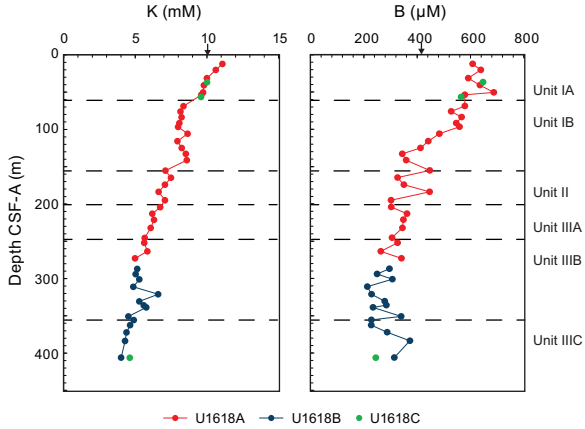

Figure F41. IW potassium and boron, Site U1618. Black arrows = average seawater values.

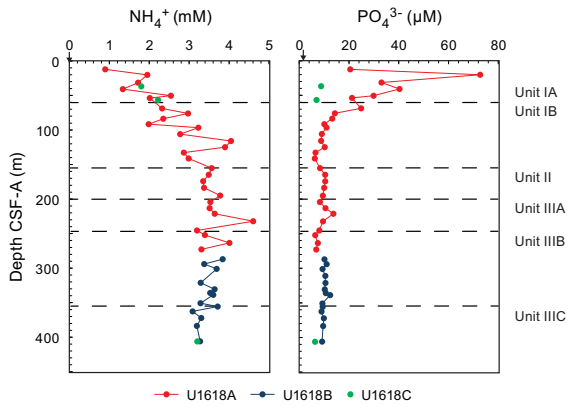

Figure F42. IW ammonium and phosphate, Site U1618. Black arrows = average seawater values.

Table T10. Bulk sediment geochemistry, Site U1618. **Download table in CSV format.**

The TOC content in Holes U1618A–U1618C ranges 0–2 wt%. Generally, TOC content is lower in the upper layers (approximately above 30 mbsf) and increases downhole to 80.92 mbsf. Below this depth, a decreasing trend is observed in Hole U1618A, whereas no distinct trends are noted in Holes U1618B and U1618C. The TN content in Holes U1618A–U1618C ranges 0–0.15 wt%, typically lower in the upper sediment layers and gradually increasing with depth and showing fluctuations. The ratio of TOC/TN (C/N), which is commonly used to identify sources of sedimentary organic matter (e.g., Meyers, 1997), varies from 7 to 23 at Site U1618. C/N ratios ranging between 4 and 10 suggest a marine origin, primarily from marine algae; C/N ratios of 20 or higher indicate a terrestrial origin (e.g., Meyers, 1994, 1997). The C/N ratios at this site vary within 5 to 25, suggesting organic matter is sourced from both continental (e.g., ice sheet derived) and marine origins. The sediment grain size affects C/N ratios, with fine-grained sediments generally having lower C/N ratios compared to coarse-grained sediments (e.g., Meyers, 1997). The higher C/N ratios correlate well with coarse-grained sediments (see **Lithostratigraphy**), supporting a terrestrial origin. The TS content in Holes U1618A–U1618C ranges between 0 and 1 wt% down to 383.03 mbsf, where there is an increase of TS content to ~3 wt%, and correlates with the observed sulfide minerals at depth within the cores. Figure **F43** illustrates the downcore profiles of $CaCO_3$, TOC, and TN contents (in weight percent) and C/N ratios at Site U1618, and Figure **F44** illustrates the downcore profile of TS content (in weight percent) at Site U1618.

8.3. Headspace gas geochemistry

As part of routine environmental protection and safety monitoring, headspace hydrocarbons were analyzed at Site U1618 (Figure **F45**; Table **T11**). Samples for headspace gas analysis were taken at a resolution of one sample per core. For Hole U1618B, samples were taken at a deeper depth than for Holes U1618A and U1618C. A total of 122 samples were analyzed for headspace hydrocarbons.

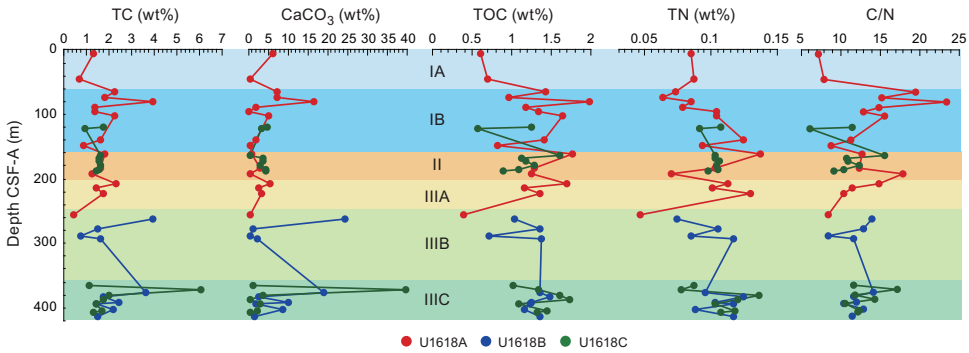

Figure F43. Bulk sediment contents of $CaCO_3$, TC, TOC, TN, and C/N ratio, Site U1618.

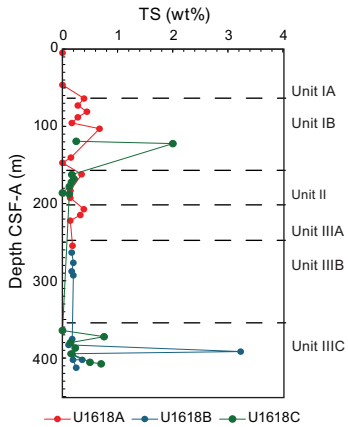

Figure F44. Bulk sediment contents of TS, Site U1618.

For safety considerations, the ratio of methane (C_1) to ethane (C_2) is generally used to obtain quick information about the origin of the hydrocarbons (i.e., to distinguish between biogenic gas and gas migrated from a deeper source of thermogenic hydrocarbons).

Methane concentrations were low in the uppermost 16.50 m, and ethane was not detected in this interval, indicating a biogenic source of gas (Figure **F45**). At approximately 40–90 mbsf, methane concentrations sharply increased by about three orders of magnitude, reaching 51,970 ppmv at 45.86 mbsf. At 31.48 mbsf, the first amounts of ethane (3.78 ppmv) were detected, with a methane/ethane (C_1/C_2) ratio of 4866 (Figure **F45**). Ethane gradually increased to about 350 mbsf, after which a decreasing trend downcore appeared, with a sharp increase below approximately 406 mbsf. Propane was first detected below 96.65 mbsf in Hole U1618B, whereas *iso*-butane and *n*-butane first appeared below 204.30 mbsf. Traces of *n*-pentane, *iso*-hexane, and *n*-hexane were found below 263.63 mbsf in Hole U1618A, below 406.14 mbsf in Hole U1618B, and below 403.36 mbsf in Hole U1618C. In these intervals, C_1/C_2 ratios less than 100 were observed, suggesting a thermogenic source of hydrocarbons.

Additionally, six void gas samples (VACs) were analyzed from Hole U1618A where voids were observed through the core liner on the core receiving platform. The VAC samples had methane and ethane concentrations that were two to three orders of magnitude higher than the headspace samples. The respective maximum values for methane and ethane were 1,011,937 and 251 ppmv at 106.07 and 132.85 mbsf, respectively.

Gas hydrates are ice-like structures found in the subseafloor in deep marine and continental shelf environments. They form when water freezes around methane gas or other higher molecular

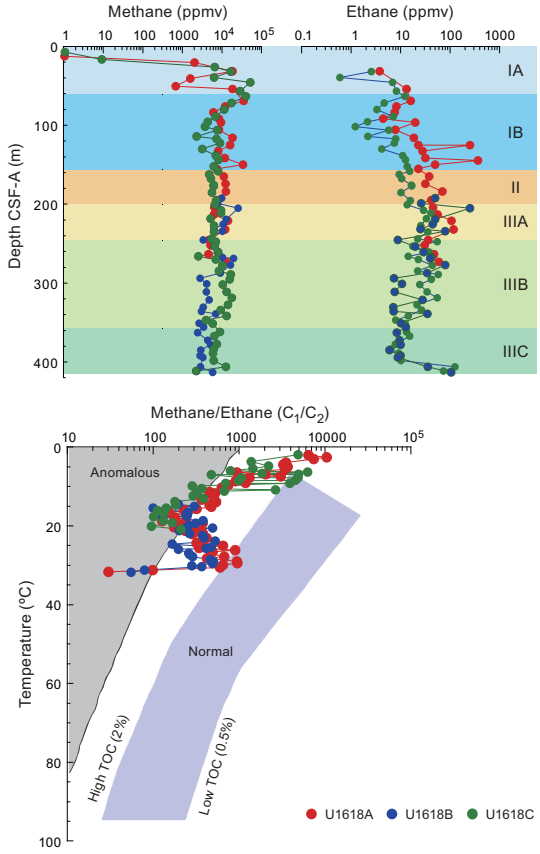

Figure F45. Methane (CH_4) and ethane (C_2H_6) concentrations and methane/ethane (C_1/C_2) ratios measured on headspace samples from 5 cm^3 of sediment, Holes U1618A–U1618C.

Table T11. Headspace gas hydrocarbon concentrations, Site U1618. **Download table in CSV format.**

weight hydrocarbons (e.g., ethane or propane) under cold temperatures and high-pressure conditions (Sloan, 1998). Gas hydrate stability zones in marine sedimentary sequences can be estimated from pressure and downhole temperature data (Brooks et al., 1983). Site U1618 had a water depth of 1196 m, and Hole U1618A had a measured geothermal gradient of 75°C/km (see **Downhole measurements**). Thus, the gas hydrate stability zone was calculated to extend to approximately 214 mbsf. Downhole temperature was also measured on three lower depths in Hole U1618B, revealing a lower geothermal gradient of 72°C/km in this hole, either suggesting a change in the rate of temperature increase with depth or a deeper gas hydrate stability zone in this hole. The occurrence of gas voids in the core liner and very high gas concentration of the VACs may possibly be related to the presence of hydrates that disassociated at depth and/or when exposed to lower pressure environments as the cores were brought up to sea level.

Authigenic carbonates precipitate at the upper and lower depths where gas hydrates exist, affecting the chemical composition of the IW and altering alkalinity (Rodriguez et al., 2000). The high peaks of $CaCO_3$ content at Site U1618 might be due to authigenic carbonate appearing in the upper and lower sections of intervals believed to contain gas hydrates. Additionally, slight changes in alkalinity and other major elements (i.e., Ca and Mg) occur in these intervals. These changes in major elements and alkalinity, along with carbonate precipitation, support the presence of gas hydrates. Although Site U1618 did not show clear signs of gas hydrates in seismic data, we detected geochemical signatures associated with gas hydrates, including an increase in alkalinity around 130–230 mbsf.

9. Microbiology

9.1. Site U1618

SedaDNA samples were taken in contamination-controlled conditions at low resolution in Hole U1618B to examine the entire record and at a higher resolution in Hole U1618C to examine the time interval from the MIS 6/5e glacial–interglacial transition to the recent past. In total, 126 sedaDNA samples were taken across the two holes (Table **T12**); these samples will be analyzed postcruise. The drill fluid contains seawater, which is a potential source of biological contamination, and therefore the drill fluid was infused with perfluorodecalin (PFD) tracers to assess whether sedaDNA samples had been contaminated. A total of 147 PFD samples were analyzed at this site shipboard on an Agilent 6890 gas chromatograph with Micro-electron capture detector (Table **T12**). Results from the shipboard analyses of the control samples are discussed below.

9.1.1. Hole U1618B

Hole U1618B was sampled at low resolution (one sample per core) for the full 414 m record (Figure **F46**; Table **T13**). In total, 48 sedaDNA samples were taken on the core receiving platform.

Table T12. Summary of sedaDNA and chemical tracer samples, Site U1618. **Download table in CSV format.**

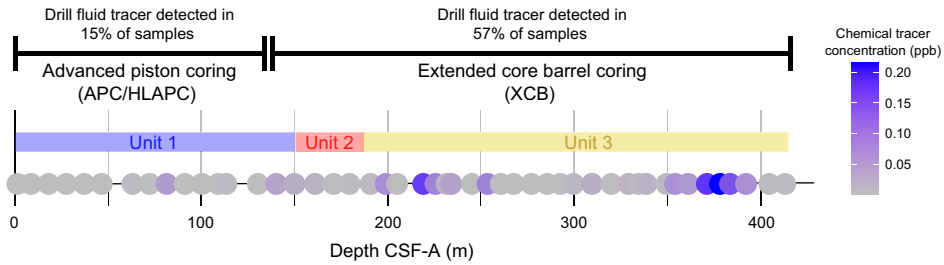

Figure F46. Low-resolution sedaDNA sampling, Hole U1618B. Dots = samples.

Table T13. List of sedaDNA negative chemical tracer controls, Site U1618. **Download table in CSV format.**

Preliminary shipboard chronological work suggests this sedaDNA record will span from the recent past to the Pliocene. Drill fluid in this hole was infused with 0.6 ng/L of PFD so that positive and negative PFD controls could be taken. The positive control was taken from a sample of drill fluid at the top of the sampled core and the negative control from directly adjacent to the sedaDNA sample. All positive drill fluid controls contained levels of PFD above background levels of 0.007 ppb (defined by the highest background levels of PFD in blank samples), indicating PFD was dispensed successfully into the drill fluid throughout coring in Hole U1618B (Table **T14**). Overall, the results from the negative controls showed drill fluid contamination was likely in 44% of sedaDNA samples from Hole U1618B. Coring with the APC/HLAPC system resulted in lower drill fluid contamination of sedaDNA control samples (15%) compared to coring with the XCB system (57%) (Figure **F46**). This contamination difference is likely due to the increased core disturbance (e.g., fracturing and biscuiting) produced by the XCB system. Nevertheless, these findings also indicate that it is possible to obtain uncontaminated sedaDNA samples with both types of coring approaches, extending the potential for sedaDNA studies in a wider range of drilling conditions than previously documented in marine sediments.

9.1.2. Hole U1618C

9.1.2.1. High-resolution record of the recent past to the lead up to the last interglacial

Hole U1618C was selected for high-resolution sampling of split core sections of the target interval spanning the MIS 6/5e transition to the present. In total, 78 sedaDNA samples were taken across the first three cores, which extend to ~26 mbsf (Table **T13**). These cores were obtained using the APC system. Analysis of PFD concentrations in the controls indicated PFD was correctly dispensed and 90% of the sedaDNA control samples were free from drill fluid contamination.

The precise sampling strategy for the target stratigraphic interval was developed dynamically and in collaboration with other shipboard scientists (Figure **F47**). A preliminary estimate of MIS 5e was determined after correlating MS data with well-dated regional records (Jessen et al., 2010) and comparing with the biostratigraphic events (i.e., nannofossils and diatoms biostratigraphy). In collaboration with the stratigraphic correlators, we used MS data to determine the possible position of MIS 5e and sampled across it to capture the transitions into (MIS 6 glacial termination) and out (MIS 4 glaciation) of this period of warmth. We further sampled across meltwater events to assess the paleoecological shifts associated with them. The location of Meltwater Pulse 1A (Deschamps et al., 2012) was identified based on well-established regional glaciomarine facies (Lucchi et al., 2013, 2015) observed on the split core surface.

Table T14. Positive chemical tracer controls, Site U1618. **Download table in CSV format.**

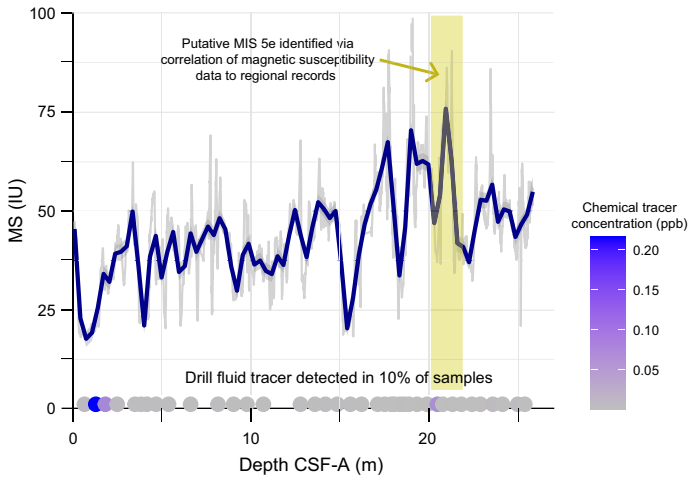

Figure F47. High-resolution sedaDNA targeted sampling of the recent past to MIS 5e, Hole U1618C. Blue line = MS data used to help refine sampling strategy, dots = samples.

9.1.2.2. Oldest preservation of sedaDNA

One sample was also taken from the middle of Section 2 of the last core (403-U1618C-62X) to test for the oldest preservation of sedaDNA at Site U1618. The preliminary chronology from this site (see **Biostratigraphy and paleoenvironment** and **Paleomagnetism**) suggests the bottom of the core may have crossed into the Pliocene, which would make any ancient DNA extracted from the sediment older than the 2 My old DNA recovered in Arctic permafrost, the oldest ancient DNA sequenced to date (Kjær et al., 2022).

For the best possible chance of an uncontaminated sample, the sample was taken from the interior of a biscuit, where the stratigraphic sequence is better preserved than in the unconsolidated gravy that is an artifact of XCB drilling. The PFD negative control from immediately adjacent to the sedaDNA sample showed no detectable PFD. However, this result needs to be interpreted with caution because all the positive PFD controls were also negative, suggesting there was a problem with the tracer in the drill fluid.

10. Downhole measurements

10.1. Formation temperature

During APC coring in Hole U1618A, in situ formation temperature was measured every third core (4H, 7H, 10H, and 13H) using the APCT-3 tool. After switching to XCB coring, in situ formation temperature was measured prior to Cores 35X, 403-U1618B-42X, and 53X using the SET2 probe. Temperature increased almost linearly with depth, and the slope of linear regression provides a typical geothermal gradient (78.8°C/km) for oceanic sediments compared with the statistical data set (Kolawole and Evenick, 2023) (Figure **F48**). The heat flow in the sediments and the temperature at the seafloor were calculated from the measured thermal conductivity in Cores 403-U1618A-15F through 37X, 403-U1618B-36X through 54X, and 403-U1618C-1H through 15F and the formation temperature measurements. Assuming a linear relationship between thermal conductivity and depth, the heat flow in the sediments and the temperature at the seafloor are approximately 98.5 mW/m^2 and –0.814°C, respectively.

10.2. Downhole logging

In Hole U1618B, downhole logging was conducted using the triple combo and FMS-sonic tool strings to obtain multiple in situ property measurements. Logging operations for these tools are illustrated in Figure **F49**. After the BHA was set at 79.6 m wireline log matched depth below seafloor (WMSF), the string was first lowered to 369.4 m WMSF for downlog while the caliper closed.

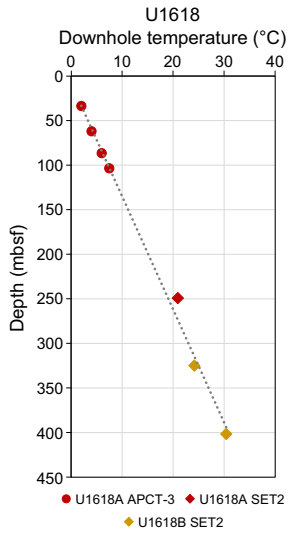

Figure F48. Formation temperature, Holes U1618A and U1618B. Dashed line = linear regression result.

A downlog of the Hostile Environment Litho-Density Sonde (HLDS) was not obtained. Subsequently, the tool string was pulled up for the first uplog from 379.2 to 288.8 m WMSF. To increase data recovery, the strings were lowered again to 370.1 m WMSF and pulled up to 0 m WMSF for the second uplog. After the triple combo tool string, the FMS-sonic string was lowered to 356.6 m WMSF. For the first image uplog, the FMS-sonic string was pulled up from 359.7 to 122.8 m WMSF. To increase data recovery, the tools were lowered again to 342.9 m WMSF and pulled up to 0 m WMSF for the second image uplog. The average peak-to-peak heave was estimated at 0.5 m, and the heave compensator was utilized during the logging operation.

Logging data were sent for processing to the Lamont-Doherty Earth Observatory (LDEO; Columbia University, USA) (Figure **F50**; Table **T15**). The data provide important information for core-log integration to understand the actual depth and thickness of each lithostratigraphic unit because most cores at this site suffered from gas expansion. Seismic imaging using the VSI was canceled because the *z*-axis accelerometer to correct the vertical position of data was out of order.

10.2.1. Triple combination

Overall, the triple combo successfully acquired borehole diameter, density, natural gamma ray, MS, and electrical resistivity. For several depth levels, however, the data should be interpreted with caution because the irregularly enlarged borehole affects eccentralization and/or good contact of tools with the borehole wall (Figure **F50**).

Logging data were collected for variations in the borehole diameter, which were measured using a hydraulic caliper on the HLDS during each uplog. Based on these caliper measurements, the borehole diameter was enlarged at almost all depths, indicating that washouts occurred while drilling mud circulated in Hole U1618B. Given the characteristics of sondes and methodologies, borehole diameter variation may affect the logging of MS and porosity. On a specific thin layer at ~120 m WMSF, we observed a rapid reduction of borehole diameter from ~11 to ~8.5 inches. Given the correspondence to the core description of Holes U1618A and U1618C (see **Lithostratigraphy**), this might be a mud cake that adhered to the borehole wall as water from the drilling mud moved into a permeable sand layer. Unfortunately, cores were not recovered from the same depth in Hole U1618B.

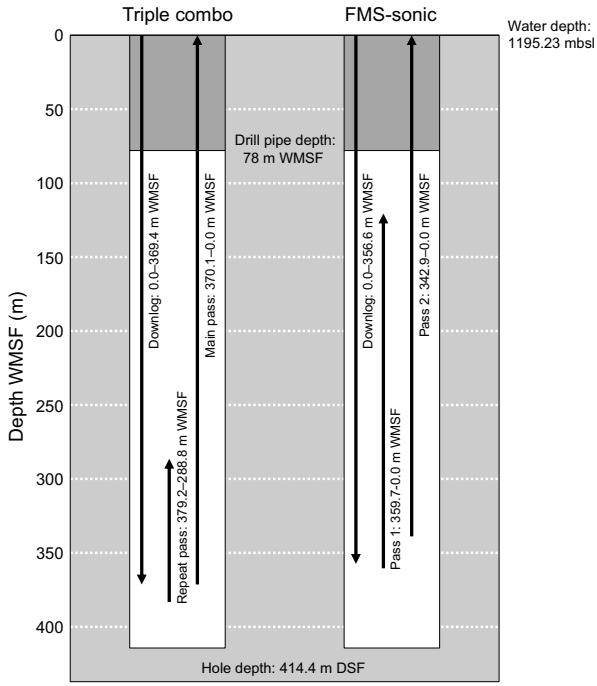

Figure F49. Downhole operations for triple combo and FMS-sonic tool strings, Hole U1618B. DSF = drilling depth below seafloor.

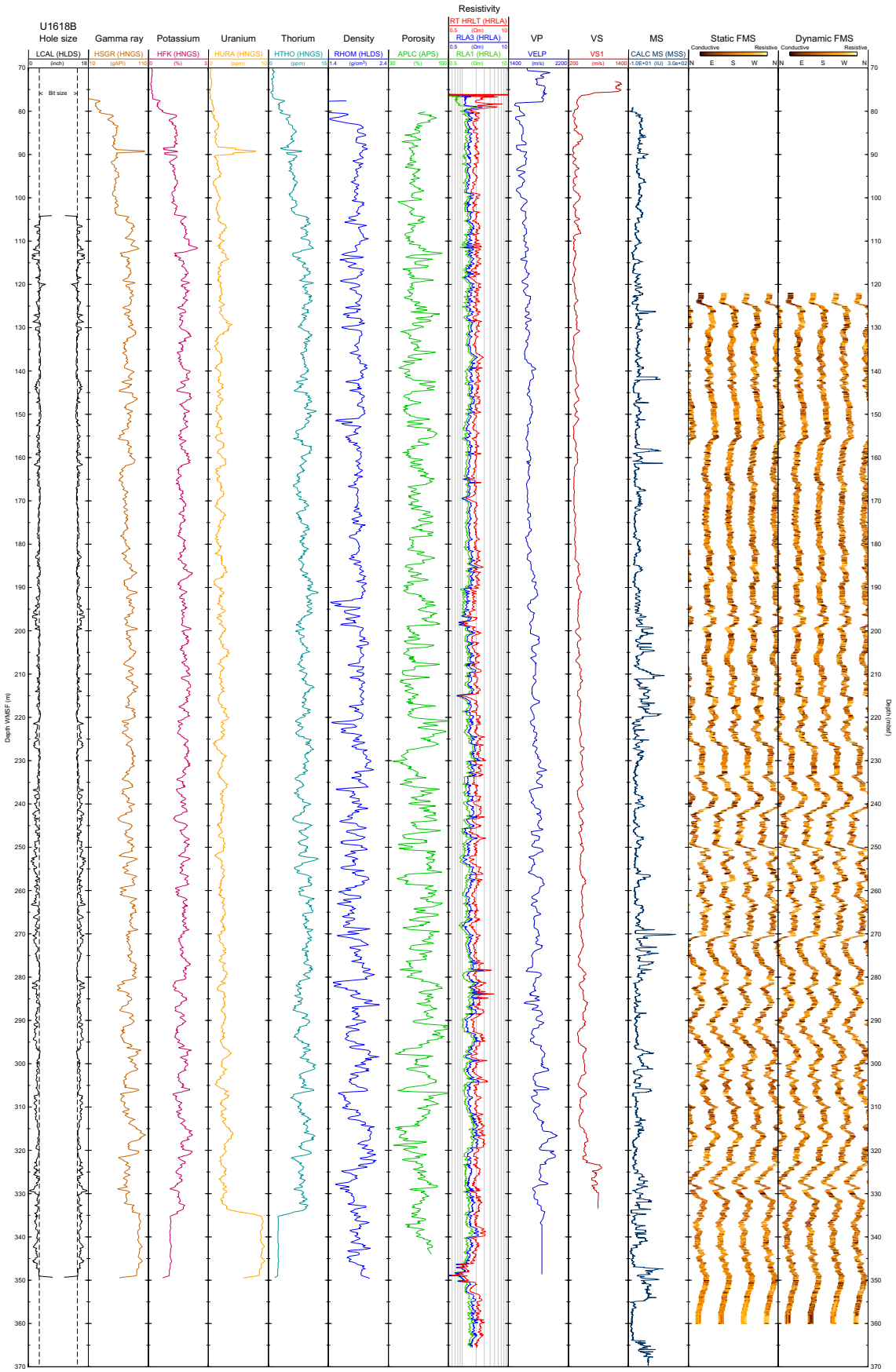

Figure F50. Downhole logging data from the triple combo and FMS-sonic tool strings, Hole U1618B. Data sets and abbreviations are shown in Table T15.

Natural gamma ray, density, and MS show almost the same trends as the shipboard scanning data. HLDS density log measurements from 82 to 350 m WMSF (below the drill pipe) are on average 1.88 g/cm^3 and do not show a significant downhole trend. Cyclic changes with increasing amplitude downhole were observed. Absolute values of the HLDS density measurements are very similar to densities derived from GRA bulk density core logging and discrete MAD measurements (Figure **F51A**).

Because of poor borehole conditions, the Accelerator Porosity Sonde (APS) likely did not obtain accurate porosity data (Figure **F50**), but relative cyclic changes show correlation with density and electrical resistivity at several depths (Figure **F51B**). In addition, the gradual increase in amplitude of cyclical changes is similar to other parameters, such as natural gamma ray or density.

Downhole natural gamma ray was reported as total spectral gamma ray (HSGR) data and potassium (K), uranium (U), and thorium (Th) contents. Each K, U, and Th component was derived from the spectrum of total natural gamma ray counts and 256-window spectroscopy. For the total natural gamma ray measurements not influenced by the drill pipe (>104 m WMSF), the average value is 78 American Petroleum Institute gamma radiation units (gAPI). Cyclic amplitude fluctuations around this value were observed. The amplitude of these cyclic variations is higher in the lower part (>280 m WMSF) of the measurements. An interval of lower HSGR values occurs around 160–180 m WMSF. Potassium and uranium showed similar trend and fluctuation to HSGR, whereas thorium indicates relatively lower amplitudes. The HSGR data showed great similarity to natural gamma ray measured on cores with the natural gamma ray logger (Figure **F51C**), indicating that core and log depth scales can be readily correlated. The differences of the depth scales can be assumed to be less than 1 m. Absolute values of the HSGR in the upper 100 m are much lower because measurements were made through the drill pipe.

The Magnetic Susceptibility Sonde (MSS) provided data that range 0.91–234.19 SI and correspond well to core measurements using the WRMSL (Figure **F51D**). MSS showed some peaks much higher than background that can be associated with the existence of authigenic iron sulfides (see **Physical properties**).

For electrical resistivity, laterologging using the High-Resolution Laterolog Array (HRLA) tool recorded multiple logs depending on the travel paths of electrical current: apparent resistivity from shallow to deep, as well as true resistivity. Resistivity ranged 1–3 Ω·m across most depths. At ~190–200 m WMSF, low resistivity that corresponds to logging of low density and high porosity was observed. Because electrical resistivity of formation is highly dependent on water content,

Table T15. Abbreviations and selected data for summary plots. **Download table in CSV format.**

String	Tool	Property	Explanation	Selected data for summary plots	Data range (WMSF)
Triple combo	HLDS		Hostile Environment Litho-Density Sonde		
		LCAL (HLDS)	DIT (Dual Induction Tool) Caliper (inch)	Main pass	104–349
	HNGS		Hostile Environment Gamma Ray Sonde		
		HSGR (HNGS)	HNGS Standard (total) Gamma Ray (API units)	Main pass	0–349
		HFK (HNGS)	HNGS Formation Potassium (%)	Main pass	0–349
		HTHO (HNGS)	HNGS Thorium (ppm)	Main pass	0–349
		HURA (HNGS)	HNGS Uranium (ppm)	Main pass	0–349
		RHOM (HLDS)	HLDS Corrected Bulk Density (g/cm^3)	Main pass	77–349
	APS		Accelerator Porosity Sonde		
		APLC (APS)	APS Near/Array Corrected Limestone Porosity (%)	Main pass	80–343
	HRLA		High Resolution Laterolog Array Tool		
		RLA1 (HRLA)	HRLA Apparent Resistivity from Computed Focusing Mode 1 (Ω m)	Downlog	75–365
		RLA3 (HRLA)	HRLA Apparent Resistivity from Computed Focusing Mode 3 (Ω m)	Downlog	75–365
		RT HRLT (HRLA)	HRLA True Formation Resistivity (Ω m)	Downlog	75–365
	MSS				
			Magnetic Susceptibility Sonde	Main pass	79–369
FMS-sonic	DSI		Dipole Sonic Imager		
		VELP	DSI Compressional Velocity (processed from waveforms; km/s)	Reprocessed data of downlog	73–333
		VS1	DSI Shear Velocity, from DT1 (Lower Dipole; km/s)	Pass 2	73–333
	FMS		Formation MicroScanner		
			Borehole resistivity image	Pass 1	122–360

unless lithology changes, it suggests the presence of large pore spaces and high-water content, which is consistent with low density and high porosity in the same interval. The same trend of resistivity was found around 350 m WMSF.

10.2.2. FMS-sonic

The FMS-sonic string successfully logged natural gamma ray, acoustic velocity, and borehole resistivity images (Figure **F50**).

Because of hydrate-bearing sediments or free gas, automatic detection of the correct arrival time of the acoustic wave pulse was difficult for the raw data from the Dipole Sonic Imager (DSI). This is similar to failed *P*-wave measurements in the core laboratory on the ship. The raw velocities are likely to be a signal of wave conducted through slow sediments (i.e., soft sediments released from compression by drilling and washing) or fluid in the borehole, which may be a mixture of drilling mud and seawater. The data reprocessing provided us with meaningful *P*-wave velocity data (Figure **F50**). The reprocessed data show increasing values with depth. The calculated linear trend is 0.98 m/s. The trend is overlain by cyclic changes that mimic changes seen in the density. Maximum velocities of 2026 m/s were measured at 321 m WMSF.

Because of the capacity of the FMS calipers, borehole resistivity images have 25% recovery of all around the borehole walls at every depth. The images indicate no significant signal of borehole breakouts nor drilling-induced tensile fractures.

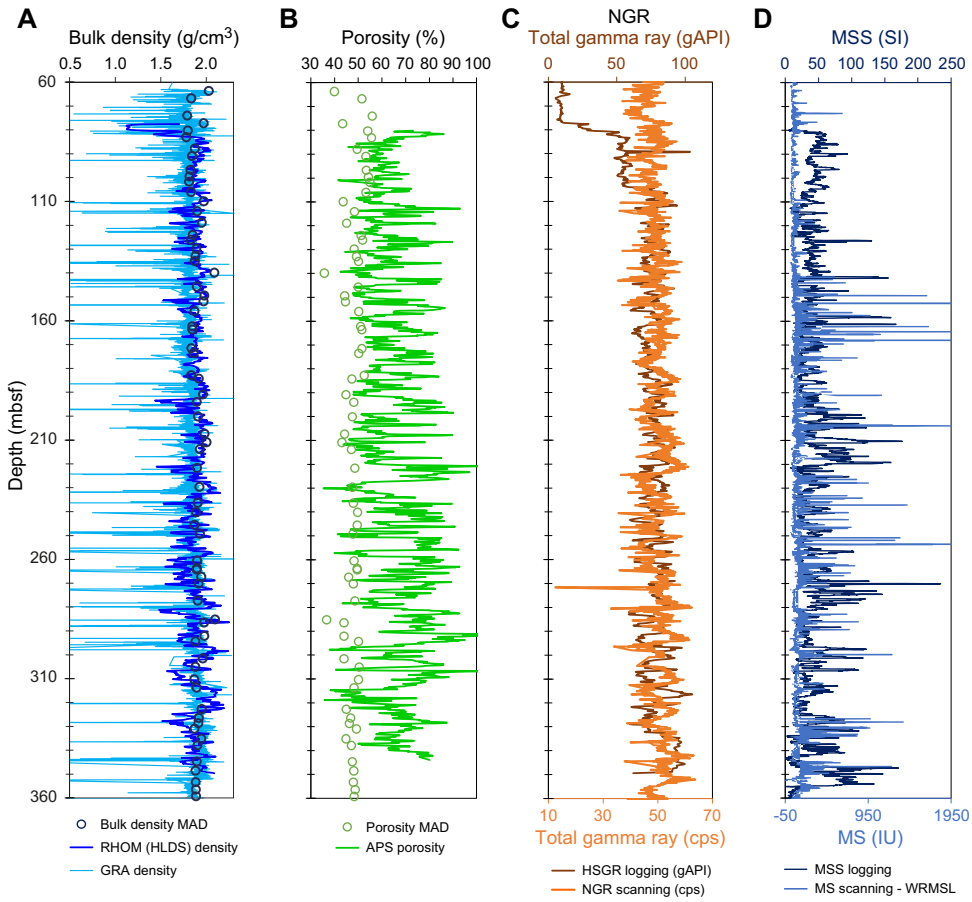

Figure F51. Core-log comparison derived from logging and core laboratory measurements, Hole U1618B. Data from shipboard tracks and downhole logging are plotted on the mbsf depth scale. Core logging data are plotted versus meters CSF, and downhole logging data are plotted versus meters WMSF. A. Density logs from HLDS data versus GRA density data. B. APS porosity data versus porosity from MAD measurements using discrete samples from Cores 403-U1618A-8H through 37X and 403-U1618B-34X through 47X. C. HSGR data versus natural gamma ray data. cps = counts per second. D. MSS data versus MS scanning data from the WRMSL.

References

Anthonissen, E.D., 2008. Late Pliocene and Pleistocene biostratigraphy of the Nordic Atlantic region. Newsletters on Stratigraphy, 43(1):33–48. **https://doi.org/10.1127/0078-0421/2008/0043-0033**

Bé, A.W.H., and Tolderlund, D.S., 1971. Distribution and ecology of living planktonic foraminifera in surface waters of the Atlantic and Indian Oceans. In Funnel, B.M. and Riedel, W.R., The Micropaleontology of Oceans. Cambridge, United Kingdom (Cambridge University Press), 105–150.

Borowski, W.S., Paull, C.K., and Ussler, W., III, 1996. Marine pore-water sulfate profiles indicate in situ methane flux from underlying gas hydrate. Geology, 24(7):655–658. **https://doi.org/10.1130/0091-7613(1996)024<0655:MPWSPI>2.3.CO;2**

Brooks, J.M., Barnard, L.A., Weisenburg, D.A., Kennicutt, M.C., II, and Kvenvolden, K.A., 1983. Molecular and isotopic compositions of hydrocarbons at Site 533, Deep Sea Drilling Project Leg 76. In Sheridan, R.E., Gradstein, F.M., et al., Initial Reports of the Deep Sea Drilling Project, 76: Washington, DC (U.S. Government Printing Office), 377–384. **https://doi.org/10.2973/dsdp.proc.76.108.1983**

Bruland, K.W., and Lohan, M.C., 2006. Controls of trace metals in seawater. In Elderfield, H., Treatise on Geochemistry (Volume 6): the Oceans and Marine Geochemistry. Amsterdam (Elsevier), 23–47. **https://doi.org/10.1016/B0-08-043751-6/06105-3**

Bünz, S., Polyanov, S., Vadakkepuliyambatta, S., Consolaro, C., and Mienert, J., 2012. Active gas venting through hydrate-bearing sediments on the Vestnesa Ridge, offshore W-Svalbard. Marine Geology, 332–334:189–197. **https://doi.org/10.1016/j.margeo.2012.09.012**

Cande, S.C., and Kent, D.V., 1995. Revised calibration of the geomagnetic polarity timescale for the Late Cretaceous and Cenozoic. Journal of Geophysical Research: Solid Earth, 100:6093–6095. **https://doi.org/10.1029/94JB03098**

Caricchi, C., Lucchi, R.G., Sagnotti, L., Macrì, P., Di Roberto, A., Del Carlo, P., Husum, K., Laberg, J.S., and Morigi, C., 2019. A high-resolution geomagnetic relative paleointensity record from the Arctic Ocean deep-water gateway deposits during the last 60 kyr. Geochemistry, Geophysics, Geosystems, 20(5):2355–2377. **https://doi.org/10.1029/2018GC007955**

Channell, J.E.T., Singer, B.S., and Jicha, B.R., 2020. Timing of Quaternary geomagnetic reversals and excursions in volcanic and sedimentary archives. Quaternary Science Reviews, 228:106114. **https://doi.org/10.1016/j.quascirev.2019.106114**

Chauhan, T., Rasmussen, T.L., Noormets, R., Jakobsson, M., and Hogan, K.A., 2014. Glacial history and paleoceanography of the southern Yermak Plateau since 132 ka BP. Quaternary Science Reviews, 92:155–169. **https://doi.org/10.1016/j.quascirev.2013.10.023**

Consolaro, C., Rasmussen, T.L., Panieri, G., Mienert, J., Bünz, S., and Sztybor, K., 2015. Carbon isotope ($\delta^{13}C$) excursions suggest times of major methane release during the last 14 kyr in Fram Strait, the deep-water gateway to the Arctic. Climate of the Past, 11(4):669–685. **https://doi.org/10.5194/cp-11-669-2015**

Curry, W.B., Shackleton, N.J., Richter, C, et al., 1995. Proceedings of the Ocean Drilling Program, Initial Reports, 154: College Station, TX (Ocean Drilling Program). **https://doi.org/10.2973/odp.proc.ir.154.1995**

De Schepper, S., Beck, K.M., and Mangerud, G., 2017. Late Neogene dinoflagellate cyst and acritarch biostratigraphy for Ocean Drilling Program Hole 642B, Norwegian Sea. Review of Palaeobotany and Palynology, 236:12–32. **https://doi.org/10.1016/j.revpalbo.2016.08.005**

De Schepper, S., and Head, M.J., 2009. Pliocene and Pleistocene dinoflagellate cyst and acritarch zonation of DSDP Hole 610A, eastern North Atlantic. Palynology, 33(1):179–218. **https://doi.org/10.2113/gspalynol.33.1.179**

de Vernal, A., Radi, T., Zaragosi, S., Van Nieuwenhove, N., Rochon, A., Allan, E., De Schepper, S., Eynaud, F., Head, M.J., Limoges, A., Londeix, L., Marret, F., Matthiessen, J., Penaud, A., Pospelova, V., Price, A., and Richerol, T., 2020. Distribution of common modern dinoflagellate cyst taxa in surface sediments of the Northern Hemisphere in relation to environmental parameters: The new n=1968 database. Marine Micropaleontology, 159:101796. **https://doi.org/10.1016/j.marmicro.2019.101796**

Deschamps, P., Durand, N., Bard, E., Hamelin, B., Camoin, G., Thomas, A.L., Henderson, G.M., Okuno, J.i., and Yokoyama, Y., 2012. Ice-sheet collapse and sea-level rise at the Bolling warming 14,600 years ago. Nature, 483(7391):559–564. **https://doi.org/10.1038/nature10902**

Ehlers, B.-M., and Jokat, W., 2013. Paleo-bathymetry of the northern North Atlantic and consequences for the opening of the Fram Strait. Marine Geophysical Research, 34(1):25–43. **https://doi.org/10.1007/s11001-013-9165-9**

Eidvin, T., and Rundberg, Y., 2001. Late Cainozoic stratigraphy of the Tampen area (Snorre and Yisund fields) in the northern North Sea, with emphasis on the chronology of early Neogene sands. Norwegian Journal of Geology, 81(2):119–160. **https://njg.geologi.no/images/NJG_articles/NGT_81_2_119-160.pdf**

Eiken, O., and Hinz, K., 1993. Contourites in the Fram Strait. Sedimentary Geology, 82(1–4):15–32. **https://doi.org/10.1016/0037-0738(93)90110-Q**

Engen, Ø., Faleide, J.I., and Dyreng, T.K., 2008. Opening of the Fram Strait gateway: a review of plate tectonic constraints. Tectonophysics, 450(1–4):51–69. **https://doi.org/10.1016/j.tecto.2008.01.002**

Feyling-Hanssen, R.W., Funder, S., and Petersen, K.S., 1983. The Lodin Elv Formation; a Plio-Pleistocene occurrence in Greenland. Bulletin of the Geological Society of Denmark, 31:81–106. **https://2dgf.dk/xpdf/bull31-03-04-81-106.pdf**

Flores, J.A., Filippelli, G.M., Sierro, F.J., and Latimer, J.C., 2012. The "White Ocean" Hypothesis: A Late Pleistocene Southern Ocean Governed by Coccolithophores and Driven by Phosphorus. Frontiers in Microbiology, 3. **https://doi.org/10.3389/fmicb.2012.00233**

González-Lanchas, A., Rickaby, R.E.M., Sierro, F.J., Rigual-Hernández, A.S., Alonso-García, M., and Flores, J.A., 2023. Globally enhanced calcification across the coccolithophore Gephyrocapsa complex during the mid-Brunhes interval. Quaternary Science Reviews, 321:108375. **https://doi.org/10.1016/j.quascirev.2023.108375**

Gradstein, F.M., Ogg, J.G., Schmitz, M.D., and Ogg, G.M. (Eds.), 2020. Geologic Time Scale 2020: Amsterdam (Elsevier BV). **https://doi.org/10.1016/C2020-1-02369-3**

Graves, C.A., James, R.H., Sapart, C.J., Stott, A.W., Wright, I.C., Berndt, C., Westbrook, G.K., and Connelly, D.P., 2017. Methane in shallow subsurface sediments at the landward limit of the gas hydrate stability zone offshore western Svalbard. Geochimica et Cosmochimica Acta, 198:419–438. **https://doi.org/10.1016/j.gca.2016.11.015**

Head, M.J., 1993. Dinoflagellates, sporomorphs, and other palynomorphs from the upper Pliocene St. Erth beds of Cornwall, southwestern England. Memoir (The Paleontological Society), 31. **https://doi.org/10.1017/S0022336000061126**

Head, M.J., 2003. Neogene occurrences of the marine acritarch genus Nannobarbophora Habib and Knapp, 1982 emend., and the new species N. Gedlii. Journal of Paleontology, 77(2):382–385. **https://doi.org/10.1666/0022-3360(2003)077<0382:NOOTMA>2.0.CO;2**

Himmler, T., Sahy, D., Martma, T., Bohrmann, G., Plaza-Faverola, A., Bünz, S., Condon, D.J., Knies, J., and Lepland, A., 2019. A 160,000-year-old history of tectonically controlled methane seepage in the Arctic. Science Advances, 5(8):eaaw1450. **https://doi.org/10.1126/sciadv.aaw1450**

Hopkins, T.S., 1991. The GIN Sea—a synthesis of its physical oceanography and literature review 1972–1985. Earth-Science Reviews, 30(3):175–318. **https://doi.org/10.1016/0012-8252(91)90001-V**

Horng, C.-S., 2018. Unusual Magnetic Properties of Sedimentary Pyrrhotite in Methane Seepage Sediments: Comparison With Metamorphic Pyrrhotite and Sedimentary Greigite. Journal of Geophysical Research: Solid Earth, 123(6):4601–4617. **https://doi.org/10.1002/2017JB015262**

Hustoft, S., Bünz, S., Mienert, J., and Chand, S., 2009. Gas hydrate reservoir and active methane-venting province in sediments on <20 Ma young oceanic crust in the Fram Strait, offshore NW-Svalbard. Earth and Planetary Science Letters, 284(1–2):12–24. **https://doi.org/10.1016/j.epsl.2009.03.038**

Husum, K., and Hald, M., 2012. Arctic planktic foraminiferal assemblages: Implications for subsurface temperature reconstructions. Marine Micropaleontology, 96-97:38–47. **https://doi.org/10.1016/j.marmicro.2012.07.001**

Jakobsson, M., Backman, J., Rudels, B., Nycander, J., Frank, M., Mayer, L., Jokat, W., Sangiorgi, F., O'Regan, M., Brinkhuis, H., King, J., and Moran, K., 2007. The Early Miocene onset of ventilated circulation regime in the Arctic Ocean. Nature, 447(7147):986–990. **https://doi.org/10.1038/nature05924**

Jakobsson, M., Ingólfsson, Ó., Long, A.J., and Spielhagen, R.F., 2014. The dynamic Arctic. Quaternary Science Reviews, 92:1–8. **https://doi.org/10.1016/j.quascirev.2014.03.022**

Jessen, S.P., Rasmussen, T.L., Nielsen, T., and Solheim, A., 2010. A new late Weichselian and Holocene marine chronology for the western Svalbard slope 30,000–0 cal years BP. Quaternary Science Reviews, 29(9–10):1301–1312. **https://doi.org/10.1016/j.quascirev.2010.02.020**

Kastner, M., Claypool, G., and Robertson, G., 2008. Geochemical constraints on the origin of the pore fluids and gas hydrate distribution at Atwater Valley and Keathley Canyon, northern Gulf of Mexico. Marine and Petroleum Geology, 25(9):860–872. **https://doi.org/10.1016/j.marpetgeo.2008.01.022**

King, C., 1983. Cainozoic micropalaeontological biostratigraphy of the North Sea. Report of the Institute of Geological Sciences, 82/7:1–40. **https://pubs.bgs.ac.uk/publications.html?pubID=B01222**

Kirschvink, J.L., 1980. The least-squares line and plane and the analysis of palaeomagnetic data. Geophysical Journal International, 62(3):699–718. **https://doi.org/10.1111/j.1365-246X.1980.tb02601.x**

Kjær, K.H., Winther Pedersen, M., De Sanctis, B., De Cahsan, B., Korneliussen, T.S., Michelsen, C.S., Sand, K.K., Jelavić, S., Ruter, A.H., Schmidt, A.M.A., Kjeldsen, K.K., Tesakov, A.S., Snowball, I., Gosse, J.C., Alsos, I.G., Wang, Y., Dockter, C., Rasmussen, M., Jørgensen, M.E., Skadhauge, B., Prohaska, A., Kristensen, J.Å., Bjerager, M., Allentoft, M.E., Coissac, E., Alsos, I.G., Coissac, E., Rouillard, A., Simakova, A., Fernandez-Guerra, A., Bowler, C., Macias-Fauria, M., Vinner, L., Welch, J.J., Hidy, A.J., Sikora, M., Collins, M.J., Durbin, R., Larsen, N.K., Willerslev, E., and PhyloNorway, C., 2022. A 2-million-year-old ecosystem in Greenland uncovered by environmental DNA. Nature, 612(7939):283–291. **https://doi.org/10.1038/s41586-022-05453-y**

Knies, J., Mattingsdal, R., Fabian, K., Grøsfjeld, K., Baranwal, S., Husum, K., De Schepper, S., Vogt, C., Andersen, N., Matthiessen, J., Andreassen, K., Jokat, W., Nam, S.-I., and Gaina, C., 2014. Effect of early Pliocene uplift on Late Pliocene cooling in the Arctic–Atlantic gateway. Earth and Planetary Science Letters, 387:132–144. **https://doi.org/10.1016/j.epsl.2013.11.007**

Koç, N., and Scherer, R.P., 1996. Neogene diatom biostratigraphy of the Iceland Sea Site 907. In Thiede, J., Myhre, A.M., Firth, J.V., Johnson, G.L., and Ruddiman, W.F. (Eds.), Proceedings of the Ocean Drilling Program, Scientific Results, 151: College Station, TX (Ocean Drilling Program), 61–74. **https://doi.org/10.2973/odp.proc.sr.151.108.1996**

Kolawole, F., and Evenick, J.C., 2023. Global distribution of geothermal gradients in sedimentary basins. Geoscience Frontiers, 14(6):101685. **https://doi.org/10.1016/j.gsf.2023.101685**

Lam, A.R., Crundwell, M.P., Leckie, R.M., Albanese, J., and Uzel, J.P., 2022. Diachroneity rules the mid-latitudes: a test case using Late Neogene planktic foraminifera across the Western Pacific. Geosciences, 12(5):190. **https://doi.org/10.3390/geosciences12050190**

Lourens, L., Hilgen, F., Shackleton, N.J., Laskar, J., and Wilson, D., 2004. The Neogene period. In Smith, A.G., Gradstein, F.M. and Ogg, J.G., A Geologic Time Scale 2004. Cambridge, UK (Cambridge University Press), 409–440. **https://doi.org/10.1017/CBO9780511536045.022**

Lucchi, R.G., Camerlenghi, A., Rebesco, M., Colmenero-Hidalgo, E., Sierro, F.J., Sagnotti, L., Urgeles, R., Melis, R., Morigi, C., Bárcena, M.A., Giorgetti, G., Villa, G., Persico, D., Flores, J.A., Rigual-Hernández, A.S., Pedrosa, M.T., Macri, P., and Caburlotto, A., 2013. Postglacial sedimentary processes on the Storfjorden and Kveithola trough

mouth fans: significance of extreme glacimarine sedimentation. Global and Planetary Change, 111:309–326. **https://doi.org/10.1016/j.gloplacha.2013.10.008**

Lucchi, R.G., Sagnotti, L., Camerlenghi, A., Macrì, P., Rebesco, M., Pedrosa, M.T., and Giorgetti, G., 2015. Marine sedimentary record of Meltwater Pulse 1a along the NW Barents Sea continental margin. arktos, 1(1):7. **https://doi.org/10.1007/s41063-015-0008-6**

Lucchi, R.G., St. John, K., and Ronge, T.A., 2023. Expedition 403 Scientific Prospectus: Eastern Fram Strait Paleo-Archive (FRAME). International Ocean Discovery Program. **https://doi.org/10.14379/iodp.sp.403.2023**

Lucchi, R.G., St. John, K.E.K., Ronge, T.A., Barcena, M.A., De Schepper, S., Duxbury, L.C., Gebhardt, A.C., Gonzalez-Lanchas, A., Goss, G., Greco, N.M., Gruetzner, J., Haygood, L., Husum, K., Iizuka, M., Kapuge, A.K.I.U., Lam, A.R., Libman-Roshal, O., Liu, Y., Monito, L.R., Reilly, B.T., Rosenthal, Y., Sakai, Y., Sijinkumar, A.V., Suganuma, Y., and Zhong, Y., 2026. Expedition 403 methods. In Lucchi, R.G., St. John, K.E.K., Ronge, T.A., and the Expedition 403 Scientists, Eastern Fram Strait Paleo-Archive. Proceedings of the International Ocean Discovery Program, 403: College Station, TX (International Ocean Discovery Program). **https://doi.org/10.14379/iodp.proc.403.102.2026**

Maiorano, P., Marino, M., Balestra, B., Flores, J.A., Hodell, D.A., and Rodrigues, T., 2015. Coccolithophore variability from the Shackleton Site (IODP Site U1385) through MIS 16-10. Global and Planetary Change, 133:35–48. **https://doi.org/10.1016/j.gloplacha.2015.07.009**

Martini, E., 1971. Standard Tertiary and Quaternary calcareous nannoplankton zonation. Proceedings of the Second Planktonic Conference, Roma, 1970:739–785.

Matthiessen, J., and Brenner, W., 1996. Dinoflagellate cyst ecostratigraphy of Pliocene-Pleistocene sediments from the Yermak Plateau (Arctic Ocean, Hole 911A). In Thiede, J., Myhre, A.M., Firth, J.V., Johnson, G.L., and Ruddiman, W.F. (Eds.), Proceedings of the Ocean Drilling Program, Scientific Results, 151: 243–253. **https://doi.org/10.2973/odp.proc.sr.151.109.1996**

Matthiessen, J., and Knies, J., 2001. Dinoflagellate cyst evidence for warm interglacial conditions at the northern Barents Sea margin during marine oxygen isotope stage 5. Journal of Quaternary Science, 16(7):727–737. **https://doi.org/10.1002/jqs.656**

Matthiessen, J., Schreck, M., De Schepper, S., Zorzi, C., and de Vernal, A., 2018. Quaternary dinoflagellate cysts in the Arctic Ocean: potential and limitations for stratigraphy and paleoenvironmental reconstructions. Quaternary Science Reviews, 192:1–26. **https://doi.org/10.1016/j.quascirev.2017.12.020**

Mattingsdal, R., Knies, J., Andreassen, K., Fabian, K., Husum, K., Grøsfjeld, K., and De Schepper, S., 2014. A new 6 Myr stratigraphic framework for the Atlantic–Arctic gateway. Quaternary Science Reviews, 92:170–178. **https://doi.org/10.1016/j.quascirev.2013.08.022**

Matul, A., and Kazarina, G.K., 2020. The North Pacific Diatom Species Neodenticula seminae in the Modern and Holocene Sediments of the North Atlantic and Arctic. Geosciences, 10(5). **https://doi.org/10.3390/geosciences10050173**

Meyers, P.A., 1994. Preservation of elemental and isotopic source identification of sedimentary organic matter. Chemical Geology, 114(3–4):289–302. **https://doi.org/10.1016/0009-2541(94)90059-0**

Meyers, P.A., 1997. Organic geochemical proxies of paleoceanographic, paleolimnologic, and paleoclimatic processes. Organic Geochemistry, 27(5–6):213–250. **https://doi.org/10.1016/S0146-6380(97)00049-1**

Miettinen, A., Koç, N., and Husum, K., 2013. Appearance of the Pacific diatom Neodenticula seminae in the northern Nordic Seas — An indication of changes in Arctic sea ice and ocean circulation. Marine Micropaleontology, 99:2–7. **https://doi.org/10.1016/j.marmicro.2012.06.002**

Pados, T., and Spielhagen, R.F., 2014. Species distribution and depth habitat of recent planktic foraminifera in Fram Strait, Arctic Ocean. Polar Research, 33. **https://doi.org/10.3402/polar.v33.22483**

Pape, T., Bünz, S., Hong, W.-L., Torres, M.E., Riedel, M., Panieri, G., Lepland, A., Hsu, C.-W., Wintersteller, P., Wallmann, K., Schmidt, C., Yao, H., and Bohrmann, G., 2020. Origin and transformation of light hydrocarbons ascending at an active pockmark on Vestnesa Ridge, Arctic Ocean. Journal of Geophysical Research: Solid Earth, 125(1):e2018JB016679. **https://doi.org/10.1029/2018JB016679**

Peters, C., and Thompson, R., 1998. Magnetic identification of selected natural iron oxides and sulphides. Journal of Magnetism and Magnetic Materials, 183(3):365–374. **https://doi.org/10.1016/S0304-8853(97)01097-4**

Plaza-Faverola, A., Bünz, S., Johnson, J.E., Chand, S., Knies, J., Mienert, J., and Franek, P., 2015. Role of tectonic stress in seepage evolution along the gas hydrate-charged Vestnesa Ridge, Fram Strait. Geophysical Research Letters, 42(3):733–742. **https://doi.org/10.1002/2014GL062474**

Plaza-Faverola, A., Sultan, N., Lucchi, R.G., El bani Altuna, N., Ramachandran, H., Singhroha, S., Cooke, F., Vadakkepuliyambatta, S., Ezat, M.M., and Rasmussen, T.L., 2023. Spatial changes in gas transport and sediment stiffness influenced by regional stress: observations from piezometer data along Vestnesa Ridge, eastern Fram Strait. Journal of Geophysical Research: Solid Earth, 128(5):e2022JB025868. **https://doi.org/10.1029/2022JB025868**

Raffi, I., 2002. Revision of the Early-Middle Pleistocene calcareous nannofossil biochronology (1.75–0.85 Ma). Marine Micropaleontology, 45(1):25–55. **https://doi.org/10.1016/S0377-8398(01)00044-5**

Raffi, I., Backman, J., Fornaciari, E., Pälike, H., Rio, D., Lourens, L., and Hilgen, F., 2006. A review of calcareous nannofossil astrobiochronology encompassing the past 25 million years. Quaternary Science Reviews, 25(23):3113–3137. **https://doi.org/10.1016/j.quascirev.2006.07.007**

Rasmussen, T.L., and Nielsen, T., 2024. Glacial-interglacial sedimentation control on gas seepage exemplified by Vestnesa Ridge off NW Svalbard margin. Frontiers in Earth Science, 12:1356341. **https://doi.org/10.3389/feart.2024.1356341**

Razmjooei, M.J., Henderiks, J., Coxall, H.K., Baumann, K.-H., Vermassen, F., Jakobsson, M., Niessen, F., and O'Regan, M., 2023. Revision of the Quaternary calcareous nannofossil biochronology of Arctic Ocean sediments. Quaternary Science Reviews, 321:108382. **https://doi.org/10.1016/j.quascirev.2023.108382**

Reid, P.C., Johns, D.G., Edwards, M., Starr, M., Poulin, M., and Snoeijs, P., 2007. A biological consequence of reducing Arctic ice cover: arrival of the Pacific diatom Neodenticula seminae in the North Atlantic for the first time in 800,000 years. Global Change Biology, 13(9):1910–1921. **https://doi.org/10.1111/j.1365-2486.2007.01413.x**

Richter, C., Acton, G., Endris, C., and Radsted, M., 2007. Technical Note 34: Handbook for shipboard paleomagnetists. Ocean Drilling Program. **https://doi.org/10.2973/odp.tn.34.2007**

Rio, D., Fornaciari, E., and Raffi, I., 1990. Late Oligocene through early Pleistocene calcareous nannofossils from western equatorial Indian Ocean (Leg 115). In Duncan, R.A., Backman, J., Peterson, L. C, et al., Proceedings of the Ocean Drilling Program, Scientific Results, 115: College Station, TX (Ocean Drilling Program), 175–235. **https://doi.org/10.2973/odp.proc.sr.115.152.1990**

Roberts, A.P., Chang, L., Rowan, C.J., Horng, C.-S., and Florindo, F., 2011. Magnetic properties of sedimentary greigite (Fe_3S_4): an update. Reviews of Geophysics, 49(1):RG1002. **https://doi.org/10.1029/2010RG000336**

Roberts, A.P., and Weaver, R., 2005. Multiple mechanisms of remagnetization involving sedimentary greigite (Fe_3S_4). Earth and Planetary Science Letters, 231(3):263–277. **https://doi.org/10.1016/j.epsl.2004.11.024**

Rodriguez, N.M., Paull, C.K., and Borowski, W.S., 2000. Zonation of authigenic carbonates within gas hydrate-bearing sedimentary sections on the Blake Ridge: offshore southeastern North America. In Paull, C.K., Matsumoto, R., Wallace, P.J., and Dillon, W.P. (Eds.), Proceedings of the Ocean Drilling Program, Scientific Results, 164: College Station, TX (Ocean Drilling Program), 301–312. **https://doi.org/10.2973/odp.proc.sr.164.227.2000**

Sato, T., and Kameo, K., 1996. Pliocene to Quaternary calcareous nannofossil biostratigraphy of the Arctic Ocean, with reference to late Pliocene glaciation. In Thiede, J., Myhre, A.M., Firth, J.V., Johnson, G.L., and Ruddiman, W.F. (Eds.), Proceedings of the Ocean Drilling Program, Scientific Results, 151: College Station, TX (Ocean Drilling Program), 39–59. **https://doi.org/10.2973/odp.proc.sr.151.112.1996**

Sato, T., Kameo, K., and Mita, I., 1999. Validity of the latest Cenozoic calcareous nannofossil datums and its application to the tephrochronology. Earth Science (Chikyu Kagaku), 53(4):265–274. **https://doi.org/10.15080/agcjchikyukagaku.53.4_265**

Sato, T., Kameo, K., and Takayama, T., 1991. Coccolith biostratigraphy of the Arabian Sea. In Prell, W.L., Niitsuma, N., et al., Proceedings of the Ocean Drilling Program, Scientific Results, 117: College Station, TX (Ocean Drilling Program), 37–54. **https://doi.org/10.2973/odp.proc.sr.117.133.1991**

Schiebel, R., and Hemleben, C., 2017. Planktic Foraminifers in the Modern Ocean: Berlin (Springer). **https://doi.org/10.1007/978-3-662-50297-6**

Schneider, A., Panieri, G., Lepland, A., Consolaro, C., Crémière, A., Forwick, M., Johnson, J.E., Plaza-Faverola, A., Sauer, S., and Knies, J., 2018. Methane seepage at Vestnesa Ridge (NW Svalbard) since the Last Glacial Maximum. Quaternary Science Reviews, 193:98–117. **https://doi.org/10.1016/j.quascirev.2018.06.006**

Sejrup, H.P., Birks, H.J.B., Klitgaard Kristensen, D., and Madsen, H., 2004. Benthonic foraminiferal distributions and quantitative transfer functions for the northwest European continental margin. Marine Micropaleontology, 53(1):197–226. **https://doi.org/10.1016/j.marmicro.2004.05.009**

Shipboard Scientific Party, 1995. Site 912. In Myhre, A.M., Thiede, J., Firth, J.V., et al., Proceedings of the Ocean Drilling Program, Initial Reports, 151: College Station, TX (Ocean Drilling Program), 319–343. **https://doi.org/10.2973/odp.proc.ir.151.110.1995**

Sloan, E.D., 1998. Gas Hydrates: Review of Physical/Chemical Properties. Energy & Fuels, 12(2):191-196. **https://doi.org/10.1021/ef970164+**

Smelror, M., 1999. Pliocene-Pleistocene and redeposited dinoflagellate cysts from the western Svalbard margin (Site 986); biostratigraphy, paleoenvironments, and sediment provenance. In Raymo, M.E., Jansen, E., Blum, P., and Herbert, T.D. (Eds.), Proceedings of the Ocean Drilling Program, Scientific Results, 162: College Station, TX (Ocean Drilling Program), 83–97. **https://doi.org/10.2973/odp.proc.sr.162.011.1999**

Smith, A.J., Mienert, J., Bünz, S., and Greinert, J., 2014. Thermogenic methane injection via bubble transport into the upper Arctic Ocean from the hydrate-charged Vestnesa Ridge, Svalbard. Geochemistry, Geophysics, Geosystems, 15(5):1945–1959. **https://doi.org/10.1002/2013GC005179**

Spiegler, D., 1996. Planktonic foraminifer Cenozoic biostratigraphy of the Arctic Ocean, Fram Strait (Sites 908–909), Yermak Plateau (Sites 910-912), and East Greenland Margin (Site 913). In Thiede, J., Myhre, A.M., Firth, J.V., Johnson, G.L., and Ruddiman, W.F. (Eds.), Proceedings of the Ocean Drilling Program, Scientific Results, 151: College Station, TX (Ocean Drilling Program), 153–167. **https://doi.org/10.2973/odp.proc.sr.151.104.1996**

Stein, R., and Stax, R., 1996. Organic carbon and *n*-alkane distribution in late Cenozoic sediments of Arctic gateways Sites 909 and 911 and their paleoenvironmental implications: preliminary results. In Thiede, J., Myhre, A.M., Firth, J.V., Johnson, G.L., and Ruddiman, W.F. (Eds.), Proceedings of the Ocean Drilling Program, Scientific Results, 151: College Station, TX (Ocean Drilling Program), 391–405. **https://doi.org/10.2973/odp.proc.sr.151.143.1996**

Stober, J.C., and Thompson, R., 1979. An investigation into the source of magnetic minerals in some Finnish lake sediments. Earth and Planetary Science Letters, 45(2):464–474. **https://doi.org/10.1016/0012-821X(79)90145-6**

Sultan, N., Plaza-Faverola, A., Vadakkepuliyambatta, S., Buenz, S., and Knies, J., 2020. Impact of tides and sea-level on deep-sea Arctic methane emissions. Nature Communications, 11(1):5087. **https://doi.org/10.1038/s41467-020-18899-3**

Sztybor, K., and Rasmussen, T., 2017. Late glacial and deglacial palaeoceanographic changes at Vestnesa Ridge, Fram Strait: methane seep versus non-seep environments. Palaeogeography, Palaeoclimatology, Palaeoecology, 476:77–89. **https://doi.org/10.1016/j.palaeo.2017.04.001**

Thierstein, H.R., Geitzenauer, K.R., Molfino, B., and Shackleton, N.J., 1977. Global synchroneity of late Quaternary coccolith datum levels validation by oxygen isotopes. Geology, 5(7):400–404. **https://doi.org/10.1130/0091-7613(1977)5<400:GSOLQC>2.0.CO;2**

Ussler, W., III, and Paull, C.K., 2001. Ion Exclusion Associated with Marine Gas Hydrate Deposits. In Natural Gas Hydrates: Occurrence, Distribution, and Detection. 41–51. **https://doi.org/10.1029/GM124p0041**

Voorthuysen, J.H., 1950. The quantitative distribution of the Pleistocene, Pliocene and Miocene Foraminifera of boring Zaandam (Netherlands). Mededelingen Geologische Stichting, Nieuwe, 4:51–72.
Zhang, L., Chan, L.-H., and Gieskes, J.M., 1998. Lithium isotope geochemistry of pore waters from Ocean Drilling Program Sites 918 and 919, Irminger Basin. Geochimica et Cosmochimica Acta, 62(14):2437–2450. **https://doi.org/10.1016/S0016-7037(98)00178-1**